

FABRICATION OF ALUMINA-CARBON COMPOSITES FOR
HYDROGEN SEPARATION



A THESIS SUBMITTED IN PARTIAL FULFILLMENT OF THE REQUIREMENT FOR THE
DEGREE OF DOCTOR OF PHILOSOPHY IN APPLIED PHYSICS
DEPARTMENT OF PHYSICS SCHOOL OF SCIENCE
KING MONGKUT'S INSTITUTE OF TECHNOLOGY LADKRABANG

2024

KMITL-2024-SC-D-030-037

This material is reserved for educational use only, not allowed for commercial use.

Forbidden to modify the content, and cite the document when use.



COPYRIGHT 2024

SCHOOL OF SCIENCE

KING MONGKUT'S INSTITUTE OF TECHNOLOGY LADKRABANG

This material is reserved for educational use only, not allowed for commercial use.

Forbidden to modify the content, and cite the document when use.

Thesis Title	Fabrication of Alumina-Carbon Composites for Hydrogen Separation
Student Name	Montree Hankoy
Student ID	62605011
Degree	Doctor of Philosophy (Applied Physics)
Department	Physics
Year	2024
Thesis Advisor	Asst. Prof. Dr. Mettaya Kitiwan
Thesis Co-advisor	Dr. Duangduen Atong

Abstract

This research presents an efficient method to fabricate macroporous Al_2O_3 -carbon flat sheet composite membranes for hydrogen separation using different types and concentrations of carbon materials. Specifically, a series of Al_2O_3 -carbon composite membranes were produced from four categories of carbon: activated carbon (AAC), carbon black (ACB), graphene oxide (AGO), and graphite (AGP). For each composite, carbon was added in amounts of 0.5, 1.0, 1.5, 2.0, 2.5, and 3.0 wt%. Additionally, a carbon-free Al_2O_3 membrane was prepared as a reference specimen. All composite membranes were sintered at 1500 °C for 2 h with a heating rate and cooldown rate of 5 °C/min under an argon (Ar) atmosphere. The membranes were then characterized in terms of phase structure identification, morphology, bulk density, porosity, pore size distribution, mechanical properties, and hydrogen separation performance. The characterization of the membranes depended on the categories and amounts of carbon loading. The performance (permeability and selectivity of hydrogen) of the composite membranes was studied under various temperatures ranging from 30 to 500 °C. The results showed that carbon black composite membranes exhibited the highest hydrogen permeance, reaching The highest hydrogen permeance values were observed for AAC (3.0 wt% carbon addition) at $275 \times 10^{-6} \text{ mol m}^{-2} \text{ s}^{-1} \text{ Pa}^{-1}$, followed by ACB (3.0 wt% carbon addition) at $508 \times 10^{-6} \text{ mol m}^{-2} \text{ s}^{-1} \text{ Pa}^{-1}$, AGO (2.5 wt% carbon addition) at $408 \times 10^{-6} \text{ mol m}^{-2} \text{ s}^{-1} \text{ Pa}^{-1}$, and AGP (3.0 wt% carbon addition) at $403 \times 10^{-6} \text{ mol m}^{-2} \text{ s}^{-1} \text{ Pa}^{-1}$. Additionally, H_2/N_2 selectivity was also enhanced, with the highest values for each carbon type being 4.01 (AAC, 3.0 wt%

This material is reserved for educational use only, not allowed for commercial use.

Forbidden to modify the content, and cite the document when use.

carbon), 3.82 (ACB, 3.0 wt% carbon), 4.20 (AGO, 2.5 wt% carbon), and 4.03 (AGP, 3.0 wt% carbon). The Knudsen diffusion mechanism was observed for all categories and concentrations of carbon materials. Overall, this research suggests that the selection of carbon material and its concentration significantly impacts the performance of Al_2O_3 -carbon composite membranes for hydrogen separation. The preliminary study of H_2S absorption was conducted for AGO composite membranes. The adsorption capacity of AGO adsorbent was found to be between 0.07-0.43 mg/g, which is higher than that of pure alumina (0.06 mg/g). These preliminary results suggest that AGO composites have the potential to be used for H_2S removal at ambient temperature.

Keywords : Hydrogen permeance, H_2/N_2 selectivity, Knudsen diffusion, composite membrane.



Acknowledgements

First, I would like to extend my sincere gratitude to my supervisors, Asst. Prof. Dr. Mettaya Kitiwan and Dr. Duangduen Atong, for their invaluable guidance and support throughout this research project. Not only did they share their profound knowledge and expertise in the field of hydrogen separation membranes, but they also provided unwavering encouragement and insightful feedback that significantly enriched my research journey. Their willingness to connect me with key researchers in the field opened doors to invaluable collaborations, further enriching my understanding of the topic.

I would also like to offer my special thanks to Dr. Supawan Vichaphund, Dr. Kanit Soongprasit, Dr. Chakrit Soongprasit, Dr. Punchaluck Sirinwaranon, Mr. Mana Rodchom, and Ms. Panida Wimuktiwan, the researchers at the Thailand National Metal and Materials Center (MTEC), for their help and guidance in understanding the hydrogen separation system. Beyond the academic realm, they fostered a supportive and encouraging environment, allowing me to develop my confidence as a researcher and navigate the challenges of independent research. I am truly grateful for their mentorship and consider myself fortunate to have had the opportunity to learn from them.

I sincerely thank the Thailand Graduate Institute of Science and Technology (TGIST) under the National Science and Technology Development Agency (NSTDA) for awarding me the Ph.D. scholarship (Grant No. SCA-CO-2563-12077-TH). Their financial support was crucial in enabling this research.

Finally, I would like to express my heartfelt thanks to my family. Their unwavering love and belief in me have been the bedrock of my success. I appreciate the countless sacrifices they made, from juggling work and household duties to providing financial support. I would not be here without their endless encouragement and belief in my dreams.

Mr. Montree Hankoy

This material is reserved for educational use only, not allowed for commercial use.

Forbidden to modify the content, and cite the document when use.

Table of contents

Contents	Page
Abstract.....	i
Acknowledgements.....	iii
Table of contents.....	iv
List of tables.....	vii
List of figures.....	viii
Chapter 1 Introduction.....	1
1.1 Research Motivation.....	1
1.2 Objectives of the study.....	3
1.3 Scopes of the study.....	3
1.4 Benefits of the study.....	3
Chapter 2 Theory and literature reviews.....	5
2.1 Hydrogen production method.....	5
2.1.1 Natural gas to hydrogen.....	5
2.1.2 Coal to hydrogen.....	5
2.1.3 Biomass to hydrogen.....	6
2.2 Hydrogen purification method.....	7
2.2.1 Pressure swing absorption.....	8
2.2.2 Cryogenic distillation.....	9
2.2.3 Hydrogen separation membrane.....	9
2.2.3.1 Porous separation membrane.....	9
2.2.3.2 Polymeric separation membrane.....	11
2.2.3.3 Dense ceramic ion transport membrane.....	12
2.2.3.4 Dense metallic membranes.....	14

This material is reserved for educational use only, not allowed for commercial use.

Forbidden to modify the content, and cite the document when use.

2.2.3.5	Carbon-based membranes	16
2.2.3.5.1	Activated carbon	17
2.2.3.5.2	Carbon black	17
2.2.3.5.3	Graphene oxide	18
2.2.3.5.4	Graphite	19
2.3	Mechanisms for gas separation	20
2.3.1	Knudsen Diffusion	21
2.3.2	Poiseuille (Viscous Flow)	22
2.3.3	Capillary Condensation	23
2.3.4	Selective Adsorption / Surface Diffusion	23
2.3.5	Molecular Sieving	24
2.3.6	Configurational / Micropore Diffusion	24
2.3.7	Single File Diffusion	25
2.4	Literature review	25
2.4.1	Disk membrane	25
2.4.2	Tubular membrane	27
2.4.3	Hollow fiber membrane	28
2.4.4	Composite membrane	31
Chapter 3	Research methodology	34
3.1	Raw materials	34
3.2	Fabrication procedure	35
3.2.1	Membrane sintering	36
3.3	Composites characterization	37
3.3.1	Phase Identification	37
3.3.2	Microstructure characterization	38

This material is reserved for educational use only, not allowed for commercial use.

Forbidden to modify the content, and cite the document when use.

3.3.3 Pore size distribution.....	38
3.3.4 Density measurement.....	38
3.3.5 Hardness	40
3.3.6 Gas permeation tests.....	40
3.3.7 Hydrogen sulfide adsorption capacity test.....	41
Chapter 4 Result and discussion	43
4.1 Phase identification	43
4.2 Physical properties.....	49
4.3 Morphology	52
4.4 Pore size distribution.....	58
4.5 Mechanical Properties.....	61
4.6 Gas permeance performance	63
4.7 Hydrogen sulfide removal.....	75
Chapter 5 Conclusion and suggestions.....	79
References.....	82
Appendix	94
Author biography	121

List of tables

Table	Page
Table 2.1 Comparison of Hydrogen Purification Techniques	8
Table 2.2 Characteristics of certain porous membranes used for hydrogen separation	10
Table 2.3 Performance characteristics such as hydrogen permeance, ideal H ₂ /CO ₂ selectivity, and ideal H ₂ /N ₂ selectivity of graphene oxide (GO) membranes	11
Table 2.4 Hydrogen permeabilities and selectivity of the polymer membranes	12
Table 2.5 Conductivities of promising proton-conducting materials for hydrogen separation membranes	14
Table 2.6 Hydrogen permeability and ΔH formation (of hydrides) data for selected Metals.....	16
Table 4.1 Comparing the experimental performance qualitatively regarding hydrogen permeance and H ₂ /N ₂ ideal selectivity.....	74
Table 4.2 The breakthrough time and H ₂ S breakthrough capacity compared to literature.....	78

List of figures

Figure	Page
Figure 2.1 Schematic of hydrogen transport in ion transport membranes	13
Figure 2.2 Hydrogen selectivity versus permeability of different separation membranes	15
Figure 2.3 Schematic presentation of transport mechanisms through membranes (a) Poiseuille flow, (b) Knudsen diffusion, (c) Surface diffusion, (d) multi-layer diffusion, (e) Capillary condensation, (f) Molecular sieving, and (g) Single-file.....	21
Figure 2.4 Fabrication process for graphene oxide membrane	26
Figure 2.5 (A) and (B) the separation results for a 1.8-nm-thick GO membrane, (C) and (D) the separation results for 9-nm membrane, and (E) and (F) for an 18-nm membrane	26
Figure 2.6 Pictures of GO membrane samples; (a) sample 1 and (b) sample 2.....	27
Figure 2.7 Hydrogen permeance and H ₂ /CO ₂ selectivity for GO membrane samples at transmembrane pressure of 1.0 bar; (a) sample 1 and (b) sample 2	28
Figure 2.8 H ₂ permeance for GO membrane samples and (a) H ₂ /CO ₂ ideal selectivity and (b) H ₂ /N ₂ ideal selectivity vs transmembrane pressure at room temperature.....	28
Figure 2.9 The spinel hollow fibers membrane, GO and MgAl ₂ O ₄ /GO composites membrane.....	29
Figure 2.10 SEM images of (a) cross-section of the spinel hollow fiber and (b) surface of GO image, and (c) AFM image of GO surface layer.....	29
Figure 2.11 (a) Individual gas permeance data and (b) the ideal selectivity values for gas permeations through the MgAl ₂ O ₄ /GO composite membrane	29
Figure 2.12 (a) SEM image of alumina hollow fiber membrane, (b) cross section, (c)magnification diagram for b, (d) SEM image of GO sheet used for membrane preparation, (e) SEM images of GO membrane without SDBS: GO@Al ₂ O ₃ , (f) SEM image of GO-SDBS@Al ₂ O ₃ , (g) macroscopical photos of alumina hollow fiber, (h) macroscopical photos composite membrane	30

Figure 2.13 (a) Temperature dependent H ₂ and N ₂ permeances and the respective separation factor of GO-SDBS@Al ₂ O ₃ for H ₂ /N ₂ mixture, (b) time dependent of H ₂ and N ₂ permeances and H ₂ /N ₂ separation factor of GO-SDBS@Al ₂ O ₃ membranes, (c) Temperature dependent H ₂ and CO ₂ permeances and the respective separation factor of GO-SDBS@Al ₂ O ₃ for H ₂ /CO ₂ mixture, (d) Time dependent H ₂ and CO ₂ permeances and H ₂ /CO ₂ separation factor of GO-SDBS@Al ₂ O ₃ membrane	31
Figure 2.14 Arrhenius plot of the hydrogen permeability as function of inversed temperature.....	32
Figure 2.15 Hydrogen permeability of ACG/Al membrane.....	32
Figure 2.16 Hydrogen permeability of ACG/Al membrane and ACZ-10wt.%Co and ACZ-10wt.% Ni	33
Figure 4.1 XRD patterns of starting materials.....	45
Figure 4.2 XRD patterns of (a) AAC, (b) ACB, (c) AGO and (d) AGP composite membranes with the different carbon addition.....	46
Figure 4.3 The Raman spectra of AGO composite membranes.....	48
Figure 4.4 TEM image of AGO3.0 composite membranes.....	49
Figure 4.5 The bulk density, porosity, and the relative density as a functions of carbon content for AAC, ACB, AGO and AGP composite membranes.	51
Figure 4.6 FESEM image of Al ₂ O ₃ membrane.....	52
Figure 4.7 Surface morphology of AAC composite membranes with different activated carbon content.	53
Figure 4.8 Surface morphology of ACB composite membranes with different carbon black content.	54
Figure 4.9 Surface morphology of AGO composite membranes with different graphene oxide content.	55
Figure 4.10 Surface morphology of AGP composite membranes with different graphite content.	56
Figure 4.11 Average grain size of AAC, ACB, AGO and AGP composite membranes with different carbon content.....	57
Figure 4.12 Pore size distributions of (a) AAC, (b) ACB, (c) AGO and (d) AGP composite membranes as a function of carbon content.....	61

Figure 4.13 Vicker's Indentation of AGP composite membrane.....	62
Figure 4.14 Vickers hardness of (a) AAC, (b) ACB, (c) AGO, and (d) AGP composite membrane with different carbon content contents.....	63
Figure 4.15 H ₂ and N ₂ gas permeation as a function of the temperature of mesoporous Al ₂ O ₃ membranes.....	64
Figure 4.16 H ₂ and N ₂ gas permeation as a function of the temperature of AAC composite membranes with different activated carbon contents.....	66
Figure 4.17 H ₂ and N ₂ gas permeation as a function of the temperature of ACB composite membranes with different carbon black contents.....	68
Figure 4.18 H ₂ and N ₂ gas permeation as a function of the temperature of AGO composite membranes with different graphene oxide contents.....	70
Figure 4.19 H ₂ and N ₂ gas permeation as a function of the temperature of AGP composite membranes with different graphite contents.....	72
Figure 4.20 Schematic of gas separation of Al ₂ O ₃ -carbon composite membranes.....	75
Figure 4.21 The H ₂ S concentration in the outlet gas stream as a function of time of AGO composite membranes.....	76
Figure 4.22 H ₂ S breakthrough capacity as a function of GO content.....	77
Figure 4.23 Schematic representation of one feasible mechanism of AGO composite for H ₂ S removal.....	78

Chapter 1

Introduction

1.1 Research Motivation

Several political and scientific have discussed the development for clean and sustainable energy resources. Policies and plans of action are put into place to achieve energy sustainability. The concern about climate change in Thailand has been widely discussed due to 70 percent of the energy sector (power generation, industries, transport, and households) contributing to total greenhouse gas emissions. Thailand Alternative Energy Development Plan (AEDP2015) aims to increase renewable energy usage to 30% by 2036 in three strategies: (i) Renewable electricity generation, (ii) Renewable energy for heat generation, and (iii) Biofuels in the transport sector. In addition, Thailand Climate Change Master Plan (2015–2050) provided the vision 2050 to help Thailand achieve sustainable development, low carbon growth, and climate change resilience by 2050 for reducing greenhouse gas emissions [1]. Corresponding to the vision of the World Energy Outlook 2021 to increase clean energy-based and reduced the greenhouse emission for net-zero emissions in 2050. The power or electricity sector is expected to have a vital role to reduce emissions but a low-carbon fuel such as hydrogen is also essential to achieving the net-zero objective by introducing clean energy technologies [2].

Hydrogen is the first element on the periodic table, usually in the form of a gas. Hydrogen is not only the most abundant element in the universe but also operates as an ecologically benign fuel since the production of energy using hydrogen by fuel cell only produces heat and water leading to reduces emissions of greenhouse gases [3,4]. In addition, hydrogen is of importance as a future fuel source in the transportation and energy sectors. Many research demonstrate the technological viability of utilizing hydrogen [5,6]. Currently available commercial hydrogen production technologies will consider that the development of the technologies can produce hydrogen efficiently, the cost of hydrogen production must be lowered and the requirement for raw resources and infrastructure development to produce hydrogen. One of the interesting technologies that are utilized in the production of hydrogen is membrane technology.

Membrane separation has become an advanced technology designed to solve problems such as energy shortages and environmental problems. Compared with conventional hydrogen production, membrane separation is offering an energy-efficient, low-cost manufacturing, and environmentally friendly technology, which utilizes less space and can produce consistent results. The enhancement of efficiency (i.e., permeance, selectivity, and stability) of the membrane can be improved with controlled shape and pore. Moreover, one of the important parameters to increase permeability, provide maximum throughput, and increase the performance of the membrane was the thickness of the membrane [7]. Palladium (Pd) membranes are highly efficient for hydrogen separation. Although palladium has excellent catalytic properties and can be effective in hydrogen separation, its high cost, scarcity, susceptibility to poisoning, and environmental impact present significant challenges. These issues limit its practicality and drive the search for alternative materials for hydrogen membranes.

A few years ago, the research on carbon-based membranes for H₂ separation applications tend to increase owing to their attractive properties such as high thermal and chemical stability, and higher selectivity compared to the present polymer membrane. In general, supported carbon membranes and unsupported carbon membranes are the two main categories of carbon-based membranes [8]. Both types of materials have significant disadvantages in mechanical performance, especially brittleness. Many methods have been applied to produce carbon membranes such as rotation, coating, and vacuum filtration. However, those methods were complicated to produce carbon membranes. To facilitate the fabrication of membrane for the H₂ separation and purification, a composite membrane prepared by powder sintering method has been proposed.

In this thesis, we fabricated alumina (Al₂O₃) composite membranes with the addition of four types of carbon including activated carbon, carbon black, graphene oxide and graphite by powder mixing and sintering process. The effects of carbon type and addition content on the physical properties, microstructure, pore size distribution, and the H₂ separation performance of Al₂O₃ composites membranes were investigated.

1.2 Objectives of the study

To enhance the physical and mechanical properties of porous alumina composites, carbon addition is pursued, with the aim to investigate the influence of carbon type and content on bulk density, porosity, and relative density of the composites. Furthermore, the objective includes analyzing how varying carbon type and content affect the hydrogen permeability and selectivity of alumina-carbon composite membranes.

1.3 Scopes of the study

1. Fabrication of alumina-carbon composites using four types of carbon including activated carbon, carbon black, graphene oxide and graphite.
2. Each type of carbon material was mixed with alumina at weight percentages of 0.5, 1.0, 1.5, 2.0, and 3.0. Additionally, a carbon-free specimen was used as a reference for comparison.
3. Investigation of physical properties, phase composition, microstructure, pore size distribution of alumina-carbon composites.
4. This study evaluates the hydrogen permeance and selectivity of alumina-carbon composites for application as hydrogen separation membranes. Single-gas permeation tests were conducted for both nitrogen and hydrogen gases across a temperature range of 25 to 500 °C. Transmembrane pressure differentials (ΔP) of 50-150 kPa and 25-125 kPa were employed for nitrogen and hydrogen, respectively.
5. The performance of H₂S absorption of alumina-graphene oxide was estimated through experimentation. H₂S, comprising 1% or 10000 ppm H₂S and balanced with Ar, was introduced into the reactor at a rate of 10 mL/min. The gas analyzer was employed to identify the presence of H₂S in the gas exiting the reactor.

1.4 Benefits of the study

Newly developed alumina-carbon membrane technology enables the production of high-purity hydrogen gas, offering a cost-effective alternative to the pricey palladium membrane. Additionally, the efficiency of membrane for hydrogen

This material is reserved for educational use only, not allowed for commercial use.

Forbidden to modify the content, and cite the document when use.

separation has been estimated, positioning it as a potential component in future energy systems, particularly fuel cells. In addition, hydrogen gas is also a clean fuel because when hydrogen fuel is burned, the hydrogen (H_2) reacts with oxygen (O_2) to form water (H_2O) with the release of energy. Therefore, the knowledge from this research is considered environmentally friendly research. To promote well-being and health according to the United Nations (UN) Sustainable Development Goals (SDGs), a principal of global development objectives.



This material is reserved for educational use only, not allowed for commercial use.

Forbidden to modify the content, and cite the document when use.

Chapter 2

Theory and literature reviews

2.1 Hydrogen production method

2.1.1 Natural gas to hydrogen

For the production of hydrogen, natural gas is usually used as the primary source. It is also the most popular technique of producing hydrogen today. In addition, the most widespread technology to produce hydrogen from natural gas is Steam Methane Reforming (SMR). In the steam methane reforming process, first, the gas was cleaned and then steam was mixed with gas in a steam reformer and produced CO and H₂ gas as the products. In the final products, the reaction temperature in the steam methane reforming process works at 700-800 °C. For this process, it is feasible to obtain a higher yield, like 100K tons in some situations. The reaction of the steam reforming process following the relation of equations 2.1 and 2.2 to produce hydrogen [9,10].

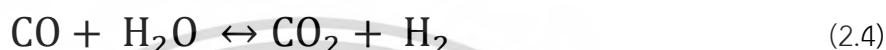


2.1.2 Coal to hydrogen

Gasification is regarded as a recognized procedure for habilitating any source of hydrocarbon into useful synthetic gas, in addition, be able to use another source such as oxygen or air in this process [11]. This method is also applied to other raw materials such as biomass, coal tar, and plastic waste which is an easy way to convert into useful gas. The coal gasification process is another fairly well-established method to produce hydrogen and many chemical fertilizer factories have been to produce ammonia, this is another advantageous byproduct of hydrogen gas [12]. Along with hydrogen-based syngas at the end of the coal-based gasification process, additional gases such as CO, H₂S, NH₃, ash, tar, HCL, and HCN [13] may also be present. The produced hydrogen gas is necessary to be purified to remove other impurities, and other elements that could reduce the calorific value of the gas. Additionally, four different types of coal-lignite, This material is reserved for educational use only, not allowed for commercial use.

Forbidden to modify the content, and cite the document when use.

sub-bituminous, bituminous, and anthracites are utilized in the gasification process and that the raw material is typically gasified at a temperature of more than 900 °C [14]. In teams producing high-quality hydrogen gas is determined by the grade and quality of coal. The production of hydrogen with the reaction with steam by the following equation [15]:



2.1.3 Biomass to hydrogen

Growing anthropogenic CO₂ emissions are a serious challenge the world is currently experiencing. To address this environmental issue, The existing power generation infrastructure must incorporate a greater proportion of renewable energy sources, such as biomass and alternative fuels, to mitigate dependence on and the adverse effects of CO₂ and other harmful emissions. Renewable energy resources extend beyond merely producing electrical power; they can also be utilized to convert one form of energy into another valuable product. Hydrogen is the one of products was attracts interest in renewable energy, which hydrogen It is not only helpful in the industrial and power sectors but also has various uses in the transportation and fuel sectors [16]. Fossil fuels are currently the dominant source of hydrogen production, accounting for over 85% of global output. However, steam methane reforming remains a highly economical method for large-scale hydrogen production [17]. Less than 5% of hydrogen has been produced using renewable resources, primarily through water electrolysis. [18].

Considered among all renewable energy sources, humans used biomass as the first option to produce energy and still being used nowadays. Biomass is derived from a variety of sources like animal wastes, wood, plants, agriculture products, etc. and that is why biomass is an interesting energy source as an alternative to fossil fuel. In terms of used hydrogen as a feedstock, most of the research focuses on lignocellulosic biomass materials such as wood, agricultural waste, energy crops, etc., mainly using thermochemical (gasification pyrolysis) conversion. The thermochemical gasification This material is reserved for educational use only, not allowed for commercial use.

Forbidden to modify the content, and cite the document when use.

process of biomass is similar to coal gasification which is the conversion of entire biomass into a mixture of H_2 , CO , CO_2 , and methane gas [19]. Thermochemical biomass conversion is a more state-of-the-art technology than any other biomass process, it includes liquefaction, pyrolysis, and gasification and holds more potential for future use [20].

Gasification is currently the most cost-effective method for producing renewable hydrogen. The efficiency of this process is approximately 50%, but there is potential for improvement. The biomass steam gasification process is endothermic and operates at high temperatures ranging from approximately 700 to 1200 °C. Additionally, H_2 and CO_2 are the primary components of the final product of the steam gasification process, which subsequently undergoes purification [21].

2.2 Hydrogen purification method

High-purity hydrogen is essential for its conversion to electrical energy in fuel cells or as a feedstock in manufacturing processes. Typically, gas separation is achieved through cryogenic distillation, pressure swing adsorption (PSA), and membrane technology. Table 2.1 provides a comparison of these hydrogen purification methods. The required quality grade of the produced hydrogen, along with the levels of specific product impurities, is crucial in determining the appropriate purification technique. The PSA process is ideal for producing high-purity hydrogen (above 99.9 vol%), whereas polymeric membrane technology offers a cost-effective alternative for obtaining hydrogen with purities ranging from 90 to 99.9 vol%, depending on the type of membrane used. Furthermore, membrane technology typically requires lower capital investment compared to cryogenic distillation and pressure swing adsorption (PSA), providing a distinct advantage.

Table 2.1 Comparison of Hydrogen Purification Techniques [22]

		unit	PSA	Distillation	Membranes
Feed requirements		H ₂ Vol%	>40	>10	>25
Product purity			99.9	90-98	90-99.9
Operating conditions	Temperature	°C	RT	-183	0-900
	Feed pressure	Bar	10-40	5-75	20-160
Hydrogen recovery		%	50-92	90-99	85-95
Productivity		Nm ³ h ⁻¹	30-400,000	10,000-90,000	<60,000
Product pressure		bar	feed	feed/low	<1/3-feed
Capacity investment			medium	high	Low

2.2.1 Pressure swing adsorption [23,24]

Pressure swing adsorption (PSA) has been applied to the chemical and petrochemical industries for high-purity hydrogen production from syngas. Globally, the current hydrogen production utilized pressure swing adsorption of more than 85% for hydrogen purification. The principal concept of the pressure swing adsorption process is relatively uncomplicated. This process relies on high partial pressures for the adsorption of impurity molecules, and these impurity molecules are subsequently removed at lower partial pressures. Thus, micro and mesoporous adsorbents were used to refine the gas mixture, in particular, zeolite. At relatively high pressure, the contaminants in the hydrogen-rich feed gas are selectively adsorbed on the surface of adsorbents. Undesired of the gas mixture was adsorbed while pure hydrogen permeated through. As the operation progresses, the impurity gases are adsorbed on the surface of adsorbents and become saturated over time. This is the reason why lowering their partial pressure results in the impurities then desorbed from the adsorbent. Although high-purity hydrogen production (approximately 99.9% in an efficient way) and hydrogen separation was widely used in the pressure swing adsorption process, the process has a number of limitations. In the pressure swing

absorption provided the recovery of hydrogen quite low. Therefore, outgas has a component large proportion of unreacted methane, CH_4 and unrecovered hydrogen. It is well known that the pressure swing absorption process does not become an affordable hydrogen purification method until it is scaled up for substantial stationary applications.

2.2.2 Cryogenic distillation [25,26]

Cryogenic distillation is a process that uses a low temperature and the cryogenic distillation working principle for the separation of gases relies on the ingredients in feed gas having different boiling points. Hydrogen production of the cryogenic separation method is derived from hydrocarbons. The boiling point of hydrogen is $-252.9\text{ }^\circ\text{C}$, which the cryogenic distillation process is provided good performance for hydrogen separation compared with other ingredients in the syngas. In this process, the purity of hydrogen obtained was approximately 90-98%, and factors such as separation pressure, working temperature, and feed gas composition determined the purity and recovery of hydrogen. Most commercial applications provide an average hydrogen recovery value of around 95%. The same as pressure swing adsorption, cryogenic distillation is relatively energy-intensive and only suitable for mass production.

2.2.3 Hydrogen separation membrane

2.2.3.1 Porous separation membrane [24,27]

Porous membranes can be fabricated from multiple materials such as ceramics, organic polymers, metals, and carbon and can utilize to separate H_2 from other gases such as CO , CO_2 , CH_4 , etc. The porous separation membrane only allows the gas molecules that smaller than the pore size of membrane can diffuse through the pores of the membrane.

Therefore, the membrane essentially functions as a molecular sieve, with its performance determined by the pore size and the relative size of the molecules to the pore distribution. One advantage of the porous membrane is that the hydrogen flux is directly proportional to the pressure difference across the membrane. In the context of hydrogen membrane separation, porous membranes have been utilized

This material is reserved for educational use only, not allowed for commercial use.

Forbidden to modify the content, and cite the document when use.

more extensively than any other material. These membranes are typically based on silica and zeolite. Recently, a membrane consisting of nearly dense SiO_2 films prepared on porous Al_2O_3 support through chemical vapor deposition (CVD) has been developed. Due to the varying pore sizes of the membrane support layers, thin films less than 1 mm in thickness were deposited to enhance permeability. In addition, the novel breed of membranes consisting of graphene oxide films onto the porous MgAl_2O_4 hollow support membranes by vacuum assisted method, the composites $\text{MgAl}_2\text{O}_4/\text{GO}$ membrane exhibited to enhance the ideal selectivity of hydrogen/carbon dioxide. In addition, the summary of the permeabilities and selectivity of different porous membranes for hydrogen separation are listed in Table 2.2.

Table 2.2 Characteristics of certain porous membranes used for hydrogen separation [28].

Membrane	Preparative method	Support	H_2 permeance ($10^{-8} \text{ mol m}^{-2} \text{ s Pa}$)	H_2 selectivity
Silica	CVD (TEOS)	Alumina	2.2 (at 500°C)	$\text{H}_2/\text{N}_2 = 1000$
	Sol-gel	Alumina	112 (at 200°C)	$\text{H}_2/\text{CH}_4 = 5000$
SiC	CVD	Alumina	60 (at 400°C)	$\text{H}_2/\text{H}_2\text{O} = 5$
Carbon	UD (PFFA)	Alumina/glass	10.6 (at 150°C)	$\text{H}_2/\text{N}_2 = 30$
Zeolite	ZSM-5	Alumina	4.4 (at 190°C)	$\text{H}_2/n\text{-C}_4\text{H}_{10} = 14$

The carbon-based membrane has garnered significant interest in hydrogen separation applications due to its superior sieving properties, offering higher thermal and chemical stability as well as excellent selectivity compared to existing polymer membranes. Carbon membranes generally fall into two main categories: supported and unsupported.

Unsupported carbon membranes can have flat, capillary, or hollow structures. Among these, hollow fiber unsupported carbon membranes have been extensively studied for their hydrogen selectivity, owing to their low material costs and excellent separation performance relative to other membranes. However, the brittleness of hollow fiber membranes directly impacts their hydrogen separation efficiency.

Supported carbon membranes are typically categorized into two designs: flat and tubular. These designs are widely employed in separation processes due to their superior separation efficiency and mechanical resilience. However, a notable drawback of carbon and porous membranes lies in their mechanical properties, particularly their brittleness. In unsupported carbon membranes, this issue is addressed by subjecting them to multiple carbonization cycles and depositing multiple layers of polymers. Both supported and unsupported materials can undergo processes for the preparation of carbon membranes.

Various methods have been utilized to produce supported carbon membranes, including vacuum assistance, spray coating, and rotation coating. The top layer of the membrane serves to control gas selectivity, while the porous supporting materials enhance gas permeation and strengthen the membrane. However, a significant challenge with supported carbon membranes is the interface between the membrane and its fabrication step. To mitigate this issue, modified porous supports can be prepared prior to coating. Table 2.3 summarizes the hydrogen permeation and selectivity of the carbon layer, specifically graphene oxide (GO), on the porous support.

Table 2.3 Performance characteristics such as hydrogen permeance, ideal H₂/CO₂ selectivity, and ideal H₂/N₂ selectivity of graphene oxide (GO) membranes [29].

Membrane/Support	Method	H ₂ permeance (mol m ⁻² s ⁻¹ Pa)	H ₂ /N ₂	H ₂ /CO ₂
GO/ α -alumina-hollow fiber	VDC	1.2×10 ⁻⁶	6	16.7
GO/polymeric pellet	VDC	1×10 ⁻⁷	3.2	-
GO/YSZ-hollow fiber	VDC	4.48×10 ⁻⁸	64	-
GO/AAO pellet	VDC	5.1×10 ⁻⁷	-	48
GO/TiO ₂ -alumina-Tubular	VDC	0.3×10 ⁻⁶	9	26

Note: VDC is Vacuum Dip Coating

2.2.3.2 Polymeric separation membrane [7].

Polymer membranes have been widely utilized in various industrial gas separation processes. One method for transporting hydrogen through these membranes is the solution-diffusion mechanism, which differs from methods involving photon-

conducting membranes or dense metals, as it does not require hydrogen dissociation and re-association steps. Typically, polymeric membranes operate at temperatures around 100°C, although in certain conditions, temperatures may reach up to 200°C. Polymeric membranes can be categorized into two main types: glassy and rubbery. Glassy membranes generally exhibit higher selectivity but lower hydrogen flux compared to rubbery membranes. Table 2.4 presents data on hydrogen permeability and selectivity relative to nitrogen (N₂), methane (CH₄), and CO₂ for polymeric membranes.

However, when comparing polymeric membranes, the hydrogen permeability and selectivity are much lower than the dense metallic membrane. Polymeric membranes are susceptible to contamination when H₂S, HCl, and CO₂ gases are presented. As a result, polymeric membranes are less attractive than other dense membranes.

Table 2.4 Hydrogen permeabilities and selectivity of the polymer membranes [30].

polymer	Hydrogen Permeability Barrer ^a	Selectivity		
		H ₂ /N ₂	H ₂ /CH ₄	H ₂ /CO ₂
Polysulfone	121	15.1	30.3	2.0
Polystyrene	23.8	39.7	29.8	2.3
Polymethyl methacrylate	2.4	2.0	4.0	4.0
Polyvinylidene fluoride	2.4	3.4	1.8	2.0

^aNote: 1 Barrer = 10⁻¹⁰ cm³(STP)cm/(cm² s cm Hg) where STP) standard temperature and pressure

2.2.3.3 Dense ceramic ion transport membrane [31–33]

Dense ceramic membranes with mixed ion and electron transport capabilities are increasingly recognized in hydrogen separation technologies. At high partial pressures, hydrogen transport occurs through the dissociation of protons and electrons from hydrogen molecules. These protons and electrons then migrate through the dense membrane and recombine on the low partial pressure side. The membrane surface plays a crucial role by facilitating charge transfer reactions on both sides of its exterior surfaces. The layers of alternative catalytic or electrodes are necessary to promote

This material is reserved for educational use only, not allowed for commercial use.

Forbidden to modify the content, and cite the document when use.

hydrogen dissociation and reassociation processes. The selectivity of hydrogen was exceptionally high, exceeding 99%, and isolated hydrogen does not require any additional purification. The schematic illustration of hydrogen transport through the dense ceramics ion transport membrane is illustrated in Figure 2.1.

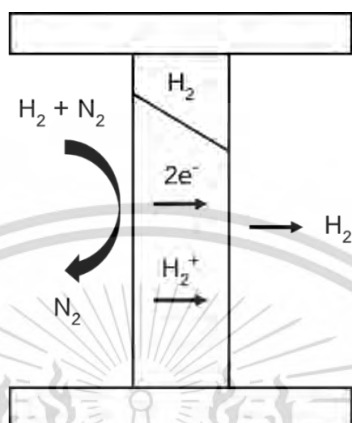


Figure 2.1 Schematic of hydrogen transport in ion transport membranes [34].

Most of the work to current has been operated on perovskite-type oxide, with a general formula of ABX_3 , where A and B represent cations and X represent anion. Perovskite phases are quite attractive owing to the component of ionic and electronic conductivity. Materials based on $BaCeO_3$ and $SrCeO_3$ are the p-type or hole conductors of perovskite structure with free hydrogen or water vapor. However, in the presence of hydrogen and water vapor, they improved performance via reducing electrical conductivity while increasing proton conductivity. Maintaining electroneutrality in the perovskite structure of $BaCeO_3$ and $SrCeO_3$ is essential for creating oxygen vacancies. This can be achieved by doping with an aliovalent cation at the B site in the perovskite formula. Elements such as Y, Yb, and Gd can substitute some Ce in the lattice, thereby generating the necessary oxygen vacancies. These vacancies plays a significant role in proton conduction. The combination of high proton conductivity and thermodynamic stability, essential prerequisites for use as a hydrogen separation membrane, is a property exhibited by relatively few perovskites such as $BaCeO_3$. While some oxides may exhibit suitable proton conductivity properties, their chemical stability under real operating environments is often inadequate. Research efforts are currently underway to address some of these challenges. The membrane deterioration would cause the

This material is reserved for educational use only, not allowed for commercial use.

Forbidden to modify the content, and cite the document when use.

hydrogen flux rate to decrease. In general, the strength and chemical stability of the materials were different depending on the function of the composites and temperature of the sintering, and mush clouds are considered when selecting the smashing denser membrane for high performance of hydrogen separation application. Table 2.5 illustrates the information on the optimal conducting temperature and proton conductivities for dense proton conducting-based materials.

Table 2.5 Conductivities of promising proton-conducting materials for hydrogen separation membranes [35].

Material	Optimal conducting temperature (°C)	Proton conductivity (s/cm)
$H_4SiW_{12}O_{40} \cdot 28H_2O$	<100	2×10^{-2} at 25 °C
$H_3PW_{12}O_{40} \cdot 29H_2O$	<100	8×10^{-2} at 25 °C
$H_3PMo_{12}O_{40} \cdot 29H_2O$	<100	1.7×10^{-2} at 25 °C
$Sb_2O_5 \cdot 4H_2O$	<300	3×10^{-4} at 25 °C
$V_2O_5 \cdot nH_2O$, $ZrO_2 \cdot nH_2O$,	<150	1×10^{-2} at 100 °C
Sr doped $La_3P_3O_9$	700	$7 \times 10^{-7} - 3 \times 10^{-4}$ at 300-700 °C
Sr doped $LaPO_4$ (wet atm)	500–925	$6 \times 10^{-6} - 3 \times 10^{-4}$ at 500-925 °C
$CsHSO_4$	100–200	$2 \times 10^{-7} - 3 \times 10^{-2}$ at 110-190 °C
H_3OClO_4	100–200	3.5×10^{-4} at 25 °C
$MeNO_3 - SiO_2$ (Me = Rb, Cs)	100–200	$1 \times 10^{-6} - 1 \times 10^{-2}$ at 60-280 °C

2.2.3.4 Dense metallic membranes [36,37]

Dense metallic membranes are commonly employed for hydrogen separation within a temperature range of 300-600 °C. Research on dense metallic membranes has focused notably on alloys based on V, Nb, and Zr, as well as several amorphous alloys which serve as cost-effective alternatives. Examples include Ni-Nb-Zr amorphous alloys, Cu-Zr binary amorphous alloys, V-Al alloys, and V-Ni alloys. The mechanism involved in hydrogen separation through these metal

membranes is often described as the "solution-diffusion" mechanism. A comparative analysis of different membrane types is illustrated in Figure 2.2.

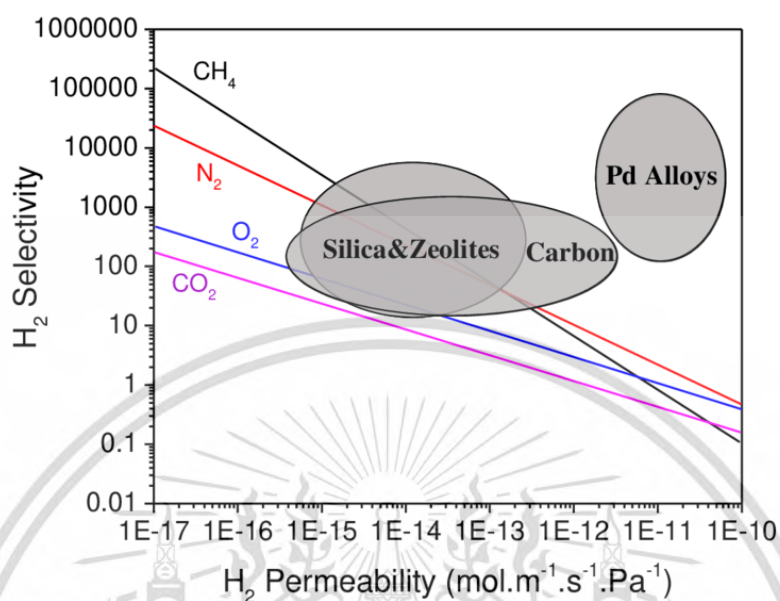


Figure 2.2 Hydrogen selectivity versus permeability of different separation membranes [38].

A dense metallic membrane can produce hydrogen with an increase of 99.999% of purity. In addition, the recovery ratio of hydrogen can reach a very high level, equal to or greater than 95% under some conditions. Metallic membrane often displays reasonable hydrogen permeability over a large temperature range between 300 and 700 °C. In addition to membrane thickness and temperature, the efficiency of hydrogen permeation through membranes also depends on hydrogen diffusion and solubility. Typically, permeation flow disregards surface effects and is proportional to the square root of the pressure difference. However, the catalytic capability of the membrane surface to dissociate and re-associate hydrogen is crucial for metal membranes to function effectively. When these reactions occur too slowly, a catalytic layer is often added to enhance the dissociation and re-association processes. Metal membranes are preferred for hydrogen separation due to their high permeation rates, offering increased flux. However, higher permeability often correlates with greater susceptibility to hydrogen embrittlement. Therefore, selecting the optimal metal for a hydrogen separation membrane involves balancing high permeability with resistance to hydrogen

embrittlement. Table 2.6 provides data on hydrogen permeability and enthalpy of formation (ΔH) for various metals.

Table 2.6 Hydrogen permeability and ΔH formation (of hydrides) data for selected Metals [28].

Metals	Crystal structure ^a	H ₂ permeability at 500 °C (mol/m s Pa ^{1/2})	ΔH formation (of hydrides) (KJ/mol)
Platinum, Pt	fcc	2.0×10^{-12}	+26 (Pt-H)
Palladium, Pd	fcc	1.9×10^{-12}	+20 (Pd ₂ -H) ^b
Nickel, Ni	fcc	7.8×10^{-12}	-6 (Ni-H _{0.2})
Copper, Cu	fcc	4.9×10^{-12}	-
Iron, Fe	bcc	1.8×10^{-12}	+14 (Fe-H)
Tantalum, Ta	bcc	1.3×10^{-12}	-78 (Ta-H _{0.5})
Niobium, Nb	bcc	1.6×10^{-12}	-60 (Nb-H ₂)

^abcc, is body-centred cubic and fcc, face-centred cubic

^binformation from Kelton, K. F. et al., J. Non-Cryst. Solids 317 (2003). 71.

2.2.3.5 Carbon-based membranes [39]

Carbon-based membranes have gained considerable attention in hydrogen separation applications because of their sieving properties, which offer superior selectivity and greater chemical and thermal stability compared to current polymer membranes. Carbon membranes can generally be classified into two primary types: unsupported carbon membranes and supported carbon membranes [40]. Unsupported carbon membranes can be configured as flat, capillary, or hollow. Hollow fibers are typically favored for hydrogen separation due to their low material cost, high packing density, and excellent separation performance. However, their brittleness can sometimes hinder their effectiveness. Carbon materials, which include a wide variety of substances rich in carbon atoms, exhibit a range of structures, properties, and applications. These materials are crucial in numerous fields such as industry, technology, and membrane research. Common forms of carbon materials include activated carbon, carbon black, graphene oxide, and graphite.

This material is reserved for educational use only, not allowed for commercial use.

Forbidden to modify the content, and cite the document when use.

2.2.3.5.1 Activated carbon [41–43]

Activated carbon is recognized as an effective and trustworthy material for impurity and pollution removal applications. It demonstrated the excellent performance as an adsorptive capacity, this versatility has led to its widespread use in various industrial applications, including gas purification technologies, the removal of organic pollutants from water (such as in drinking water and wastewater purification), and medical applications. The main raw materials for producing activated carbon are organic substances with high carbon content, such as coal, wood, peat, and coconut shells. The process of converting carbon-based material into activated carbon involves thermal decomposition in a furnace under controlled atmospheric conditions and heat, or through alternative physical and chemical methods. The resulting product possesses an exceptionally large surface area per unit volume, along with a network of submicroscopic pores where adsorption occurs. The pore walls play a crucial role by providing the necessary surface layer molecules for adsorption. In simple terms, physical adsorption happens because molecules exert attractive forces, particularly those at the surface of a solid, which seek other molecules to stick to. The extensive internal surface area of carbon contains numerous attractive forces that draw in other molecules. Activated carbon has shown that using it in membrane bioreactors achieves high removal performance for organic pollutants in both synthetic and real wastewater.

2.2.3.5.2 Carbon black [44,45]

Carbon black is a nanostructured material composed of almost pure carbon, typically exceeding 95% in elemental content. It usually appears as fine, quasi-spherical particles, known as "primary particles," which are interconnected by covalent bonds to create aggregates and agglomerates. The average diameter of primary particles ranges from several tens to several hundred nanometers, depending on the production process. It is crucial to distinguish between carbon black and soot: the former is intentionally produced under controlled conditions for numerous commercial applications, is almost ubiquitous in modern society, and is valued at around \$1000 USD per metric ton. In contrast, soot is an unwanted byproduct of combustion, posing health risks and environmental hazards. Despite these differences, both types of carbonaceous nanomaterials typically originate from similar growth

This material is reserved for educational use only, not allowed for commercial use.

Forbidden to modify the content, and cite the document when use.

mechanisms. The properties of carbon black are heavily influenced by synthesis conditions such as feedstock, heating medium, thermal histories, and reactor configurations. Industrial applications rely on numerous physicochemical parameters, which will not be detailed here. Recently, Robertson and Hardman have concentrated their research on the nature of carbon black and its interactions with rubber. In addition, the hydrophobic nature of carbon black also restricts water transport across its surface.

2.2.3.5.3 Graphene oxide [46–49]

Graphene oxide (GO) was first reported by Schafhaeuti in 1840 and by Brodie in 1859. Over the years, various synthesis methods have been developed, but the most standard approach is based on the method proposed by Hummers and Offeman. This involves oxidizing graphite to graphite oxide using a mixture of concentrated sulfuric acid, sodium nitrate, and potassium permanganate. This method has been refined and is known as the modified Hummers method, although the basic strategy remains unchanged. GO is an insulating material, though disordered, similar to conducting crystalline graphene. The structure of GO is still a topic of debate. Early studies suggested structural models of GO with a regular lattice composed of discrete repeat units, but the widely accepted model was proposed by Lerf and Klinowski based on an in-depth nuclear magnetic resonance (NMR) study. This model features a carbon grid of aromatic or aliphatic six-membered rings with sp^2/sp^3 regions containing basal hydroxyl and epoxy functional groups, as well as carboxylic acid groups along the sheet edges. Graphene oxide (GO), consisting of mono- or few-layered stacks, is produced by oxidizing graphite followed by exfoliating graphite oxide, as depicted in Figure 1.10b. The C/O and C/H ratios of GO are heavily influenced by the starting graphite material and the specific oxidation process used during synthesis. Factors such as the chemical composition and relative amount of the oxidizing agent, the temperature and duration of the process, and the presence and type of activation factor (e.g., $SOCl_2$ or a carbodiimide, which activates the edge carboxylic acid groups) all play significant roles. GO is decorated with covalently bound oxygen-containing groups. It features sheets with both trigonal-bonded sp^2 carbon atoms (perfectly flat) and tetrahedrally bonded sp^3 carbon atoms (slightly displaced above or below the

This material is reserved for educational use only, not allowed for commercial use.

Forbidden to modify the content, and cite the document when use.

graphene plane, making it atomically rough). High-resolution studies using annular dark field in scanning transmission electron microscopy (ADF-STEM) and scanning tunneling microscopy (STM) have shown that the oxidation degree of a GO monolayer fluctuates at the nanometer scale, with random-sized sp^2 and sp^3 clusters and highly defective regions caused by the displacement of carbon atoms by oxygen functional groups. Despite consisting of only three chemical elements (C, H, and O), GO can have numerous oxygen-containing functional groups attached to its nanosheet, allowing for modulation of its properties for various applications. Graphene's structure has made it a highly sought-after membrane material due to its atomic thickness, scalable size, excellent mechanical strength, chemical robustness, and the ability to engineer selective nanopores in its rigid yet flexible crystal lattice. Compared to other carbon or inorganic materials, graphene's availability as a large-area membrane sheet and its impermeability have spurred researchers to explore its use in membrane-based gas separations. The significant interest in graphene and its derivatives needs to be matched by persistent efforts to develop new membrane materials with superior performance in terms of permeance and selectivity for more energy-efficient processes.

2.2.3.5.4 Graphite [50–52]

Graphite is soft, conducts electricity, and is opaque to visible light (gapless semi-metal), whereas diamond, the hardest known material, is an electrical insulator and transparent to light (wide bandgap). The most extensively studied allotrope of elemental carbon is monocrystalline graphite. The first X-ray studies of graphite's crystal structure were conducted in 1924 by Bernal, who demonstrated that graphite is a three-dimensional layered material with a small inter-atomic spacing within the layer (1.42 Å) compared to the spacing between the lattice planes (3.35 Å). Within a layer, carbon atoms are arranged in a planar, hexagonal lattice. The band structure model of graphite was developed in the 1950s by Slonczewski, Weiss, and McClure, building on earlier work by Wallace, and is known as the SWM model. As the membrane application, graphite-based materials exhibit a diverse array of gas diffusion mechanisms influenced by factors such as pore diameter, the ratio of open to closed porosity, and the structural anisotropy.

Carbon-based membrane materials, such as activated carbon membranes, carbon black membranes, graphene-based membranes, and graphite membranes, are being explored for highly efficient water and wastewater treatment as well as gas separation. Various approaches, including surface modification, optimization of operational parameters, and the combination of different technologies, are employed to enhance membrane performance. These efforts have yielded significant results and advanced the field considerably. Although these carbon-based membrane materials show promising potential in water treatment, further studies are necessary to realize their viability for gas separation and their commercial application.

2.3 Mechanisms for gas separation

The key mechanisms for the separation of gas mixture across a porous membrane were Knudsen diffusion, Poiseuille (Viscous) flow, capillary condensation, selective adsorption, and molecular sieving and one of the important mechanisms for gas separation was single-file diffusion. In Figure 2.3, the different mechanisms of gas separation are depicted schematically. The properties of the membranes and the gases determine the relationship between the different gas separation mechanisms, as well as the working parameters such as temperature and pressure.

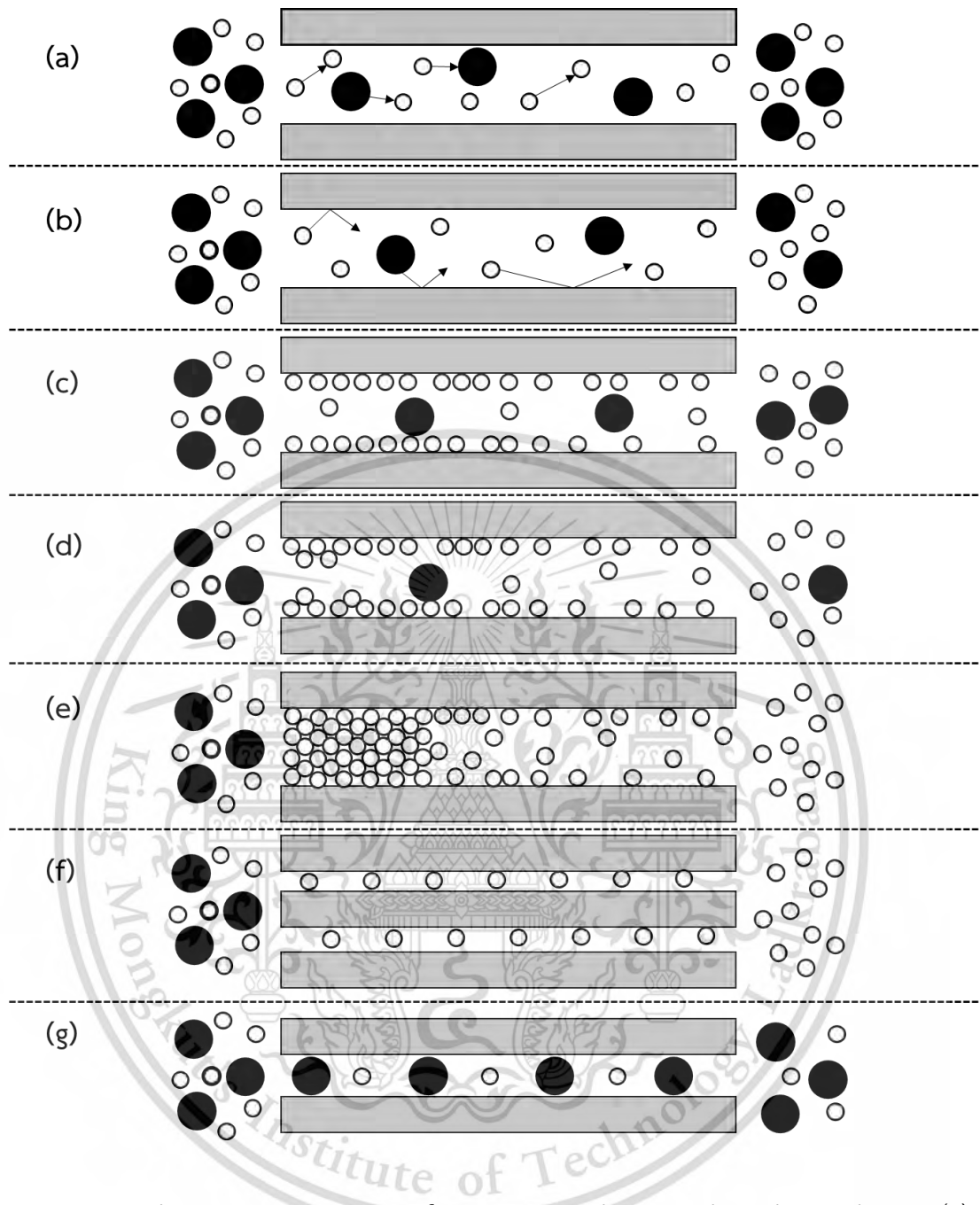


Figure 2.3 Schematic presentation of transport mechanisms through membranes (a) Poiseuille flow, (b) Knudsen diffusion, (c) Surface diffusion, (d) multi-layer diffusion, (e) Capillary condensation, (f) Molecular sieving, and (g) Single-file [53].

2.3.1 Knudsen Diffusion

In Knudsen diffusion, the differences in molar masses of gases in the main mechanism of separation through the pores. This mechanism of transportation occurs when the size of the pore (r) was smaller than the mean free path (the average distance a gas molecule will move between successive collisions or impacts) of the

This material is reserved for educational use only, not allowed for commercial use.

Forbidden to modify the content, and cite the document when use.

molecule at the processing condition. The mean free path λ is provided following equation:

$$\lambda = \frac{3\eta (\pi RT)^{0.5}}{2P \quad 2M} \quad (2.5)$$

where η is the viscosity of the gas, R is the gas constant of gas universal, T is the absolute temperature, M is the molar mass, and P is the pressure. If r/λ is much lower than one ($r/\lambda < 0.5$), the collisions with the pore walls are more important than the collision with the other gas molecules. The less value of collisions among molecules than the collisions with pore walls indicates that each gas molecule moves independently. Therefore, the separation of gases was done by the difference in the velocity of different gas molecules. The gas flux following the Sieverts' law was defined by:

$$G_{mol} = \frac{8r(P_1 - P_2)}{3L(2\pi MRT)^{0.5}} \quad (2.6)$$

where G_{mol} is the molecular flow of gas, r is the radius of the pore, P_1 and P_2 are the partial pressure of the gas on the feed and permeate side, respectively, L is the length of the pore, M is the mass of molar, R is the gas constant, and T is the temperature. The ideal selectivity or separation factor (S_F) of the Knudsen mechanism is usually estimated using the square root of the molecular weight-to-weight ratio.

$$S_F = \left(\frac{i}{j}\right) = \sqrt{\frac{M_i}{M_j}} \quad (2.7)$$

where M_i and M_j are the permeability of the two pure gasses, respectively, which i instead of the higher permeable gas.

2.3.2 Poiseuille (Viscous Flow)

Poiseuille flow happens when the pore size of the membranes is much bigger than the mean free path i.e. ($r/\lambda > 3$). In this scenario, molecule–molecule collisions
This material is reserved for educational use only, not allowed for commercial use.

Forbidden to modify the content, and cite the document when use.

are primarily of those gas diffusion. If a pressure gradient was applied to such a pore area, laminar and bulk flow would occur. In the literature, Poiseuille flow is also known as bulk diffusion or viscous flow, for the gas separation membrane, this phenomenon was unfavorable. The permeability is provided by the following formula:

$$Q_V = \frac{J_V}{\Delta P} = \frac{\varepsilon r^2}{8\tau\mu RT} P_m \quad (2.8)$$

where J_V is viscous flow, ΔP is the pressure differential transported across the membrane, ε is porosity, τ is tortuosity factor, μ is the factor of gas, and P_M is the mean pressure. P_M can be calculated by the following:

$$P_m = \frac{P_1 + P_2}{2} \quad (2.9)$$

Where P_1 is the inlet pressure and P_2 is the outlet pressure.

2.3.3 Capillary Condensation

The excellent enhancement of permeability performance through the capillary condensation mechanism may occur when one of the gases in the mixture condenses as vapor through the mesoporous membrane, resulting in high selectivity. Mesoporous pores with a diameter of more than 3 nm are often required for this mechanism to provide sufficient area for condensation of the gas mixture. However, surface diffusion can happen simultaneously with capillary condensation because the same conditions that lead to capillary condensation also induced significant surface diffusion.

2.3.4 Selective Adsorption / Surface Diffusion

Selective adsorption is one of the mechanisms observed, wherein a gas mixture is more strongly absorbed onto the pore surface, followed by the molecules of the gases undergoing surface diffusion within the pore, thereby facilitating the separation of gases. This mechanism offers a highly practical and attractive option for particle separation. It involves the adsorption of molecules from the mixed gas onto the

membrane pores surface, with certain components exhibiting extraordinary adsorption. This characteristic plays a crucial role in determining separation selectivity.

In the presence of firmly adsorbed components, it has been observed that the permeance of weakly adsorbed components is drastically reduced. A number of scientific research articles demonstrated the benefit of gas separation based on the strongly adsorbed components' surface diffusion and their restriction of the permeance of the weakly or non-adsorbed components. Also, when gas molecules permeating via adsorption on the pore wall of the membrane becomes significant, their mobility on the surface of the membrane can become highly significant. This can be considered to enhance the performance of gas transport. Surface diffusion capacity was determined by an adsorption equilibrium and surface coefficient, both of which correspond to the interactions of adsorbents and the surface of the pore. Moreover, surface diffusion becomes significant when the size of the pore becomes as small as the gas molecules in permeating experiment, owing to the physicochemical interactions between the permeating molecules and the pore wall turn into more pronounced.

2.3.5 Molecular Sieving

The molecular sieve of separation based is caused via the smaller molecules of the mixed gas passage through the pores of the membrane while the larger molecules (more than pores size) are hindered. In order to function as a molecular sieve, the first thing to consider is the pores size of the membrane. The pore diameters of the membrane must have the value between those of the gas molecules also to be separated. Therefore, if the pore size of the membranes is between the diameter of smaller and larger molecules, then only the smaller molecule gases can permeate, and the high performant of separation would be achieved. In actual circumstances, membranes typically exhibit a distribution of pore sizes. Consequently, gas permeability is greatly influenced by a combination of transport mechanisms.

2.3.6 Configurational / Micropore Diffusion

This type of diffusion is termed surface diffusion when the molecular size of the gas approaches that of the membrane pore size, leading to restrictions. In this mechanism, the transition occurs from Knudsen diffusion to configurational diffusion.

This material is reserved for educational use only, not allowed for commercial use.

Forbidden to modify the content, and cite the document when use.

This mechanism occurs when the channel diameter approaches that of the molecules. This diffusion is perceived as an “activated” process, where the molecular size and shape, pore size, and the interaction of the gas molecules and pore wall are the important parameters for separation. This kind of mechanism is outstanding in the carbon molecular sieve and microporous zeolite membranes.

2.3.7 Single File Diffusion

This mechanism of diffusion happens when the diameters of the pore of the membrane were not large enough to allow the molecules of gas to transport through one another. The limit of the single file mechanism, the boundary effect is important owing to only the gas molecules at the surface are capable of exchanging with the surrounding fluid. Single file diffusion does not permit reciprocal exchange between adjacent molecules. This only becomes a problem when different molecule types are considered.

2.4 Literature review

2.4.1 Disk membrane

Li et. al. [54] prepared the single-layered graphene oxide flakes via the modified Hummer's method. The ultrathin graphene oxide membranes were deposited on anodic aluminum oxide (AAO) disk support. The fabrication process for graphene oxide membrane is shown in Figure 2.4. In addition, the hydrogen permeance and the selectivity of the membranes are shown in Figure 2.5. This membrane exhibited a high H_2/N_2 selectivity of 900, indicating molecular sieving behavior due to an intrinsic defect, while the H_2 permeance was estimated to be $10^{-8} \text{ mol s}^{-1} \text{ m}^{-2} \text{ Pa}^{-1}$.

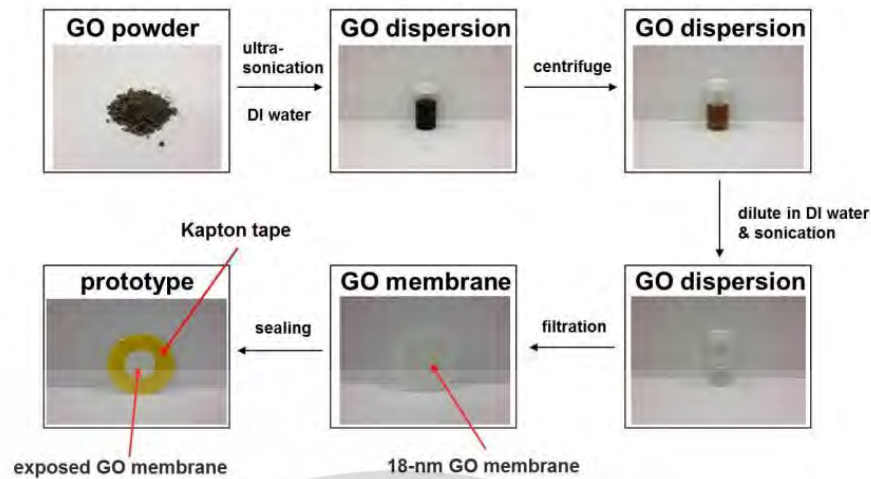


Figure 2.4 Fabrication process for graphene oxide membrane [54].

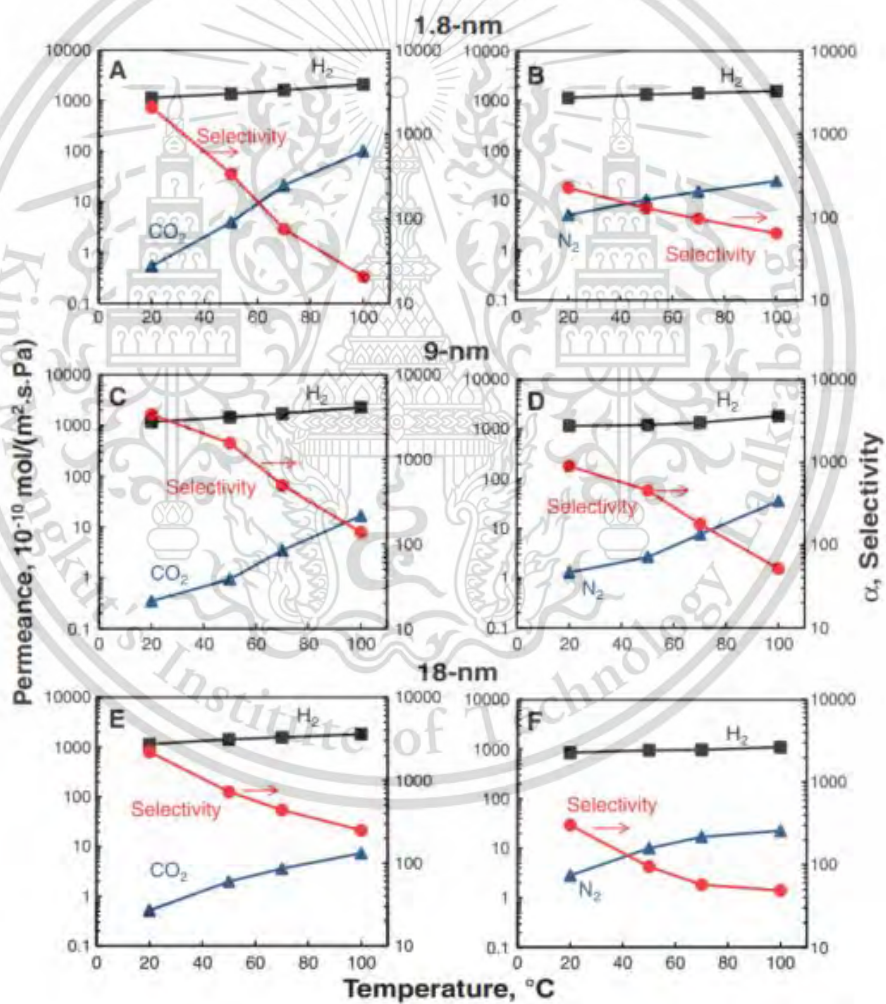


Figure 2.5 (A) and (B) the separation results for a 1.8-nm-thick GO membrane, (C) and (D) the separation results for 9-nm membrane, and (E) and (F) for an 18-nm membrane [54].

2.4.2 Tubular membrane

Zeynali et al. [55] coated the GO layer on a modified TiO₂-alumina tubular substrate by vacuum. The two GO concentrations of 1 mg/ml (sample 1) and 0.01 mg/ml (sample 2) were used in this research. Figure 2.6 demonstrates the various nanocomposite GO membrane samples prepared with different GO solution concentrations. The hydrogen permeation and selectivity of H₂/CO₂ and H₂/N₂ were investigated as a function of temperature between the range 283–473 K and transmembrane pressure was 1.0 bar. Figure 2.7 showed the hydrogen permeation and H₂/CO₂ selectivity of membranes as a function of temperature. Figure 2.8 showed the hydrogen permeation and H₂/N₂ and H₂/CO₂ selectivity of membranes as the function of pressure gradient. The results show that, as the function of temperature increased, the hydrogen permeance tended to decrease. The higher hydrogen permeation was $0.6 \times 10^{-6} \text{ mol s}^{-1} \text{ m}^{-2} \text{ Pa}^{-1}$ and $4.6 \times 10^{-6} \text{ mol s}^{-1} \text{ m}^{-2} \text{ Pa}^{-1}$ at 473K for sample 1 and sample 2, respectively. The performance of hydrogen permeation of sample 2 provides better efficiency than sample 1. In addition, as the function of pressure the hydrogen permeance was increased as the function of pressure increased.



Figure 2.6 Pictures of GO membrane samples; (a) sample 1 and (b) sample 2 [55].

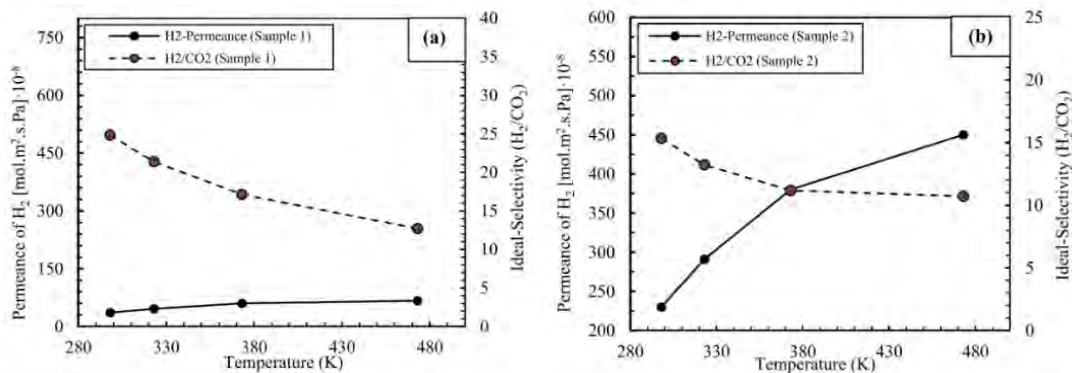


Figure 2.7 Hydrogen permeance and H_2/CO_2 selectivity for GO membrane samples at transmembrane pressure of 1.0 bar; (a) sample 1 and (b) sample 2 [55].

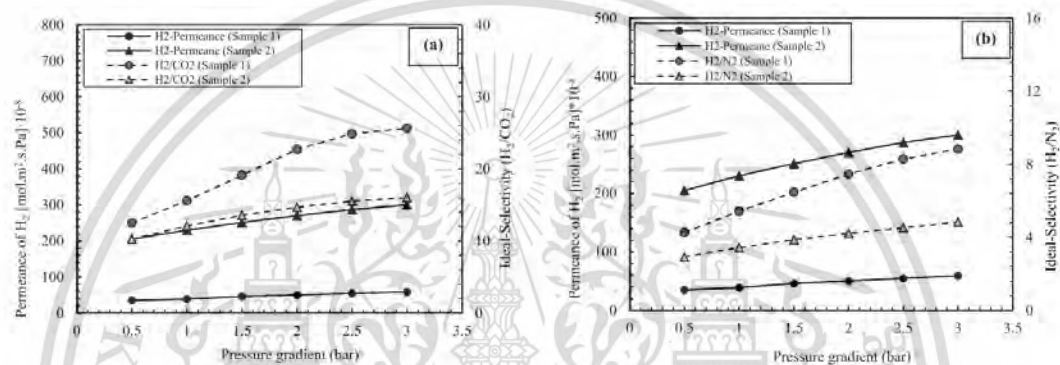


Figure 2.8 H_2 permeance for GO membrane samples and (a) H_2/CO_2 ideal selectivity and (b) H_2/N_2 ideal selectivity vs transmembrane pressure at room temperature [55].

2.4.3 Hollow fiber membrane

Ribeiro et al. [56] reported the graphene oxide membrane for the purification of hydrogen application. The GO membrane was prepared via a vacuum-assisted method on asymmetric spinel ($MgAl_2O_4$) hollow fibers. Figure 2.9 shows the spinel hollow fibers membrane, GO, and composites $MgAl_2O_4/GO$ membrane. In addition, Figure 2.10 shows the images of cross-section of $MgAl_2O_4/GO$ membrane and the surface of GO by SEM and AFM. Graphene oxide layers were well-adhered to the spinel hollow fibers as a homogeneous layer. Figure 2.11 shows the result of single gas permeation of N_2 , H_2 and CO_2 for the prepared $MgAl_2O_4/GO$ composite membrane. The experiment was conducted at $25^\circ C$ and the transmembrane pressures were varied from 0.15 to 0.30 MPa. The hydrogen permeation through $MgAl_2O_4/GO$ membrane was $8.2 \times 10^{-7} \text{ mol s}^{-1} \text{ m}^{-2} \text{ Pa}^{-1}$ and the H_2/N_2 and H_2/CO_2 selectivity values were 3.3 ± 0.0 and 11.4 ± 0.1 , respectively.



Figure 2.9 The spinel hollow fibers membrane, GO and $\text{MgAl}_2\text{O}_4/\text{GO}$ composites membrane [56].

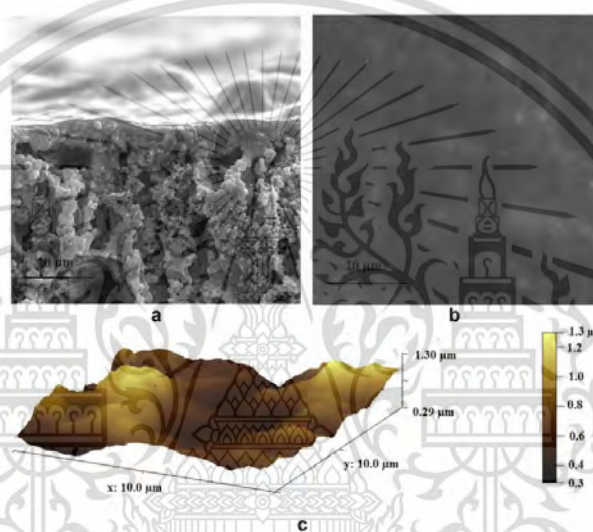


Figure 2.10 SEM images of (a) cross-section of the spinel hollow fiber and (b) surface of GO image, and (c) AFM image of GO surface layer [56].

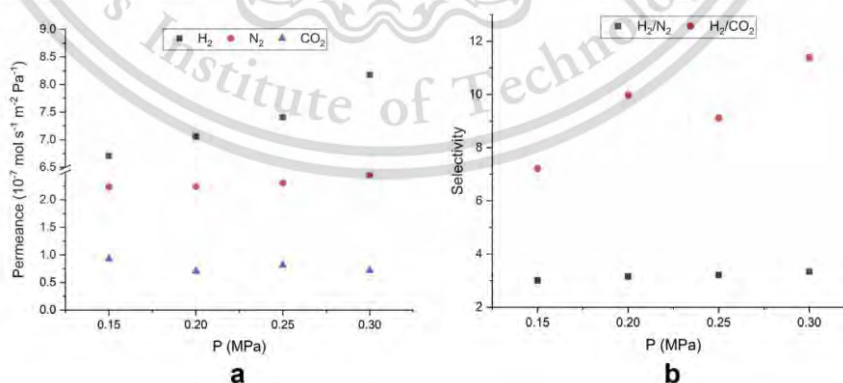


Figure 2.11 (a) Individual gas permeance data and (b) the ideal selectivity values for gas permeations through the $\text{MgAl}_2\text{O}_4/\text{GO}$ composite membrane [56].

Ma et al. [57] produced a sodium dodecylbenzene sulfonate (SDBS) modified GO layer on the Al_2O_3 hollow fibers, in which the graphene oxide membranes layer was prepared via vacuum method. The physical characterization of GO on Al_2O_3 hollow fibers is presented in Figure 2.12. The thickness of the graphene oxide layer is approximately 300–334 nm. The single gas permeation of $\text{GO-SDBS@Al}_2\text{O}_3$ is shown in Figure 2.13. At room temperature, the hydrogen permeation through $\text{GO-SDBS@Al}_2\text{O}_3$ was $0.81 \times 10^{-7} \text{ mol s}^{-1} \text{ m}^{-2} \text{ Pa}^{-1}$ and the H_2/N_2 and H_2/CO_2 selectivity values were of 28 and 323, respectively. During the continuous permeation process for more than 100 h, the two GO-SDBS membranes showed stable permeation of H_2/N_2 and H_2/CO_2 without indication of performance deterioration.

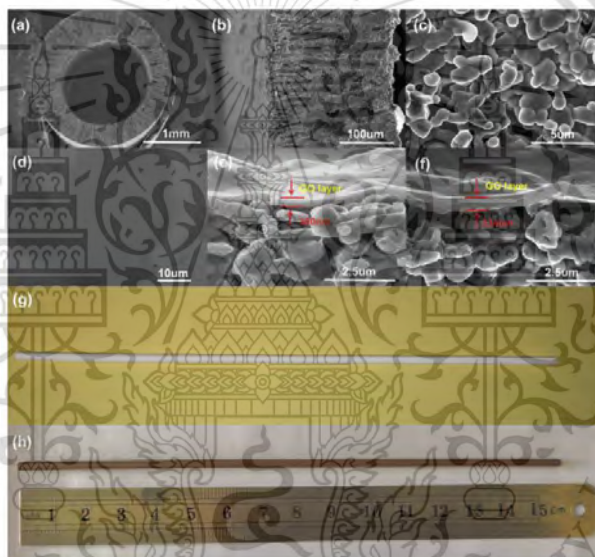


Figure 2.12 (a) SEM image of alumina hollow fiber membrane, (b) cross section, (c) magnification diagram for b, (d) SEM image of GO sheet used for membrane preparation, (e) SEM images of GO membrane without SDBS: $\text{GO@Al}_2\text{O}_3$, (f) SEM image of $\text{GO-SDBS@Al}_2\text{O}_3$, (g) macroscopical photos of alumina hollow fiber, (h) macroscopical photos composite membrane [57].

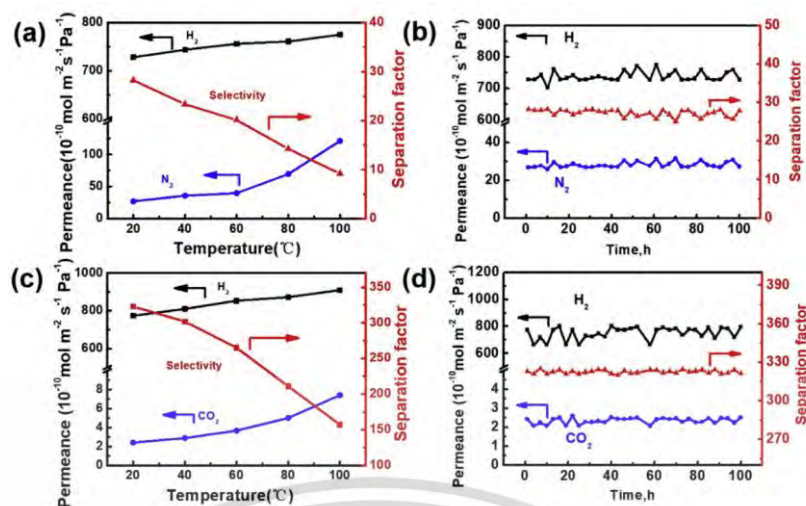


Figure 2.13 (a) Temperature dependent H₂ and N₂ permeances and the respective separation factor of GO-SDBS@Al₂O₃ for H₂/N₂ mixture, (b) time dependent of H₂ and N₂ permeances and H₂/N₂ separation factor of GO-SDBS@Al₂O₃ membranes, (c) Temperature dependent H₂ and CO₂ permeances and the respective separation factor of GO-SDBS@Al₂O₃ for H₂/CO₂ mixture, (d) Time dependent H₂ and CO₂ permeances and H₂/CO₂ separation factor of GO-SDBS@Al₂O₃ membrane [57].

2.4.4 Composite membrane

Kim et al. [58] fabricated and evaluated hydrogen permeation on TiN-graphene membrane prepared by hot press sintering (HPS) process. As shows in Figure 2.14, at 473–673 K, hydrogen permeability of this membrane was evaluated to be $2.78\text{--}2.83 \times 10^{-7} \text{ mol s}^{-1} \text{ m}^{-2} \text{ Pa}^{-1}$ at 473–673 K under 0.1 MPa, $2.12\text{--}2.09 \times 10^{-7} \text{ mol s}^{-1} \text{ m}^{-2} \text{ Pa}^{-1}$ under 0.2 MPa, and $1.89\text{--}1.67 \times 10^{-7} \text{ mol s}^{-1} \text{ m}^{-2} \text{ Pa}^{-1}$ under 0.3 MPa. The high pressure (0.3 MPa) provides higher hydrogen permeability. However, the hydrogen permeability of TiN-graphene membrane was only dependent on porosity. In addition, comparing the hydrogen permeability of the Pd-Ag amorphous membrane as a reference observed that the TiN-graphene membrane was evaluated to have a higher permeation rate than Pd-Ag amorphous membrane and had the Knudsen diffusion mechanism.

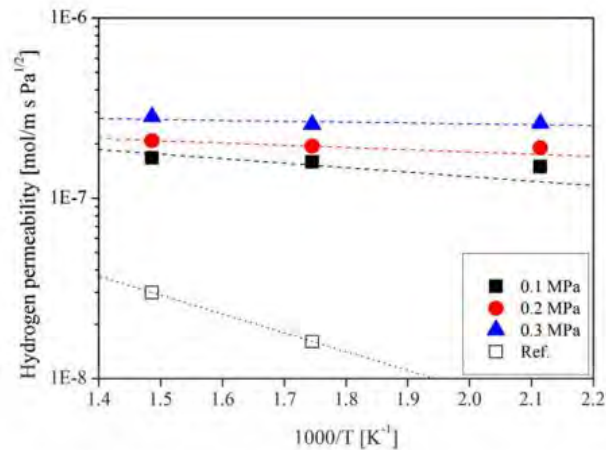


Figure 2.14 Arrhenius plot of the hydrogen permeability as function of inversed temperature [58].

Lee et al. [59] reported the synthesis Al_2O_3 - CeO_2 -Graphene oxide (ACG) composites by sol-gel method. The hot press sintering was used to fabricate ACG composites membrane as the disk type. As shows in Figure 2.15, the hydrogen permeability of ACG at room temperature was $2.62 \times 10^{-7} \text{ mol s}^{-1} \text{ m}^{-2} \text{ Pa}^{-1}$. In addition, the $\text{Al}_2\text{O}_3/\text{CuO}_2/\text{ZnO}_2$ (ACZ) composites with 10wt.% Co and 10wt.% Ni were fabricated. At room temperature, the hydrogen permeability of ACZ-10wt.%Co was $4.9 \times 10^{-8} \text{ mol s}^{-1} \text{ m}^{-2} \text{ Pa}^{-1}$ and that of ACZ-10wt.% Ni was $1.47 \times 10^{-8} \text{ mol s}^{-1} \text{ m}^{-2} \text{ Pa}^{-1}$ as shown in Figure 2.16. The addition of CeO_2 and graphene oxide to ACG had a more favorable effect on hydrogen permeability than the addition of CuO_2 and ZnO_2 .

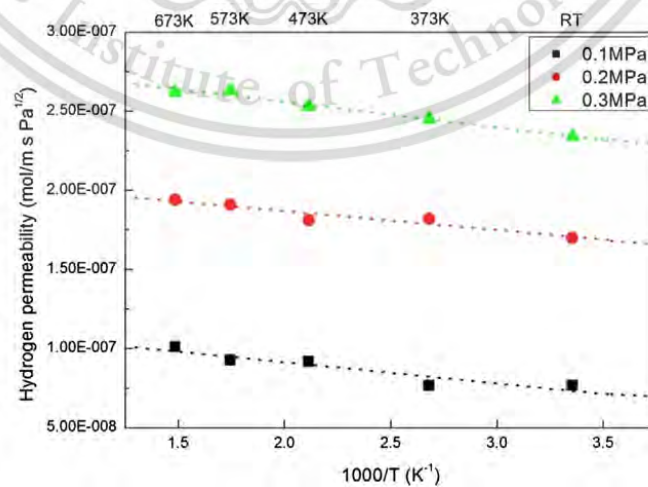


Figure 2.15 Hydrogen permeability of ACG/Al membrane [59].

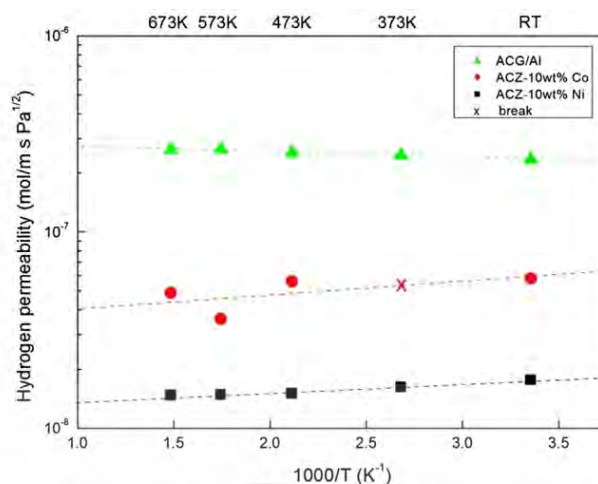


Figure 2.16 Hydrogen permeability of ACG/Al membrane and ACZ-10wt.%Co and ACZ-10wt.% Ni [59].

Based on the literature provided, graphene oxide (GO) membranes have promising potential for hydrogen separation applications. Here are the key takeaways from the different configurations.

Disk Membranes: Offer high selectivity (e.g., $H_2/N_2 = 900$) but limited hydrogen permeance ($10^{-8} \text{ mol s}^{-1} \text{ m}^{-2} \text{ Pa}^{-1}$). **Tubular Membranes:** Permeance increases with temperature and pressure (up to $4.6 \times 10^{-6} \text{ mol s}^{-1} \text{ m}^{-2} \text{ Pa}^{-1}$).

Hollow Fiber Membranes: Show good stability and selectivity ($H_2/N_2 = 28$, $H_2/CO_2 = 323$) with moderate permeance ($8.2 \times 10^{-7} \text{ mol s}^{-1} \text{ m}^{-2} \text{ Pa}^{-1}$). Modified GO layers (e.g., SDBS) can further enhance selectivity.

Composite Membranes: Can achieve higher permeance compared to pure GO membranes (e.g., $2.62 \times 10^{-7} \text{ mol s}^{-1} \text{ m}^{-2} \text{ Pa}^{-1}$ for ACG membrane). The choice of composite materials can significantly impact performance.

Thus, to study the effect of types of carbon materials such as activated carbon, carbon black, graphene oxide, and graphite in fabricating composite membranes using an uncomplex method, which is interested in optimizing these properties for industrial applications.

Chapter 3

Research methodology

In this research, Al₂O₃-carbon composites were fabricated by sintering method with different types of carbon in order to find the possibility to use them as a low-cost membrane for hydrogen separation and adsorbent for removal of hydrogen sulfide.

3.1 Raw materials

The effect of various types of carbon precursors on physical properties, mechanical properties, and gas separation properties of alumina-carbon composites was investigated in this research. The carbon used in this study includes commercial powders of carbon black, activated carbon, graphite, as well as in-house synthesized graphene oxide (GO). The details of the raw material in this research are shown in Table 3.1.

Table 3.1 Fundamentals properties of raw materials

	Raw materials	Company	Purity (%)	Particle size (μm)
Carbon precursors	Carbon black	IRPC	98.9%	0.5
	Activated carbon	C.GIGANTIC Carbon.CO., LTD	95%	45
	Graphite	Sigma-Aldrich	95%	20
	Graphene Oxide	Center of Excellence in Smart Materials Research and Innovation, KMITL	-	-
Alumina	α-Al ₂ O ₃	Nippon Light Metal	99%	~1
Additive	MgO	Fujifilm Wako Chemical	99.9%	0.2

This material is reserved for educational use only, not allowed for commercial use.

Forbidden to modify the content, and cite the document when use.

3.2 Fabrication procedure

The simplified method steps used in the fabrication of alumina-carbon composites are presented in Figure 3.1.

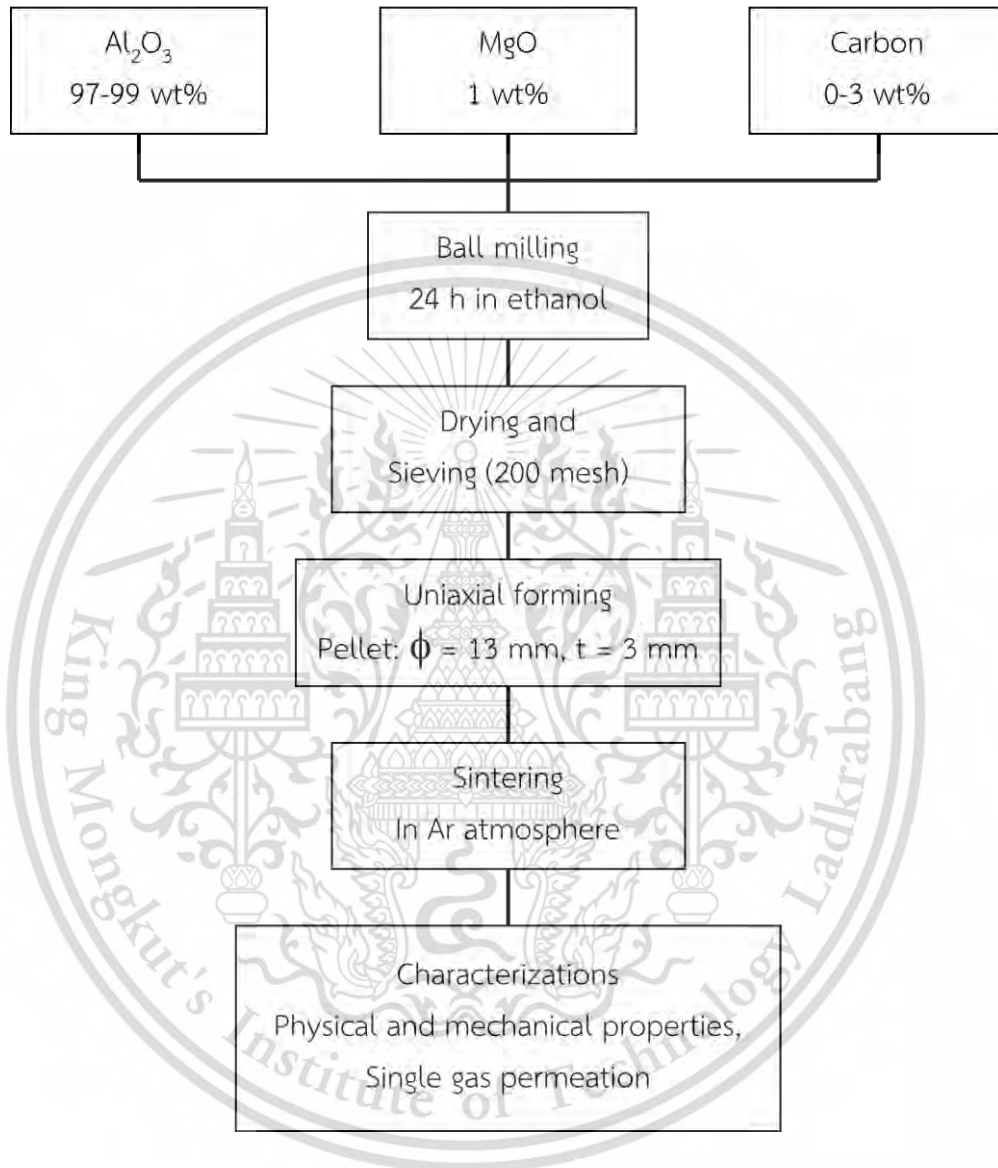


Figure 3.1 Schematic of alumina-carbon composites preparation.

The alumina-carbon composites (with 0.5, 1.0, 1.5, 2.0, 2.5 and 3.0 wt% of carbon) were fabricated via powder metallurgy. Firstly, the green Al₂O₃ powder was mixed with 1% of MgO as an additive material. Following that, the alumina-carbon composite powders were mixed by ball milling using alumina balls (3 mm in diameter) and an ethanol medium in a polypropylene bottle for 24 h at a rotational speed of

300 rpm. Then, the slurry was completely dried in a conventional oven (Memmert Universal Oven, UN55) at 120 °C for 24 h. Subsequently, the mixture powders were sieved through a 200-mesh screen to reduce agglomerates for a uniform powder mixture. Then, the alumina-carbon powders were put into the stainless-steel mold to form a disk-shaped specimen with a diameter of 13 mm and a thickness of approximately 3 mm under uniaxial pressure of 24 MPa. Finally, the specimens were sintered at 1500 °C under an argon atmosphere for 2 h with a heating rate of 5 °C/min.

The influence of carbon addition on the microstructure of the alumina-carbon composites as well as the fundamental physical, mechanical properties and the single gas permeation of hydrogen and nitrogen through the composite membranes were systematically studied and compared to the pure Al₂O₃ as a reference sample.

3.2.1 Membrane sintering

Sintering is the process of densification of the powders compact with the assistance of thermal treatment. Additionally, it is also essential for processing metallurgical powder and ceramics materials. All pellets were placed in an alumina crucible, which is embedded with carbon black powder for alumina-carbon composites pellet and embedded with alumina powder for pure Al₂O₃ as reference materials. The alumina-carbon composites were sintered by the electrical heating element furnace in the tube furnace with a diameter of 7.5 cm and length of 120 cm, as shown in Figure 3.2. The specimen was arranged on the alumina crucible and placed at the center of the tube under and sintered in argon atmosphere with a flow rate of 1 L/min. The parameters of the sintering process in this study are as follows: temperature of 1500 °C, heating rate of 5 °C/min with 2 h soaking before cooling at a rate of 5 °C/min down to at least 100 °C. The sintering temperature profile is displayed in Figure 3.4.



Figure 3.2 Tubular furnace for alumina-carbon composites sintering.

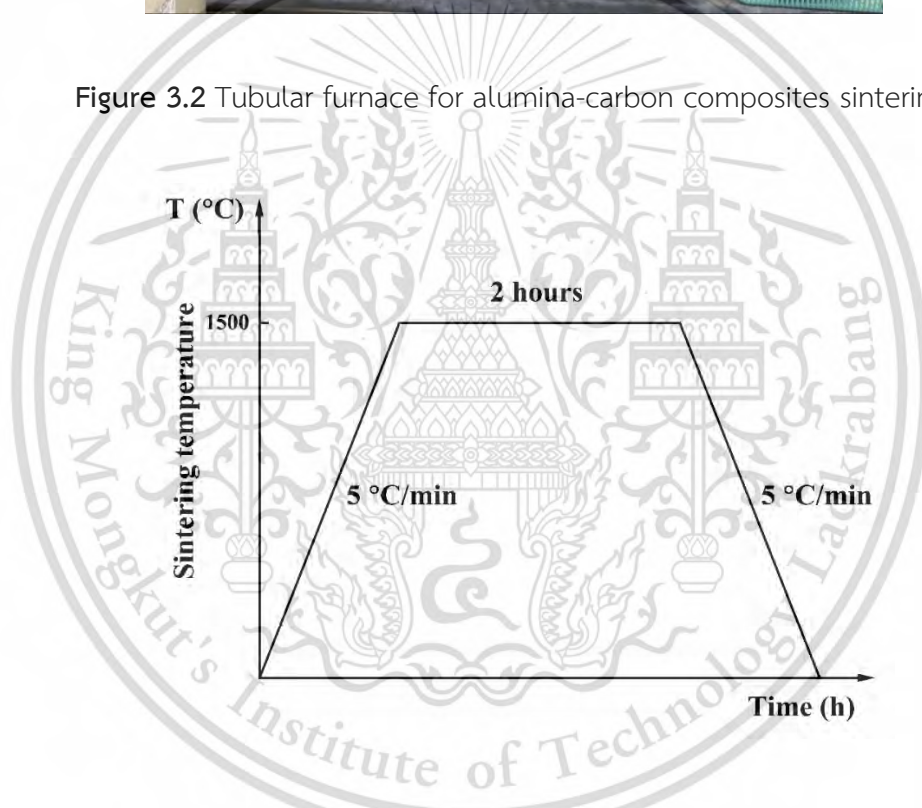


Figure 3.3 Sintering profile of the alumina-carbon composites.

3.3 Composites characterization

3.3.1 Phase Identification

An X-ray diffractometer (XRD; MiniFlex600, Rigaku, Japan) was used to investigate the crystal structure of the composites. The investigation is analyzed by using Cu K α radiation (wavelength $\lambda = 0.15406$ nm). The diffractogram was recorded from 10° to 80° (2θ modes) with a 0.02 step size and step time of 10 s. The X-ray

This material is reserved for educational use only, not allowed for commercial use.

Forbidden to modify the content, and cite the document when use.

tube voltage and current were set at 40 kV and 15 mA, respectively. The phase analysis was carried out using PDXL2 software and comparing the obtained results with Powder Diffraction File (PDF) database.

Additionally, the characterization of both pristine graphene oxide and alumina-carbon (graphene oxide) composites in the sintered specimen was performed using a Raman spectrometer (DXR Smart Raman, Thermo Fisher Scientific, USA) with a 532-nanometer laser excitation wavelength.

3.3.2 Microstructure characterization

Scanning Electron Microscope (SEM) is widely applied to study the morphology of a membrane. In this research, the surface morphology of the membrane was observed by Scanning Electron Microscopy (SEM, FEI, Quanta 250, USA) and field emission scanning electron microscopy (FESEM, Apreo 2, Thermo Fisher Scientific, USA).

The surface microstructure of the specimen was examined using high-resolution Transmission Electron Microscopy (HR-TEM), captured by a JEOL JEM-2100 Plus (field emission gun) transmission electron microscope operating at 200 kV. The microscope was equipped with Energy Dispersive X-ray Spectroscopy (EDX).

3.3.3 Pore size distribution

International Union of Pure and Applied Chemistry (IUPAC) classified the porous material into three categories, which are divided according to the size of the pore as follows; microporous (pore size less than 2 nm), mesoporous (pore size range of 2 to 50 nm) and macroporous (more than 50 nm). The mercury intrusion porosimetry (MicroActive AutoPore V 9600, ATS Scientific Inc, Canada) analysis technique is based on the introduction of mercury into pore space within a porous medium for the purpose of determining its pore size distribution and porosity. For this technique, the specimen was prepared in a square shape of around 1 × 1 cm.

3.3.4 Density measurement

The Archimedes principle was used to measure the density and porosity of sintering specimens according to ASTM C373-88. First, the specimens were dried overnight in an oven at 120 °C then cooled down, and measured the dried weight, D .

This material is reserved for educational use only, not allowed for commercial use.

Forbidden to modify the content, and cite the document when use.

The specimens were put in deionized water and boiled for 6 h and ensure that the deionized water covered the specimens at all times, then leave the specimen 24 h in DI water. Following the impregnation, the suspended weight, S , of each specimen while impregnation in water was determined and shown in Figure 3.2(a). Each specimen was softly wiped to remove all surplus water from the surface with a moistened lint-free linen or cotton cloth, and the saturated weight, M . The Archimedes density measurement setup is shown in Figure 3.5.

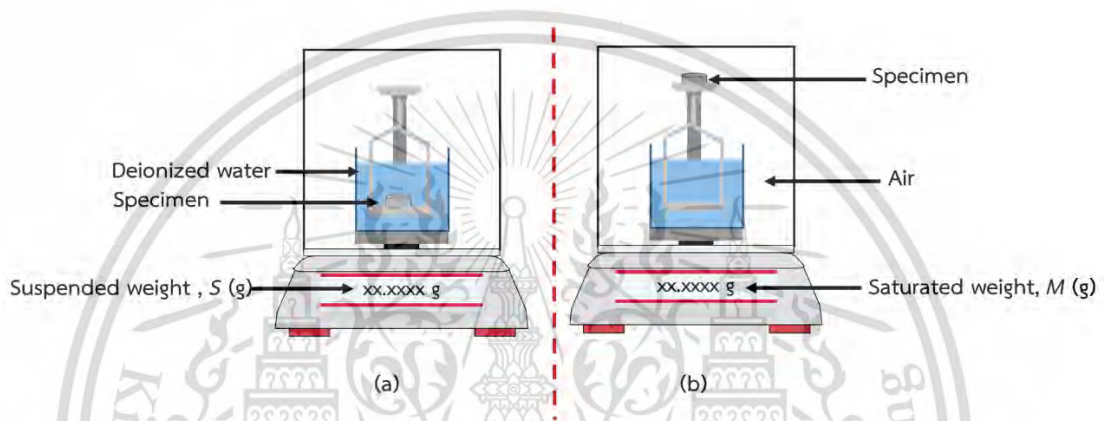


Figure 3.4 Archimedes density measurement setup.

The apparent density (ρ_a) (g/cm^3), of the test specimen can be calculated as follows:

$$\rho_a = \frac{D}{D-S} \quad (3.1)$$

The bulk density (ρ_b) (g/cm^3) of the specimen was calculate as shown in the equation:

$$\rho_b = \frac{D}{M-S} \quad (3.2)$$

The porosity, P (%), expresses, as a percentage, the relationship of the apparent density (ρ_a) and the bulk density (ρ_b) was used to calculate the porosity as the following relation:

$$P = \left(\frac{\rho_a - \rho_b}{\rho_a} \right) \times 100 \quad (3.3)$$

The water absorption, A (%), expresses, as a percentage, the relationship of the weight of water absorbed to the weight of the dry specimen. The water absorption was determined as follows:

This material is reserved for educational use only, not allowed for commercial use.

Forbidden to modify the content, and cite the document when use.

$$A = \left(\frac{M-D}{D} \right) \times 100 \quad (3.4)$$

3.3.5 Hardness

Vickers hardness indentation testers (Zwick Roell, Ulm, Germany) were used to measure the hardness of the sintering specimens. Square-shape indents were produced by applying a 98 N load to pressing the Vickers indenter and holding times for 15 s. The Vickers indenter and surface project diagonal are presented in Figure 3.6. Hardness tests were done at 10 points for each specimen and the average value for each specimen was compared. The diagonal length of each indent, d (mm), was measured using optical microscopy, followed by converted to Vickers hardness, H_V (GPa) using the following equation [60].

$$H_V = 1.854 \times 10^9 \left(\frac{P}{d^2} \right) \quad (3.5)$$

Where P is the indent load.

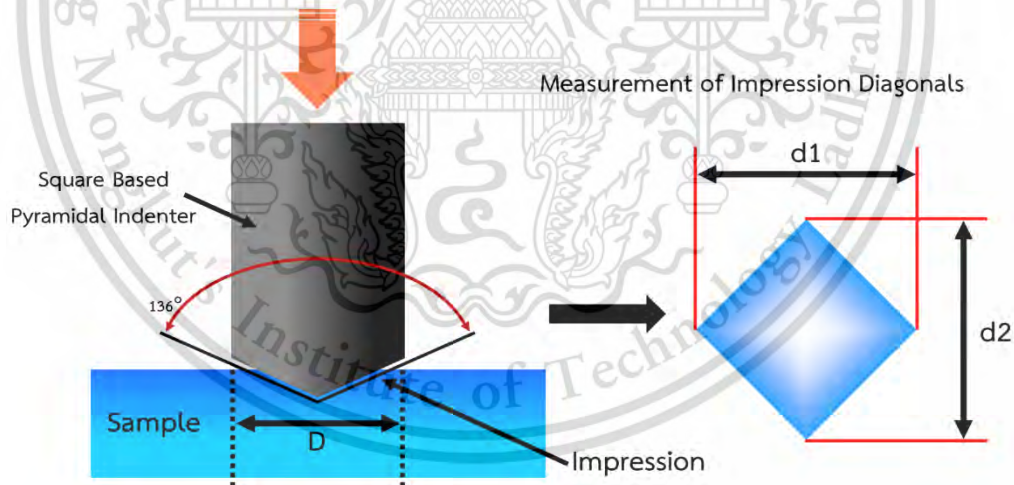


Figure 3.5 Schematic of Vickers hardness measurement.

3.3.6 Gas permeation tests

Gas permeation experiments of alumina-carbon composites membrane performed in a stainless-steel housing. The single gas of nitrogen, N_2 (99.99% purity) with a kinetic diameter of 3.64 Å and hydrogen, H_2 (99.999% purity) with a kinetic

diameter of 2.89 Å was utilized for single-gas permeation tests. The schematic diagram of the experimental setup was presented in Figure 3.7. The single-gas permeation temperature tests were varied in range of 25 to 500 °C, with transmembrane pressures of $\Delta P = 50\text{--}150$ kPa and $\Delta P = 25\text{--}125$ kPa for nitrogen and hydrogen gas, respectively. Single gas permeance values were calculated following equation:

$$J = \left(\frac{DS}{l}\right) e^{-(E_a/RT)} (P_o^{0.5} - P_i^{0.5}) \quad (3.7)$$

where J is the gas permeance through the membrane, in $\text{mol m}^{-2} \text{s}^{-1} \text{Pa}^{-1}$; D is the diffusivity of hydrogen ($\text{m}^2 \text{s}^{-1}$), S is the hydrogen solubility (mol. m^3); l is the thickness of the membrane (m), P_o and P_i are the pressure of outer sides and inner sides of the membrane (P_m).

The ideal selectivity values of H_2/N_2 were calculated by the ratio of permeance values of H_2 to permeance values of N_2 gases.

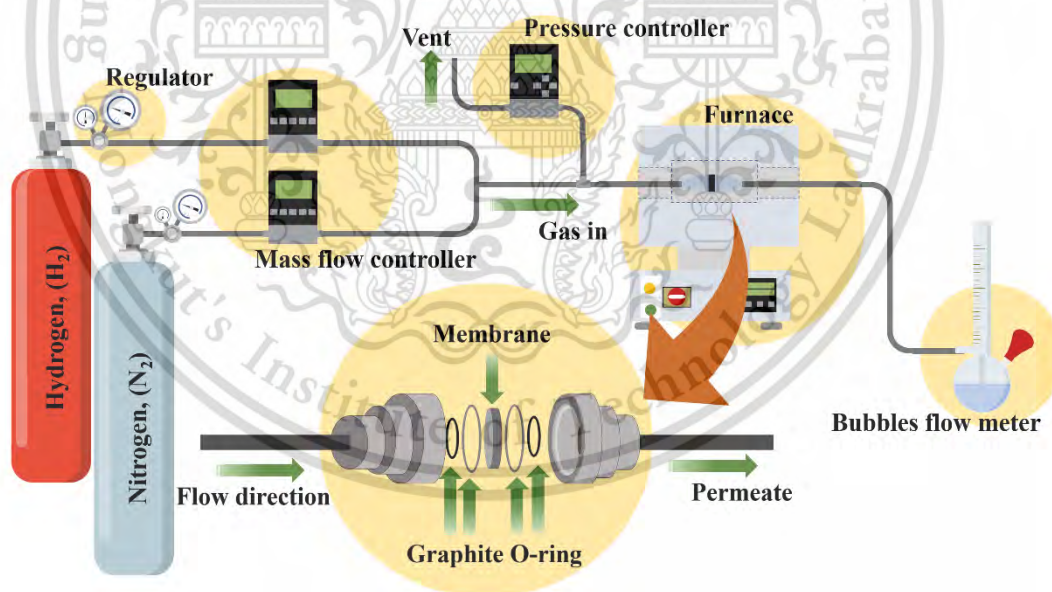


Figure 3.6 Schematic drawing of the hydrogen separation setup.

3.3.7 Hydrogen sulfide adsorption capacity test

The H_2S adsorption experiment was investigated using a fixed housing at room temperature. Figure 3.8 displays the H_2S adsorption experiment setup. The pellet of

alumina-carbon sorbents with a thickness of 3 mm was packed into the housing. After that, H₂S (composition: 1% or 10000 ppm H₂S; balanced with Ar) was released into the reactor with a flow rate of 10 mL/min. The gas analyzer (Geotech; Biogas 5000) was used to detect the H₂S outlet gas from the reactor. In addition, the duration of the experiment was defined as H₂S breakthrough time, and it was also employed to evaluate the H₂S breakthrough capacity of the produced alumina-carbon. The adsorption capacity of the alumina-carbon sorbent was estimated by the following equation:

$$Ads_{cap} = \frac{t_b \cdot FR \cdot C_{in}}{V_{mol} \cdot W} \quad (3.8)$$

where t_b is the breakthrough time (min), FR is the total flow rate (mL/min), C_{in} is the inlet concentration of H₂S, V_{mol} is the molar volume (22.4 mL/mol), and W is the weight of sorbents materials (g).

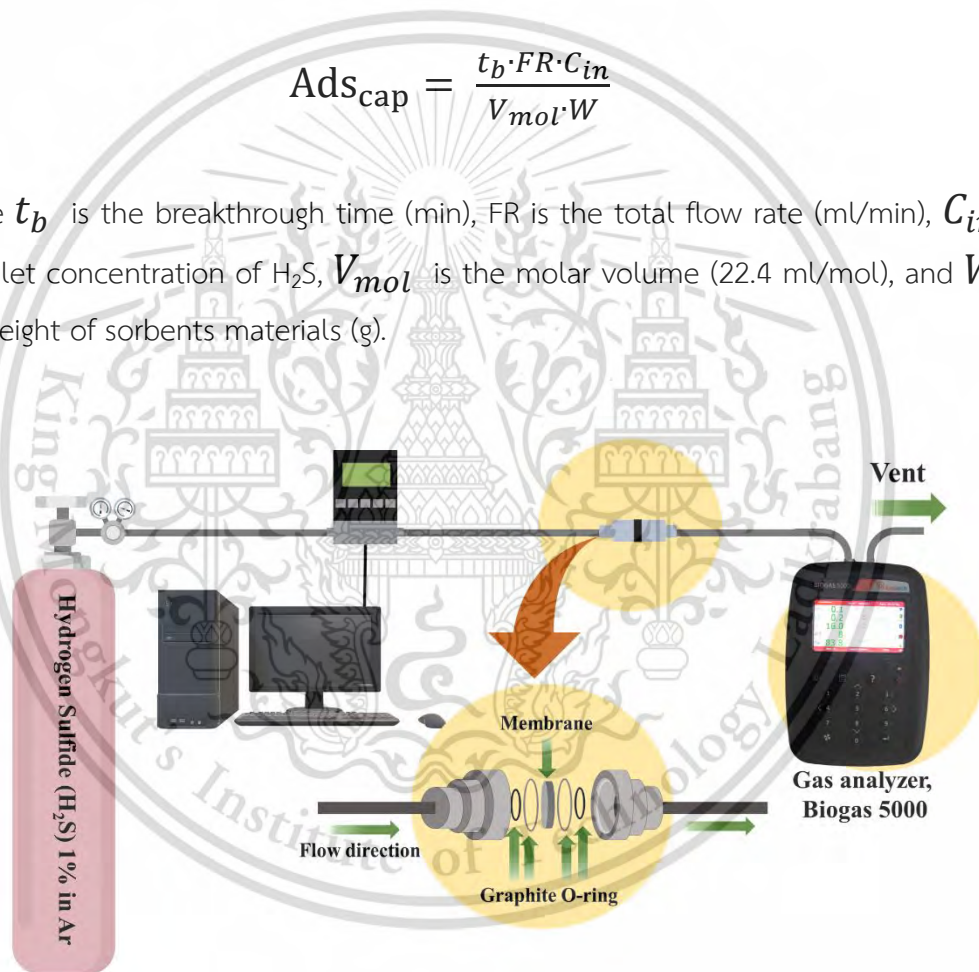


Figure 3.7 Schematic of hydrogen sulfide (H₂S) adsorption experiment setup.

Chapter 4

Result and discussion

This research focuses on the preparation and characterization of Al₂O₃-carbon composite membranes to study their effectiveness in hydrogen (H₂) permeation. Various types of carbon materials, including activated carbon, carbon black (ACB), graphene oxide (AGO), and graphite (AGP), were studied. Each carbon material was utilized at content ranging from 0.5 to 3.0 wt%, with a step of 0.5 wt%. High-temperature sintering was applied to fabricate alumina-carbon composite membranes at a temperature of 1500°C under an argon (Ar) atmosphere for 2 h, with a heating and cooling rate of 5°C/min.

This chapter reports on the influences of carbon addition on the physical characteristics, structure, and mechanical strength of the composite membranes. The single-gas permeation and separation efficiency of the alumina-carbon composite membranes were comprehensively evaluated under varying pressure and temperature conditions and thoroughly discussed.

4.1 Phase identification

Figure 4.1 presents the X-ray diffraction (XRD) patterns, revealing the phase composition of the starting materials. The phases were analyzed based on Bragg's law and 2θ values. Figure 4.1(a) shows the XRD pattern of the α -Al₂O₃ powder, clearly demonstrating its crystalline nature. The sharp peaks appearing at specific 2θ angles confirm its well-ordered crystal structure. The major peaks located at 2θ angles of 25.62°, 35.22°, 37.47°, 43.43°, 52.65°, 57.62°, 61.44°, 66.64°, 68.33°, and 77.06° correspond to specific crystallographic planes of (012), (104), (110), (113), (024), (116), (018), (214), (300), and (1010), respectively. These peak positions perfectly align with the standard data for α -Al₂O₃ (ICDD card 01-073-1123), confirming its hexagonal structure with the *R*-3*c* space group. The sharp and well-defined peaks indicate the presence of large, well-organized crystallites in the sample.

Figure 4.1(b) and 4.1(c) display the XRD patterns of the activated carbon and carbon black, respectively. Both patterns exhibit two primary peaks characteristic of carbon, located at 2θ values near 25.56° and 43.60°. These peaks correspond to reflections from the (002) and (100) planes, respectively. Given the broad nature of these peaks,

This material is reserved for educational use only, not allowed for commercial use.

Forbidden to modify the content, and cite the document when use.

the XRD patterns suggest that both activated carbon and carbon black possess an amorphous structure [61,62].

Figure 4.1(d) shows the characteristic XRD pattern of graphene oxide (GO). The pattern exhibits a peak for the (002) carbon plane in a hexagonal crystal structure for GO nanosheets at 10.83° , corresponding to an interplanar spacing distance (d_{002}) of 0.8 nm. This result is in good agreement with that reported by Lian et al. [63].

Figure 4.1(e) displays the XRD pattern of the graphite specimen. The XRD characteristics of natural flake graphite exhibit peaks at 26.5° , 42.5° , 44.6° , and 54.7° , corresponding to the Miller indices planes of (002), (100), (101), and (004), respectively. The strong (002) peak of graphite is narrower and more intense. Moreover, the interplanar spacing distance (d_{002}) of graphite is 0.34 nm. This result closely matches the findings of Li et al. [64]. Comparing the d_{002} values of graphene oxide and graphite, we observe that the d_{002} of graphene oxide is larger than that of graphite. This is because graphene oxide has oxygen functional groups at the edge of the layers, resulting in a greater spacing between the layers [65].

In addition, the crystalline phase evaluation of Al_2O_3 -carbon composites after sintering was shown in Figure 4.2. It was found that the Al_2O_3 -carbon composites with the kind of carbon of activated carbon (AAC), carbon black (ABC) and graphene oxide (AGO) demonstrated the single phase of Al_2O_3 without any detectable carbon phase. This observation can be attributed to either the limited quantity of carbon present or the overpowering signal from the Al_2O_3 peaks, which it can see at the intensity of starting materials following Figure 4.1. Furthermore, the X-ray diffraction (XRD) analysis of the AGP composite membranes revealed a supplementary peak at 26.6° for AGP1.5. This peak became progressively more evident and discernible at higher graphite concentrations, notably in AGP2.0 and AGP3.0. The emergence of this peak, which corresponds to the (002) planes of the basal plane in crystalline graphite, suggests that the graphite platelets retained their structural integrity and remained undamaged following the sintered-pressing process [66].

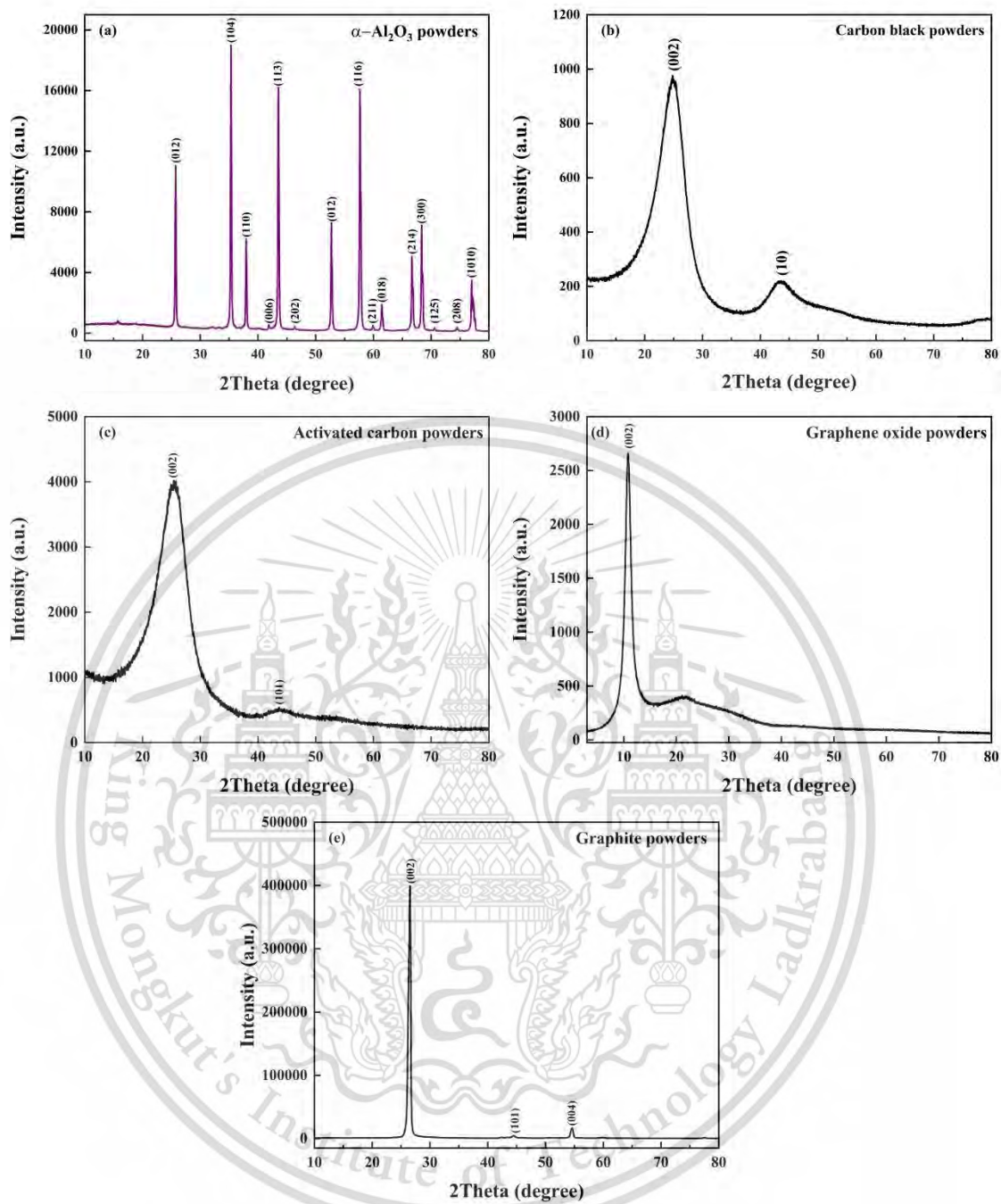


Figure 4.1 XRD patterns of starting materials.

This material is reserved for educational use only, not allowed for commercial use.

Forbidden to modify the content, and cite the document when use.

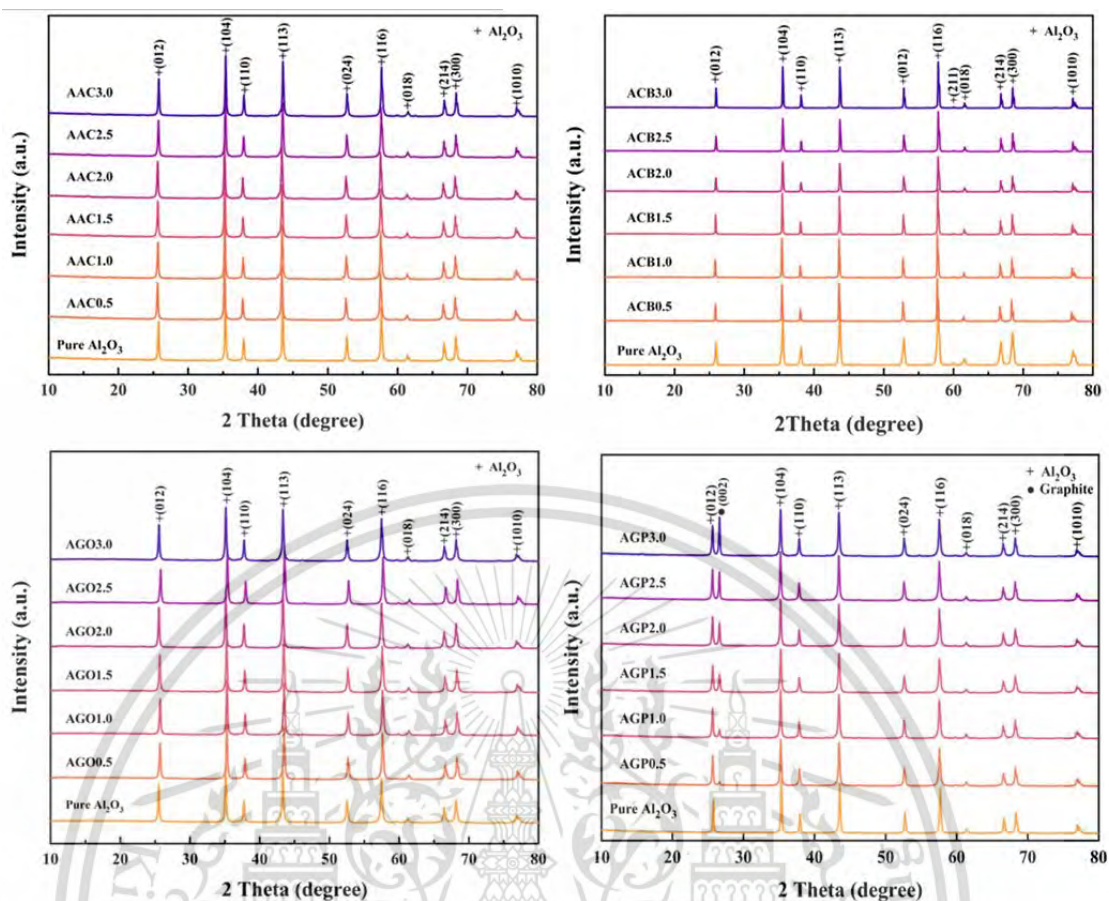


Figure 4.2 XRD patterns of (a) AAC, (b) ACB, (c) AGO and (d) AGP composite membranes with the different carbon addition.

To confirm the presence of carbon-based materials in the post-sintered aluminum-carbon composite membranes, Raman spectroscopy was employed. This technique offers valuable insights into the structural characteristics, specifically through the analysis of the D and G bands and their intensity ratio (I_D/I_G). Raman spectroscopy provides a non-destructive method to analyze the chemical composition and structural characteristics of materials. By focusing on the vibrational modes of carbon molecules, Raman spectra can reveal the presence of various carbon forms, including graphite, graphene, and amorphous carbon.

The two most prominent features in the Raman spectrum of carbon materials are the D and G bands. The D band (around 1350 cm^{-1}) corresponds to the breathing mode of disordered carbon, indicating defects or imperfections in the structure. The G band (around 1580 cm^{-1}) represents the tangential stretching mode of graphitic carbon, This material is reserved for educational use only, not allowed for commercial use.

Forbidden to modify the content, and cite the document when use.

reflecting the degree of in-plane order and sp^2 hybridization [67,68]. The ratio of the intensities of the D and G bands (I_D/I_G) provides valuable information about the structural order and graphitization level of the carbon material. A high I_D/I_G value indicates a high concentration of defects and disorder, while a low value suggests a more ordered and graphitic.

The Raman spectra of AGO composite membranes after sintered were demonstrated in Figure 4.3. The two characteristic bands of G and D band were detected at around 1350 cm^{-1} for D band and 1580 cm^{-1} for G band, which our data corroborates the results of another investigation [69–71]. The outcomes revealed I_D/I_G ratios increase of 0.94, 0.97, 0.99, 1.00, 1.02, and 1.03 for AGO composites with concentrations of 0.5, 1.0, 1.5, 2.0, 2.5, and 3.0, respectively. Several factors can contribute to the increase in the I_D/I_G ratio in materials containing graphene oxide (GO) as the GO content increases [72–74], including:

1. GO inherently contains numerous oxygen-containing functional groups, which introduce defects and disrupt the sp^2 carbon network, contributing to the D band intensity. As GO content in the composite increases, the total number of these defects also increases.
2. High GO content can hinder the complete restoration of the sp^2 carbon network during processing, resulting in smaller graphitic domains and reduced crystallinity.
3. GO sheets can intercalate between layers of other materials, altering their stacking and affecting the local electronic structure.
4. Depending on the type of material and functionalization of GO, specific interactions or bonding can occur between GO and the matrix material. These interactions can affect the vibrational modes and intensities of both the D and G bands.

There are reasons that might result in an elevated I_D/I_G ratio in the AGO composite membrane with increasing graphene oxide content. However, despite the absence of characteristic graphene oxide peaks in the XRD data, the identification of two characteristic peaks in the Raman data confirms the presence of graphene oxide in the alumina-graphene oxide composite membranes.

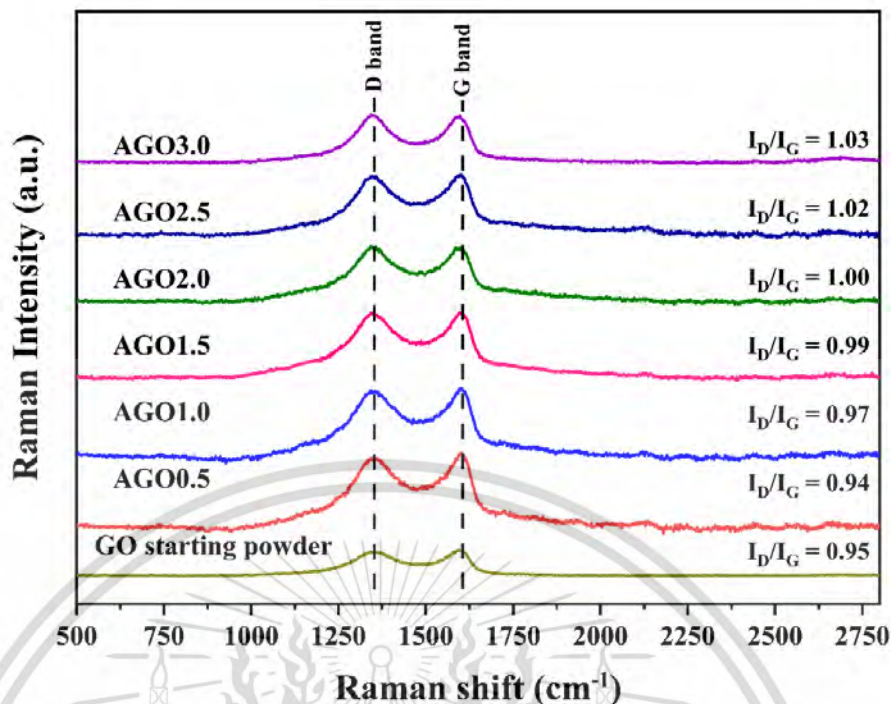


Figure 4.3 The Raman spectra of AGO composite membranes.

In addition, it is concerned that high sintering temperatures might damage the structure of GO in the composites. To assess this, Transmission Electron Microscopy (TEM) was used to examine the structure of sintered GO, specifically focusing on a sample AGO3.0 as shown in Figure 4.4. The images clearly showed GO flakes dispersed between the grains of aluminum oxide (Al_2O_3). Further analysis revealed that the GO within AGO3.0 possessed a layered, sheet-like structure, with a measured d -spacing of 0.334 nm, aligning with the findings of Wang et al. [75]. This suggests that the sintering temperature used in this experiment did not induce the transformation of GO into reduced graphene oxide (rGO). This conclusion is supported by the comparison with research by Ikram et al. [76], who reported a d -spacing of 0.23 nm for rGO, significantly smaller than that observed in AGO3.0 sample.

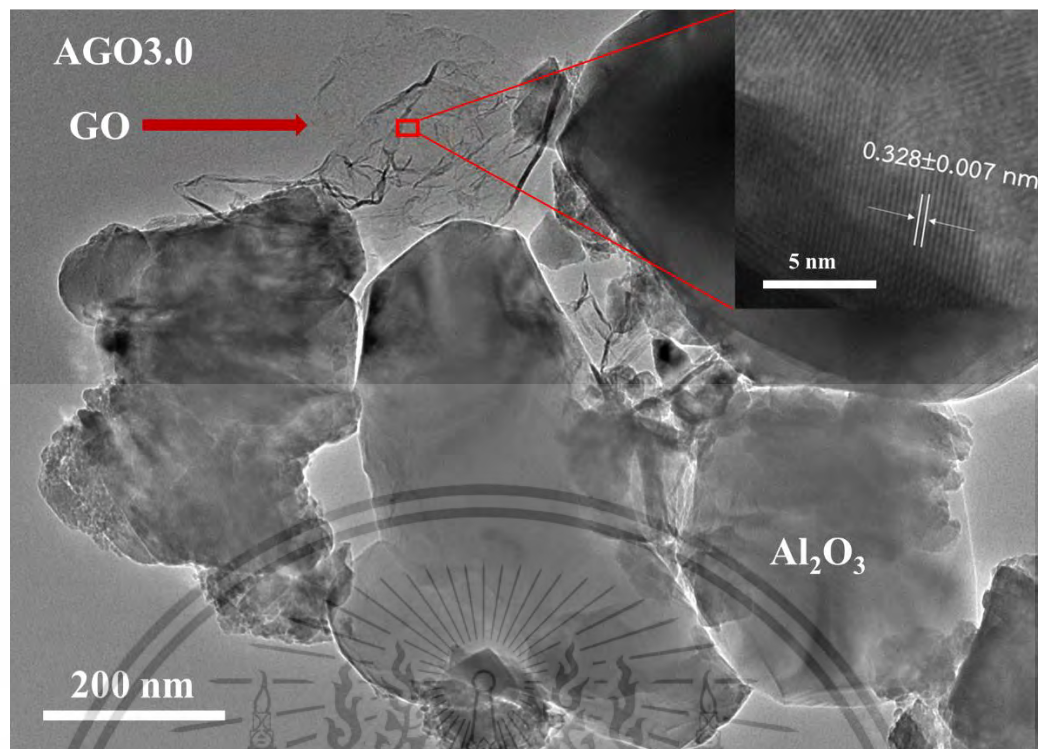


Figure 4.4 TEM image of AGO3.0 composite membranes.

4.2 Physical properties

Figure 4.5 illustrates the effect of carbon content on the bulk density, porosity, and relative density of the Al_2O_3 -carbon composite membrane. The Al_2O_3 specimen without carbon addition demonstrated the lowest bulk density and relative density with 2.29 g/cm^3 and 58%, respectively. Furthermore, it showed the highest porosity of 41.0%.

All types of carbon materials exhibited similar effects on physical properties. Across the four categories, there was a consistent pattern wherein the overall density increased upon the addition of carbon material, reaching its maximum at 0.5 wt% (3.66 g/cm^3 , 3.28 g/cm^3 , 3.65 g/cm^3 , and 3.48 g/cm^3 for AAC, ACB, AGO, and AGP, respectively). Subsequent increments in carbon material content beyond 0.5 wt% led to a decline in bulk density. Among the various carbon additions, the 3.0 wt% carbon content demonstrated the lowest bulk density for AAC, ACB, AGO, and AGP, with values of 3.28 g/cm^3 , 2.84 g/cm^3 , 2.83 g/cm^3 , and 3.01 g/cm^3 , respectively. However, despite the 3.0 wt% specimens exhibiting the lowest bulk density among the carbon addition samples, their bulk density values were still higher than those of the Al_2O_3 specimen.

This material is reserved for educational use only, not allowed for commercial use.

Forbidden to modify the content, and cite the document when use.

The porosity of the specimens presented an inverse trend compared the bulk density; as carbon materials increased, the porosity decreased. The lowest values with 0.5 wt% of carbon addition were 4.00%, 17.9%, 3.7%, and 10.7% for AAC, ACB, AGO, and AGP, respectively. Consequently, further increase in carbon materials by more than 0.5 wt% led to an increase in the porosity of the composite membranes, corresponding to the rise in carbon content. At the maximum addition of carbon materials, at 3.0 wt%, the highest porosity was obtained, with values of 15.2%, 25.6%, 25.8%, and 21.2% for AAC, ACB, AGO, and AGP, respectively. However, comparing the porosity of specimens with the maximum content of carbon addition to that of the Al_2O_3 specimen, it was evident that the porosity of the carbon addition specimens was lower than that of Al_2O_3 .

In addition, the relative density of carbon addition specimens demonstrated a higher value than that of Al_2O_3 specimen (57.6%) and are in the range of 81.6–92.4%, 70.5–77.8%, 73.4%–92.8%, and 76.5–87.8% for AAC, ACB, AGO, and AGP, respectively. The decrease in bulk density with increasing carbon content suggests that adding a small amount of carbon fills the empty spaces (pores) in the composite material, making it more compact. This improved density and reduced porosity enhanced the overall physical properties of the composite. Notably, the amount of gas that can pass through a membrane depends heavily on its porosity, with higher porosity generally leading to easier gas flow. Likewise, the density of membrane also suggest its permeability, as denser materials typically allow less gas to pass through. However, the presence of carbon materials in the membrane adds another layer of complexity to its gas permeation behavior, which will be examined in more detail later.

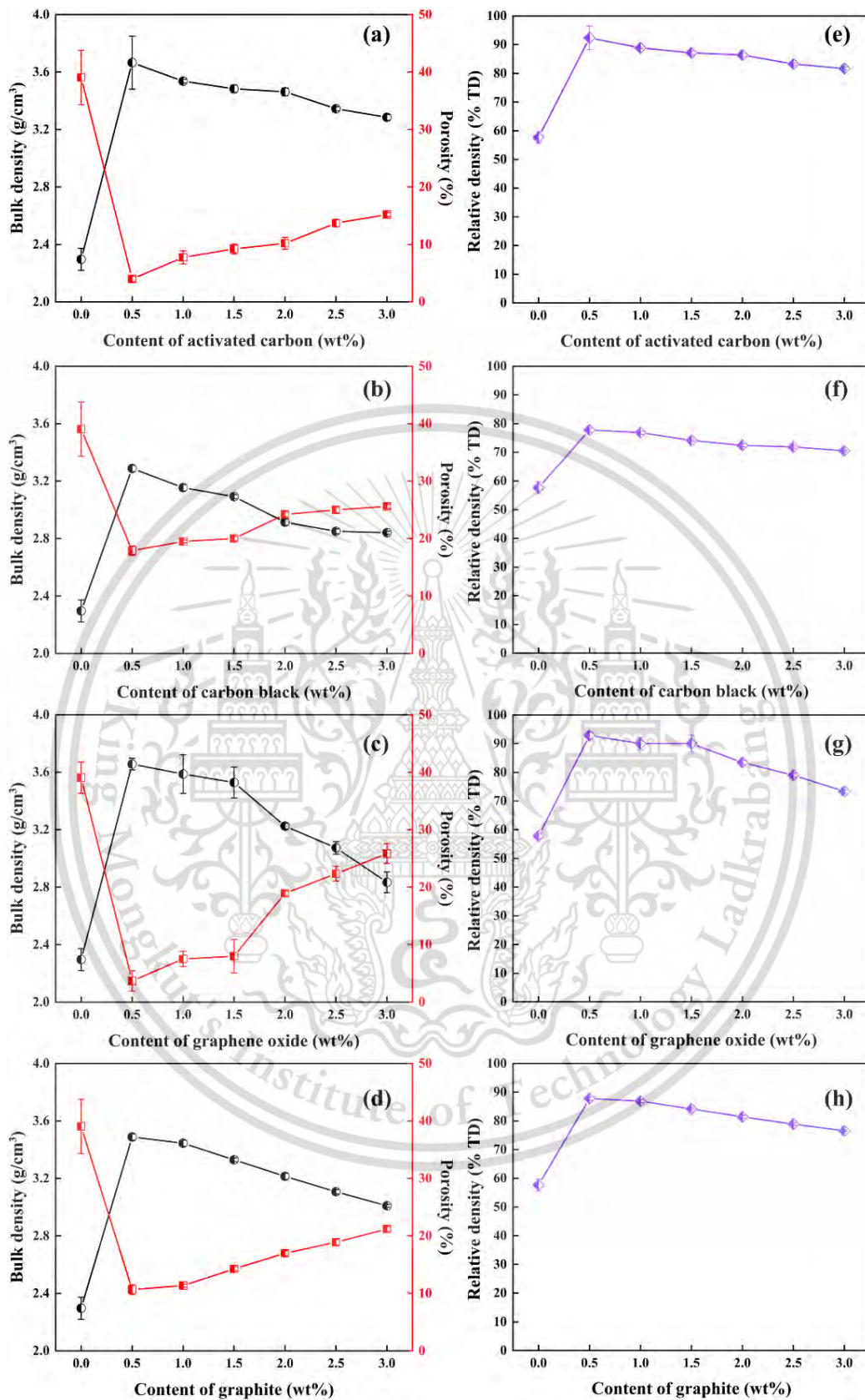


Figure 4.5 The bulk density, porosity, and the relative density as a functions of carbon content for AAC, ACB, AGO and AGP composite membranes.

This material is reserved for educational use only, not allowed for commercial use.

Forbidden to modify the content, and cite the document when use.

4.3 Morphology

The FE-SEM image of the sintered Al_2O_3 specimen is demonstrated in Figure 4.6. The image reveals a nonuniform morphology and a varied particle structure. Some particles appear sharp and angular, while others are smoother and rounder. These particles agglomerate to form partially sintered microstructure with the average grain size of $0.6 \mu\text{m}$ with the average large grain size was $1.12 \mu\text{m}$ and average small grain size was $0.49 \mu\text{m}$. Additionally, small gaps or pores can be seen between the particles.

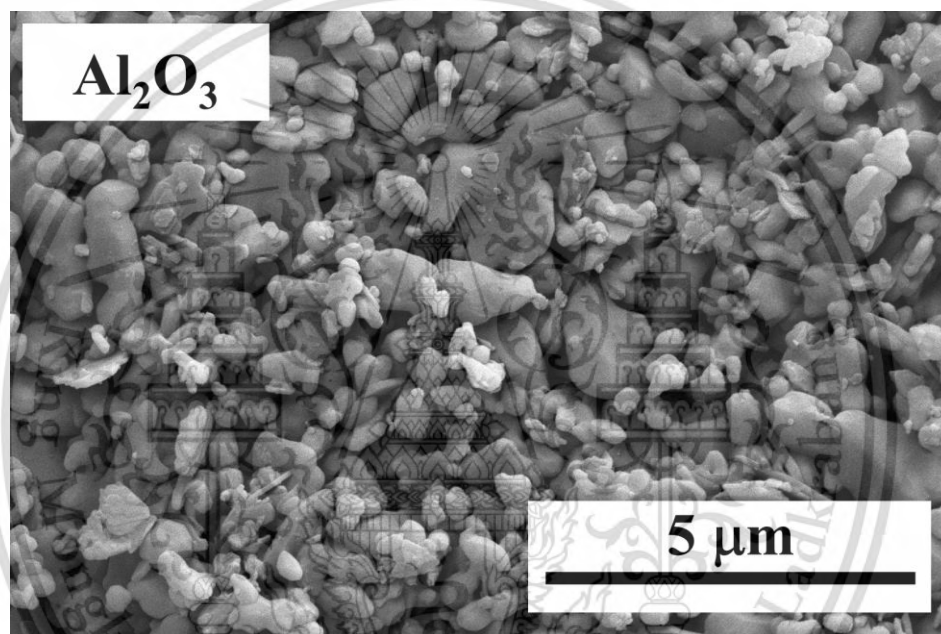


Figure 4.6 FESEM image of Al_2O_3 membrane.

Figure 4.7 illustrates microstructure of Al_2O_3 -activated carbon (AAC) composite membranes containing varying proportions of activated carbon. The AAC composite membranes displayed irregular shapes and exhibit a reduction in grain sizes from $1.16 \mu\text{m}$ to $0.08 \mu\text{m}$ as an activated carbon content increases from 0.5 wt% to 3wt%. Importantly, the grain boundaries within the AAC composite membranes are notably clearer compared to those observed in the Al_2O_3 specimen, indicating effective sintering. Furthermore, it is evident that at lower concentrations of activated carbon, the presence of small gaps or pores is not discernible, resulting in decreased porosity due to pore obstruction and a reduction in surface area.

This material is reserved for educational use only, not allowed for commercial use.

Forbidden to modify the content, and cite the document when use.

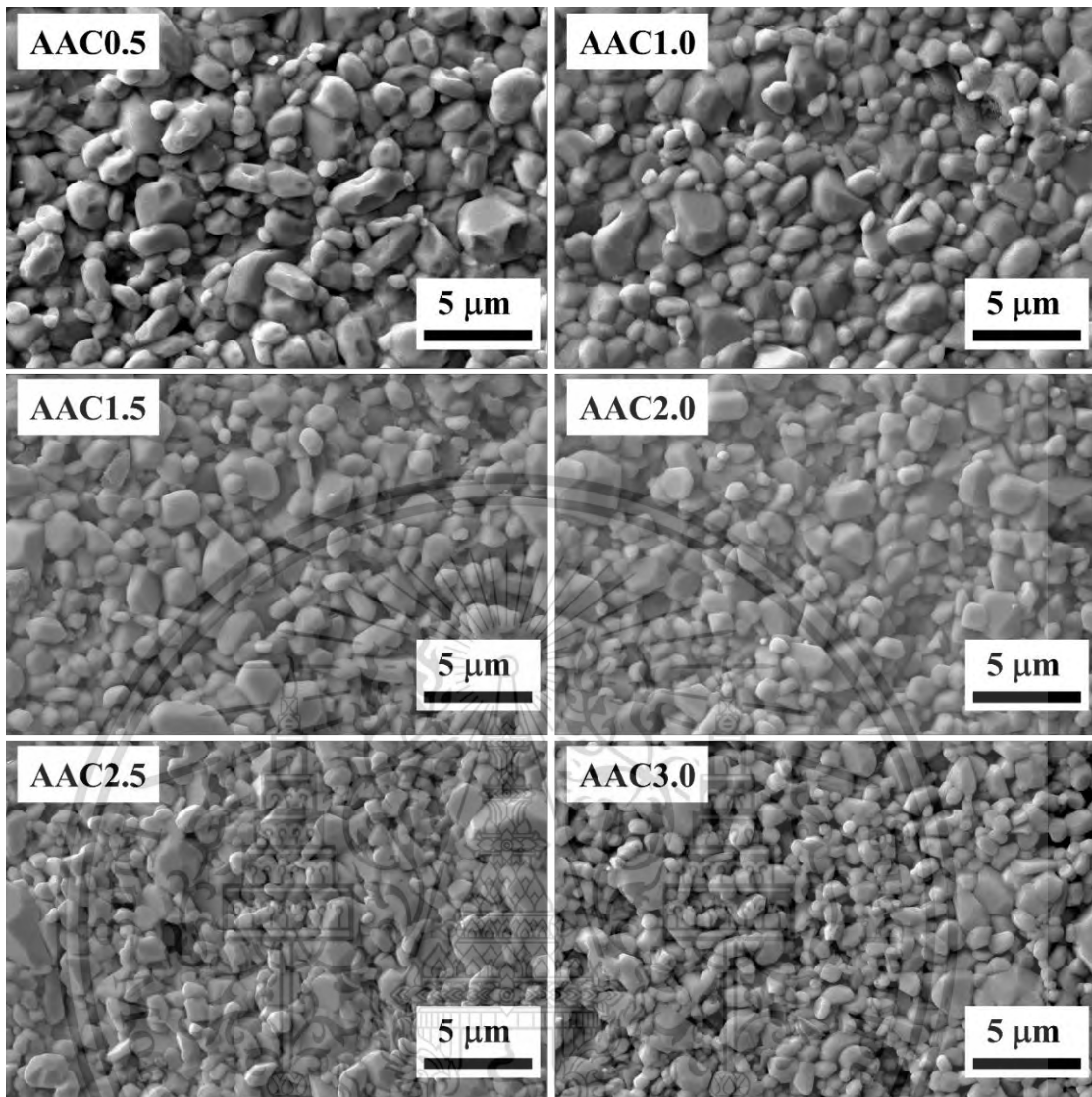


Figure 4.7 Surface morphology of AAC composite membranes with different activated carbon content.

Figure 4.8 illustrates composite membranes of Al_2O_3 -carbon black (ACB) with varying amounts of carbon black. ACB composite membranes display a spherical in grain shape and show grain size ranging from $0.70 \mu\text{m}$ to $1.16 \mu\text{m}$. ACB composite membrane exhibited similar behaviors to the AAC specimen, with clear visibility of the grain boundaries. However, the small gaps or pores between the grain boundaries were also clearly visible. This could be attributed to the smaller particle size of carbon black, which might hinder the close packing of Al_2O_3 particles, resulting in more space between them and the formation of larger pores.

This material is reserved for educational use only, not allowed for commercial use.

Forbidden to modify the content, and cite the document when use.

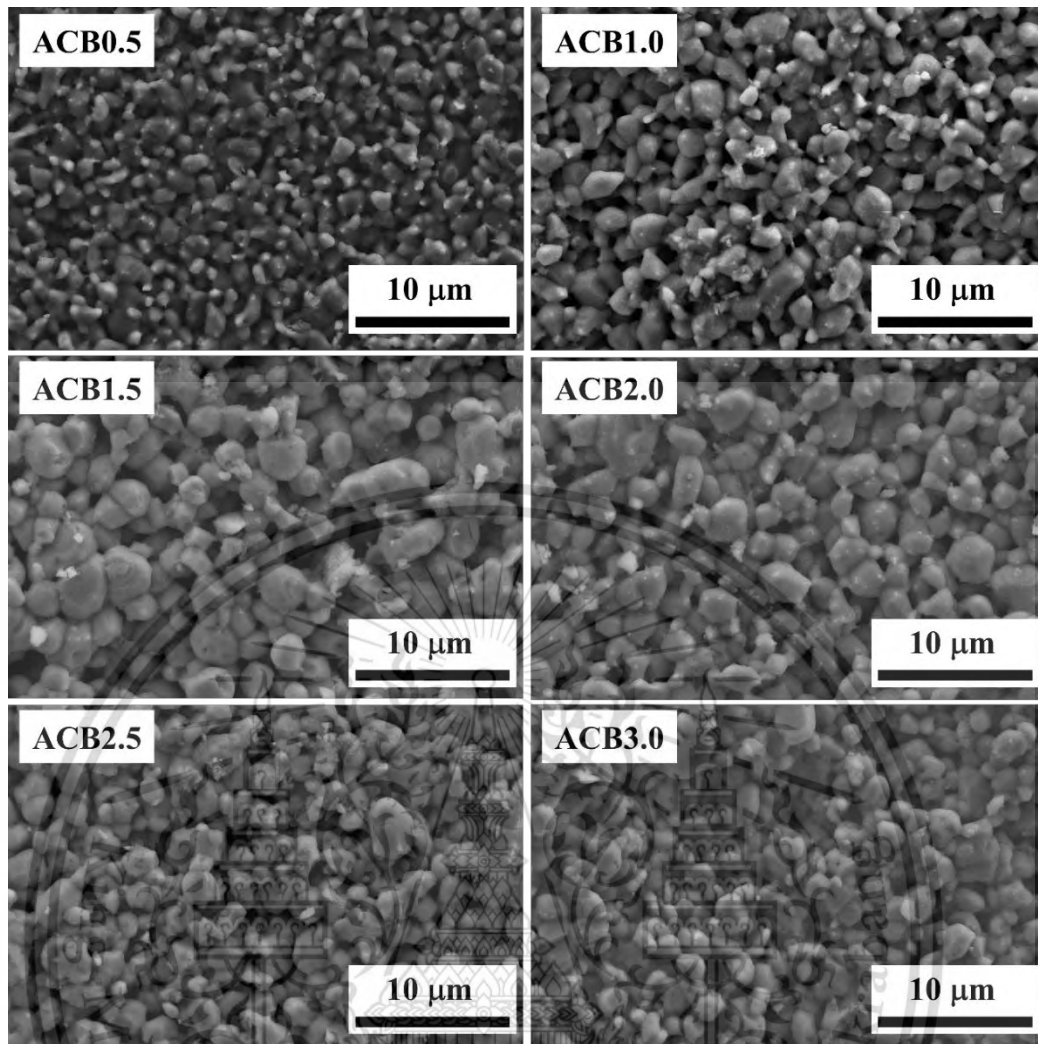


Figure 4.8 Surface morphology of ACB composite membranes with different carbon black content.

Figure 4.9 presents Al_2O_3 -graphene oxide (AGO) composite membranes with different proportions of graphene oxide. These AGO composite membranes demonstrate irregular grain morphology, with grain sizes ranging from $0.80 \mu\text{m}$ to $1.16 \mu\text{m}$. The AGO composite membrane exhibited similar behaviors AAC and ACB specimen, with clear visibility of the grain boundaries.

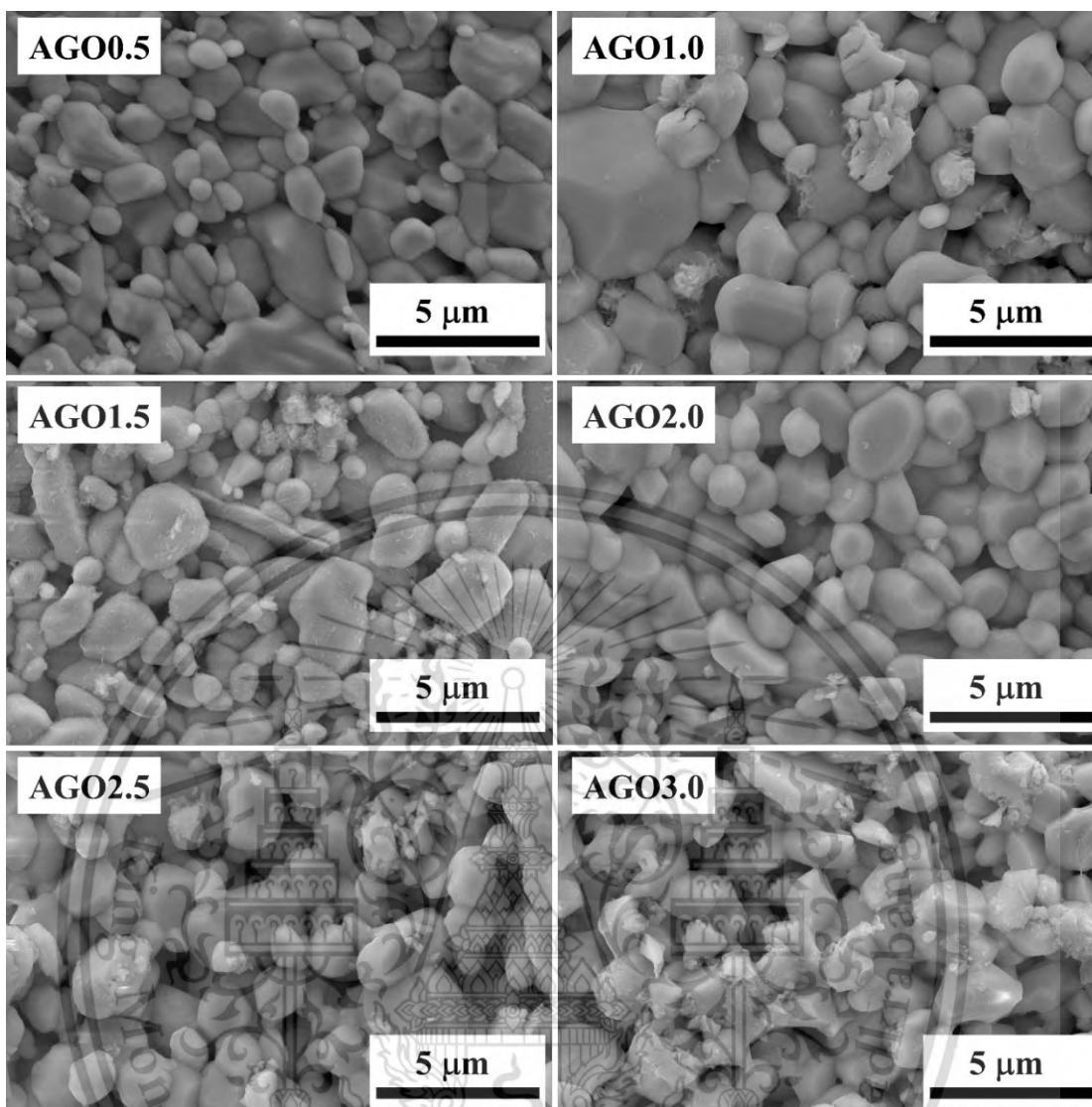


Figure 4.9 Surface morphology of AGO composite membranes with different graphene oxide content.

Figure 4.10 presents Al_2O_3 -graphite (AGP) composite membranes with different proportions of graphene oxide. The AGP composite membranes exhibit irregular morphology, showcasing grains with sizes ranging from $0.80 \mu\text{m}$ to $1.16 \mu\text{m}$. Similar to the behavior reported above, the grain morphology of AGP is irregular. However, compared to alumina, the grain boundaries in AGP are more rounded and sharply defined.

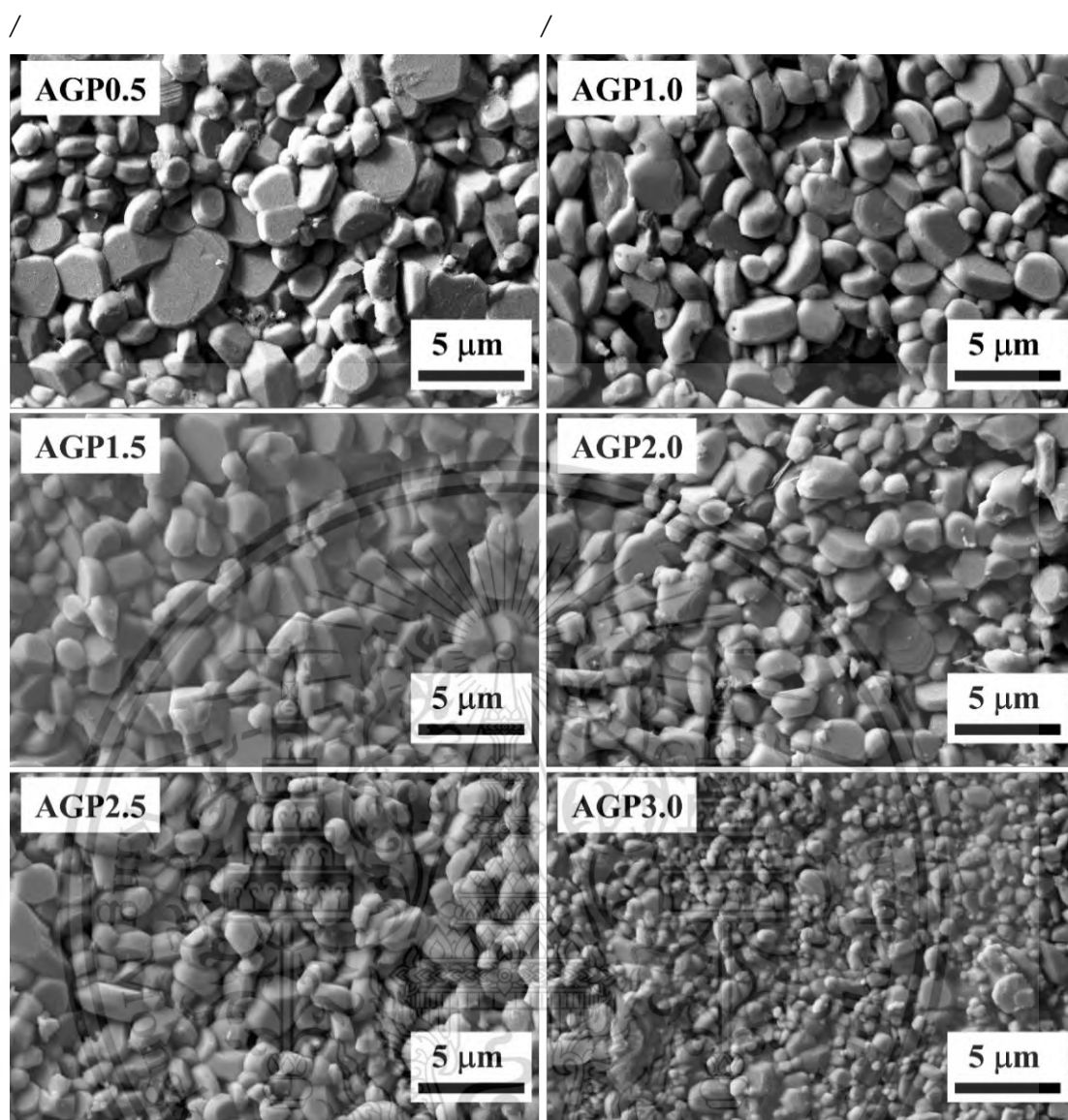


Figure 4.10 Surface morphology of AGP composite membranes with different graphite content.

Furthermore, the estimation of the grain size of Al_2O_3 -carbon composite membranes, employing various types of carbon is illustrated in Figure 4.11. Each Al_2O_3 -carbon composite membrane exhibits a similar pattern, initially showing an increase in grain size up to the maximum value at a different carbon addition volume, specifically, $1.16 \mu\text{m}$ for AAC with 0.5 wt% of activated carbon, $1.06 \mu\text{m}$ for ACB with 1.5 wt% of carbon black, $1.21 \mu\text{m}$ for AGO with 1.0 wt% of graphene oxide, and $1.13 \mu\text{m}$ for AGP specimen with 0.5 wt% of graphene oxide. Continually adding carbon materials, the grain size consistently decreases, reaching values of $0.80 \mu\text{m}$, $0.90 \mu\text{m}$, $1.07 \mu\text{m}$, and

0.81 μm for AAC, ACB, AGO, and AGP, respectively, at a carbon content of 3.0 wt%. It is evident that the addition of carbon materials modifies the grain size of pure Al_2O_3 (0.60 μm).

The observed change in the grain size of Al_2O_3 -carbon composite membranes corresponds to the previously documented densification pattern, suggesting a significant alteration in grain size with the incorporation of carbon. However, once the carbon content exceeds certain thresholds at 1 wt% for AAC and AGP samples, 2.0 wt% for ACB, and 1.5 wt% for AGO - there is a noticeable change in grain size, with the addition of carbon leading to a reduction in grain size. This phenomenon is likely due to the increased aggregation of carbon, which could hinder the growth of grains [77,78].

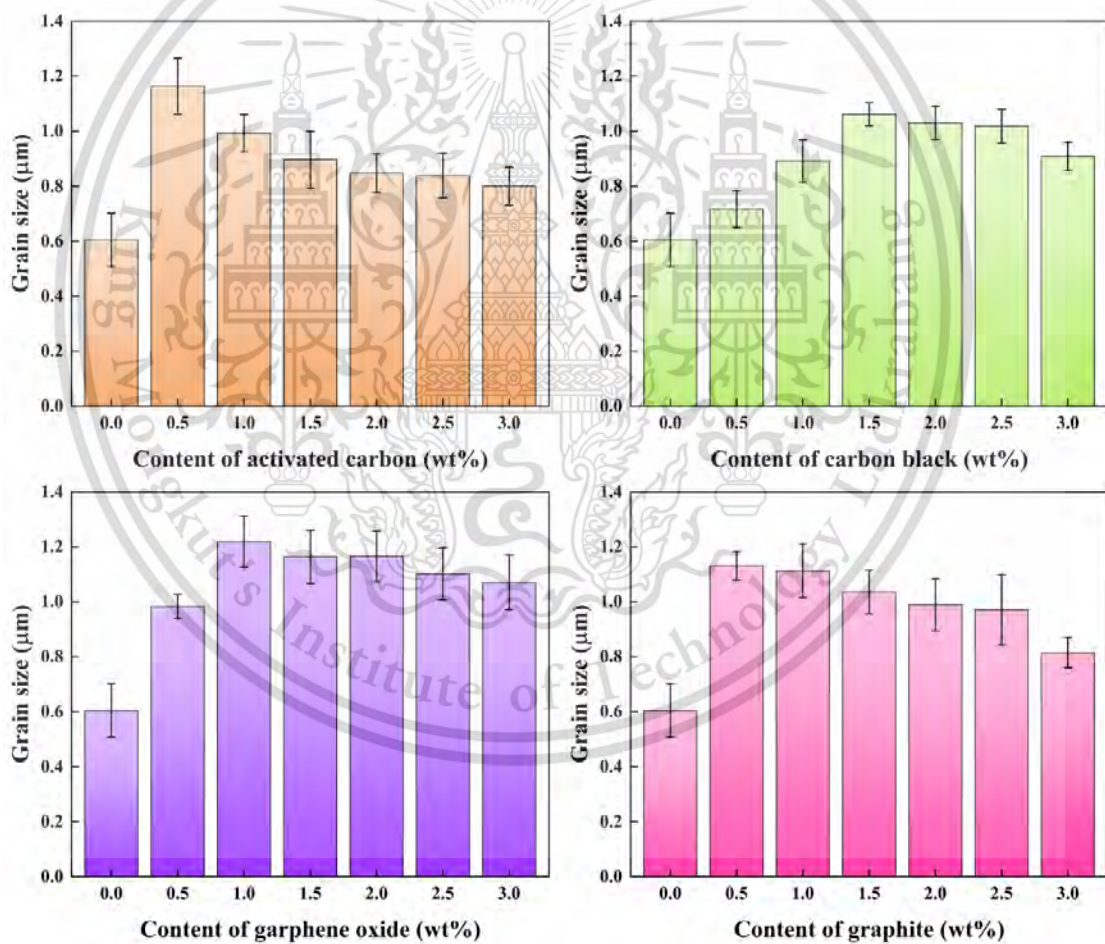


Figure 4.11 Average grain size of AAC, ACB, AGO and AGP composite membranes with different carbon content.

4.4 Pore size distribution

Figure 4.12 quantitatively demonstrates the effect of carbon type and content on the pore size distribution of Al_2O_3 -carbon composite membranes. The log differential intrusion curves represent the pore size distribution obtained from mercury intrusion porosimetry measurements. Pure Al_2O_3 membranes exhibit a pore size range of 48 to 198 nm, with a majority of pores diameter around 150 nm. After incorporating different carbon materials at various concentrations, the following results can be observed.

Figure 4.12(a) depicts the pore size distribution of ACC. It is observed that the most frequent pore size of the AAC specimens increases with higher activated carbon addition amounts, ranging from 60 to 180 nm. Specifically, the details are as follows:

- AAC0.5: The pore size distribution ranges from 65 nm to 232 nm, with the majority pores diameter around 150 nm.
- AAC1.0: The pore size distribution ranges from 32 nm to 131 nm, with the majority pores diameter around 62 nm.
- AAC1.5: The pore size distribution ranges from 48 nm to 167 nm, with the majority pores diameter around 96 nm.
- AAC2.0: The pore size distribution ranges from 59 nm to 195 nm, with the majority pores diameter around 120 nm.
- AAC2.5: The pore size distribution ranges from 61 nm to 237 nm, with the majority pores diameter around 150 nm.
- AAC3.0: The pore size distribution ranges from 63 nm to 238 nm, with the majority pores diameter around 182 nm.

Figure 4.12(b) depicts the pore size distribution of ACB. It is observed that the most frequent pore size of the ACB specimens increases with higher carbon black addition amounts, ranging from 22 to 460 nm. Specifically, the details are as follows:

- ACB0.5: Pore sizes vary within the 50 nm to 460 nm range, with the majority pores diameter around 285 nm.

- ACB1.0: Pore sizes vary within the 52 nm to 445 nm range, with the majority pores diameter around 353 nm.
- ACB1.5: Pore sizes vary within the 50 nm to 445 nm range, with the majority pores diameter around 354 nm.
- ACB2.0: Pore sizes vary within the 39 nm to 441 nm range, with the majority pores diameter around 353 nm.
- ACB2.5: Pore sizes vary within the 22 nm - 353 nm range, with the majority pores diameter around 226 nm.
- ACB3.0: Pore sizes vary within the 22 nm to 350 nm range, with the majority pores diameter around 224 nm.

Figure 4.12(c) shows a different pore size distribution for AGO, adding graphene oxide increases the most common pore size in the AGO samples. This effect is seen across various amounts of added carbon, with the pore size ranging from 29 to 352 nm. Below are the details for each sample:

- AGO0.5: Pore sizes vary within the 29 nm to 119 nm range, with the majority pores diameter around 74 nm.
- AGO1.0: Pore sizes vary within the 43 nm to 125 nm range, with the majority pores diameter around 82 nm.
- AGO1.5: Pore sizes vary within the 73 nm to 274 nm range, with the majority pores diameter around 168 nm.
- AGO2.0: Pore sizes vary within the 77 nm to 352 nm range, with the majority pores diameter around 223 nm.
- AGO2.5: Pore sizes vary within the 70 nm to 300 nm range, with the majority pores diameter around 183 nm.
- AGO3.0: Pore sizes vary within the 62 nm to 307 nm range, with the majority pores diameter around 185 nm.

Finally, the pore size distribution of AGP shown in Figure 4.12(e). The pore size of the AGP specimens increases with the increase in the graphite addition amount, ranging from 41 to 226 nm. the details are as follows:

- AAC0.5: The pore size distribution ranges from 41 nm to 148 nm, with the majority pores diameter around 76 nm.

This material is reserved for educational use only, not allowed for commercial use.

Forbidden to modify the content, and cite the document when use.

- AAC1.0: The pore size distribution ranges from 42 nm to 188 nm, with the majority pores diameter around 78 nm.
- AAC1.5: The pore size distribution ranges from 49 nm to 179 nm, with the majority pores diameter around 85 nm.
- AAC2.0: The pore size distribution ranges from 52 nm to 175 nm, with the majority pores diameter around 95 nm.
- AAC2.0: The pore size distribution ranges from 50 nm to 187 nm, with the majority pores diameter around 121 nm.
- AAC3.0: The pore size distribution ranges from 51 nm to 226 nm, with the majority pores diameter around 178 nm.

The International Union of Pure and Applied Chemistry (IUPAC) [79] categorizes nanoporous materials based on their pore size. Microporous: Tiny pores between 0.2 and 2 nanometers. Mesoporous: Intermediate pores ranging from 2 to 50 nanometers. Macroporous: Larger pores spanning 50 to 1000 nanometers. Following the Al₂O₃–carbon composite membranes based on the above analysis can be classified based on their pore size as macroporous materials.

However, the influence of macroporous size was a critical factor in gas permeance, and the selectivity of gas molecules, which will be discussed in the gas permeance section. The pore size of a carbon membrane plays a crucial role in its gas permeation and separation properties, and macroporous size (50–1000 nm) holds significant potential for hydrogen applications.

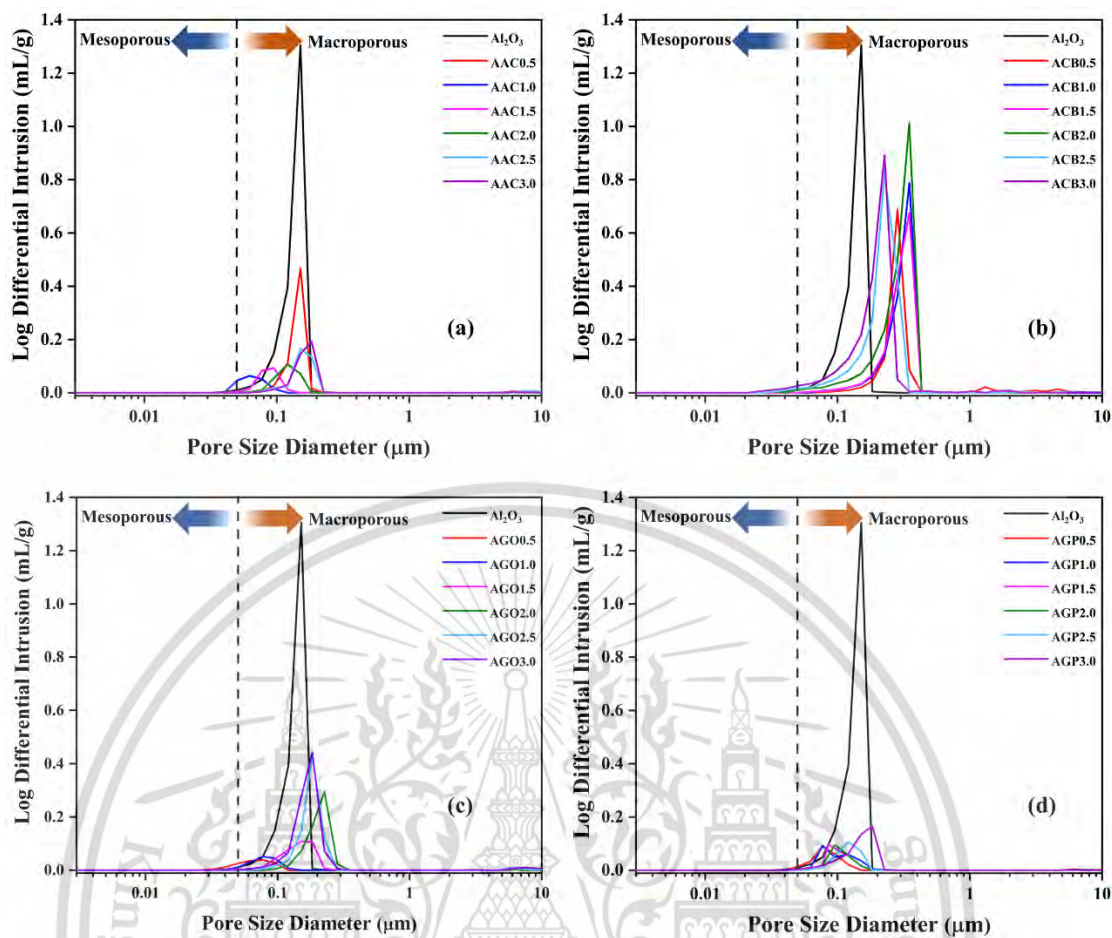


Figure 4.12 Pore size distributions of (a) AAC, (b) ACB, (c) AGO and (d) AGP composite membranes as a function of carbon content.

4.5 Mechanical Properties

This study utilized the Vickers test to evaluate the hardness of Al_2O_3 –carbon composite membranes. Visual analysis of the optical microscopy images of Vickers indentations (depicted in Figure 4.13) reveals the occurrence of corner cracks. Importantly, the absence of significant lateral cracking or spalling in the vicinity of the indentations, coupled with the minimal presence of multiple cracks around them,

Figure 4.14 presents the Vickers hardness values for the Al_2O_3 –carbon composite membranes. Notably, the Vickers hardness of the Al_2O_3 specimen was determined to be 1.82 ± 0.07 GPa. In addition, each specimen of addition of carbon with different type presented the similar behavior. It was found that when carbon was added at concentrations of 0.5 wt% of carbon materials results in the hardness of each type of carbon were highest with the 7.80 ± 0.28 GPa, 8.78 ± 0.58 GPa, 11.92 ± 0.51 GPa.

GPa and 10.18 ± 1.47 GPa for AAC, ACB, AGO and AGP, respectively. The addition of graphene oxide at 0.5 wt% demonstrated the highest hardness compared with other carbon type.

Consequently, the addition of carbon materials led to a decrease in the hardness of the composite membrane, reaching its lowest value at 3 wt% of carbon, with measurements of 3.57 ± 0.29 GPa, 3.15 ± 0.17 GPa, 4.42 ± 0.59 GPa, and 4.46 ± 0.45 GPa for AAC, ACB, AGO, and AGP specimens, respectively. The reduction in hardness, associated with the increased presence of carbon, is ascribed to the non-uniform distribution of carbon. The clustering of carbon at high content results in the formation of a network with a diminished reinforcing effect. Additionally, in accordance with SEM data, carbon particles tend to aggregate, forming clusters or agglomerates. These agglomerates serve as weak points within the composite, failing to contribute effectively to reinforcement. The incorporation of carbon during processing can also impact the alumina grain size. Our findings regarding the reduction in hardness with increasing carbon content corroborate those of earlier studies [80–82]

However, it can be observed that at the highest carbon addition (3.0 wt%), the hardness values of the samples are still higher than those of pure Al_2O_3 specimen. While membrane hardness may not directly influence hydrogen permeability, it remains a crucial parameter for high-pressure gas separation systems due to durability requirements. This study confirms that all synthesized Al_2O_3 –carbon composite membranes possess sufficient hardness for practical applications. Their secure installation in the permeation cell and lack of damage during testing further validate their suitability.

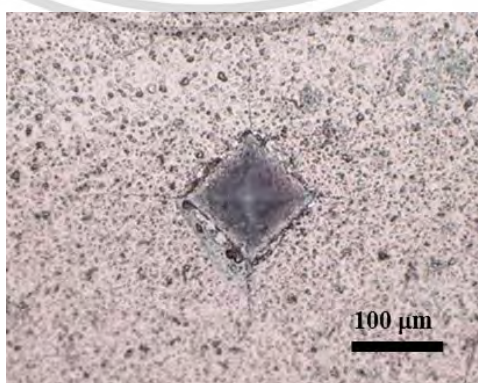


Figure 4.13 Vicker's Indentation of AGP composite membrane.

This material is reserved for educational use only, not allowed for commercial use.

Forbidden to modify the content, and cite the document when use.

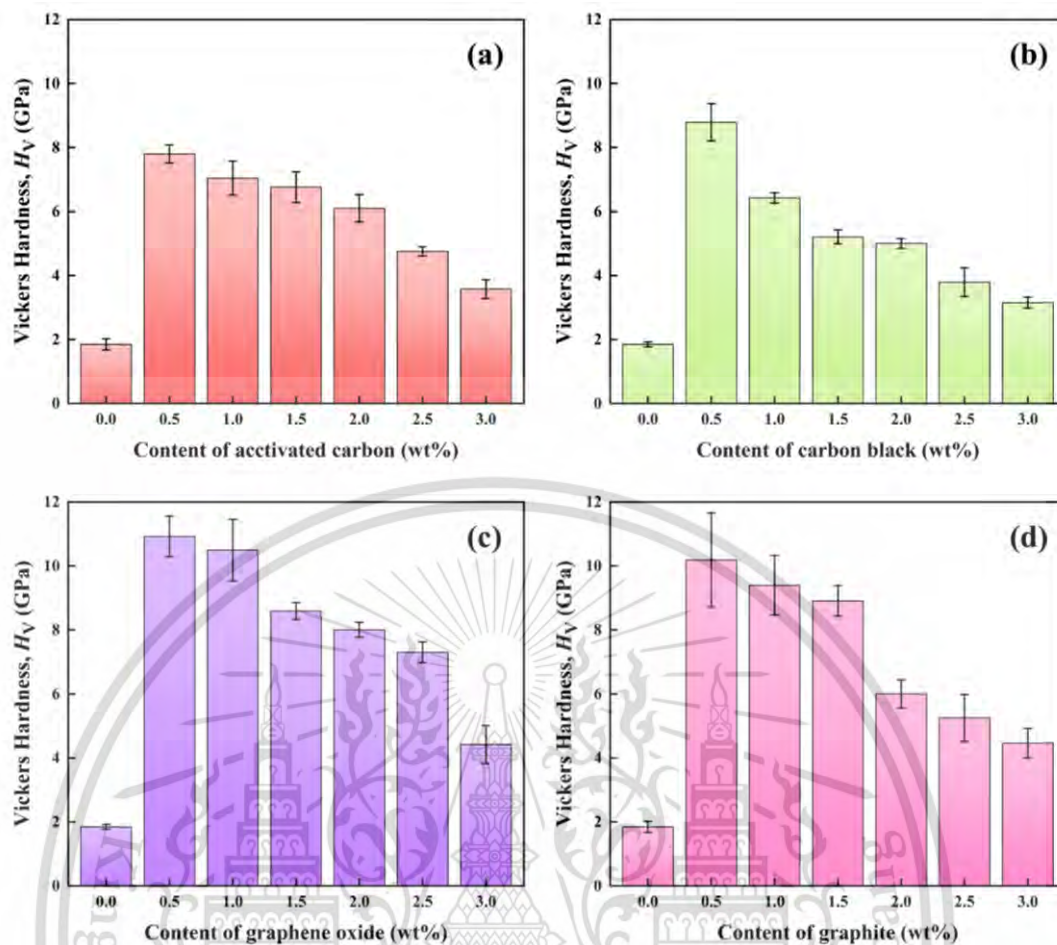


Figure 4.14 Vickers hardness of (a) AAC, (b) ACB, (c) AGO, and (d) AGP composite membrane with different carbon content contents.

4.6 Gas permeance performance

The gas permeance performance of Al_2O_3 —carbon composites membrane was systemically investigated by single gas permeation method. Figure 4.15 illustrates the gas permeance performance of the Al_2O_3 specimen as a function of temperature. The results indicate that at room temperature, the permeance values for H_2 and N_2 were determined to be 134×10^{-6} and $63 \times 10^{-6} \text{ mol m}^{-2} \text{ s}^{-1} \text{ Pa}^{-1}$, respectively. As the temperature of permeation increased, there was a decrease observed in the gas permeance for both H_2 and N_2 . Notably, at 500 °C, the lowest gas permeation was recorded, with values of 76×10^{-6} and $30 \times 10^{-6} \text{ mol m}^{-2} \text{ s}^{-1} \text{ Pa}^{-1}$ for H_2 and N_2 , respectively. Consequently, there is a slight enhancement in H_2/N_2 selectivity, rising from 2.13 to 2.53 within the temperature range of 25 to 500 °C. The decline in both

H₂ and N₂ permeance as temperature increases exhibits a similar pattern through porous Al₂O₃ membrane. As the permeation temperature increased, the activation energy required for gas molecule transport through the membrane exhibited a reduction in negativity, concurrently with a diminished adsorptive affinity of the membrane towards the gas molecules. This combined effect led to a decline in the overall permeance, i.e., the quantity of gas molecules successfully traversing the membrane per unit time and pressure.

To evaluate the gas permeation characteristics of Al₂O₃-carbon composite membranes using four types of carbon: activated carbon (AAC), carbon black (ACB), graphene oxide (AGO), and graphite (AGP), were examined.

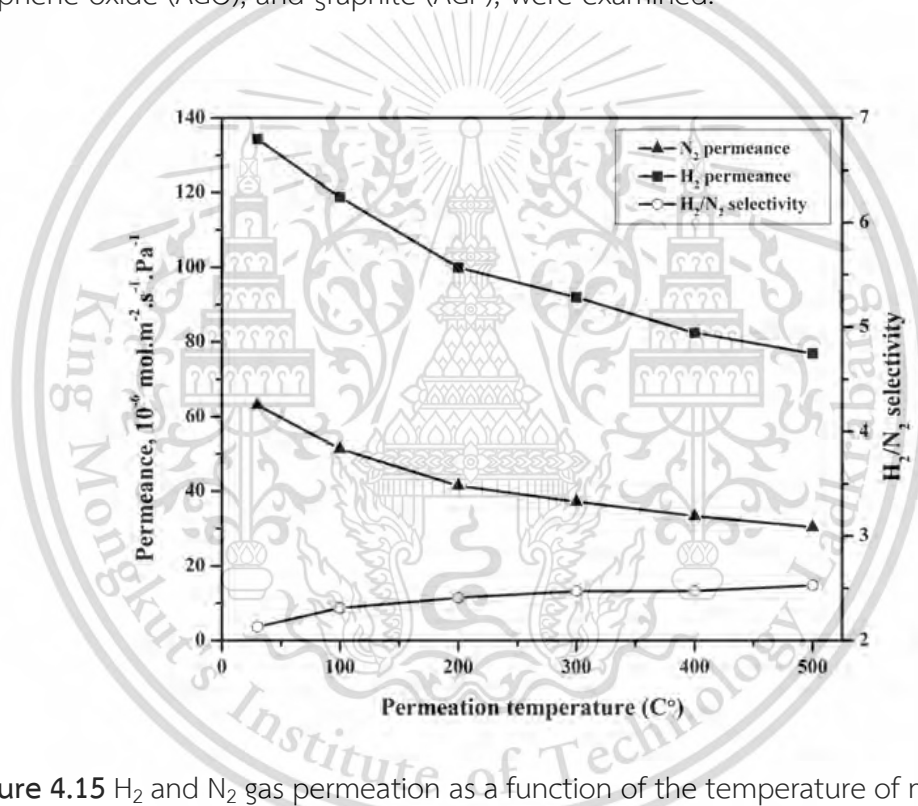


Figure 4.15 H₂ and N₂ gas permeation as a function of the temperature of mesoporous Al₂O₃ membranes.

Figure 4.16 depicted the gas permeance performance of AAC composite membranes. This result indicates that the permeance behaviors of AAC composite membranes show similarity to that of the Al₂O₃ specimen, generally decreasing with increasing transmembrane temperature for all studied gases. Although the different gases permeate at different rates and react differently to changes in activated carbon, the overall behavior suggests they all get through a similar mechanism. At 30 °C, the

H₂ gas permeance values for AAC were determined as follows: $56 \times 10^{-6} \text{ mol m}^{-2} \text{ s}^{-1} \text{ Pa}^{-1}$ for AAC0.5, $99 \times 10^{-6} \text{ mol m}^{-2} \text{ s}^{-1} \text{ Pa}^{-1}$ for AAC1.0, $124 \times 10^{-6} \text{ mol m}^{-2} \text{ s}^{-1} \text{ Pa}^{-1}$ for AAC1.5, $166 \times 10^{-6} \text{ mol m}^{-2} \text{ s}^{-1} \text{ Pa}^{-1}$ for AAC2.0, $236 \times 10^{-6} \text{ mol m}^{-2} \text{ s}^{-1} \text{ Pa}^{-1}$ for AAC2.5, and $275 \times 10^{-6} \text{ mol m}^{-2} \text{ s}^{-1} \text{ Pa}^{-1}$ for AAC3.0. As the experimental temperature increased, the H₂ gas permeance of AAC composite membranes decreased to $37 \times 10^{-6} \text{ mol m}^{-2} \text{ s}^{-1} \text{ Pa}^{-1}$ for AAC0.5, $90 \times 10^{-6} \text{ mol m}^{-2} \text{ s}^{-1} \text{ Pa}^{-1}$ for AAC1.0, $100 \times 10^{-6} \text{ mol m}^{-2} \text{ s}^{-1} \text{ Pa}^{-1}$ for AAC1.5, $133 \times 10^{-6} \text{ mol m}^{-2} \text{ s}^{-1} \text{ Pa}^{-1}$ for AAC2.0, $197 \times 10^{-6} \text{ mol m}^{-2} \text{ s}^{-1} \text{ Pa}^{-1}$ for AAC2.5, and $246 \times 10^{-6} \text{ mol m}^{-2} \text{ s}^{-1} \text{ Pa}^{-1}$ for AAC3.0 at a temperature of 500 °C.

Under similar conditions, the N₂ gas permeance values decreased as a function of temperature. At 30 °C, the N₂ permeance was measured as follows: $29 \times 10^{-6} \text{ mol m}^{-2} \text{ s}^{-1} \text{ Pa}^{-1}$ for AAC0.5, $50 \times 10^{-6} \text{ mol m}^{-2} \text{ s}^{-1} \text{ Pa}^{-1}$ for AAC1.0, $55 \times 10^{-6} \text{ mol m}^{-2} \text{ s}^{-1} \text{ Pa}^{-1}$ for AAC1.5, $57 \times 10^{-6} \text{ mol m}^{-2} \text{ s}^{-1} \text{ Pa}^{-1}$ for AAC2.0, $78 \times 10^{-6} \text{ mol m}^{-2} \text{ s}^{-1} \text{ Pa}^{-1}$ for AAC2.5, and $81 \times 10^{-6} \text{ mol m}^{-2} \text{ s}^{-1} \text{ Pa}^{-1}$ for AAC3.0. As temperature increased, the H₂ gas permeance of AAC composite membranes decreased to $15 \times 10^{-6} \text{ mol m}^{-2} \text{ s}^{-1} \text{ Pa}^{-1}$ for AAC0.5, $35 \times 10^{-6} \text{ mol m}^{-2} \text{ s}^{-1} \text{ Pa}^{-1}$ for AAC1.0, $37 \times 10^{-6} \text{ mol m}^{-2} \text{ s}^{-1} \text{ Pa}^{-1}$ for AAC1.5, $39 \times 10^{-6} \text{ mol m}^{-2} \text{ s}^{-1} \text{ Pa}^{-1}$ for AAC2.0, $50 \times 10^{-6} \text{ mol m}^{-2} \text{ s}^{-1} \text{ Pa}^{-1}$ for AAC2.5, and $61 \times 10^{-6} \text{ mol m}^{-2} \text{ s}^{-1} \text{ Pa}^{-1}$ for AAC3.0 at a temperature of 500 °C.

According to the results, H₂ permeance at 30 °C of AAC composite membranes is rated as follows: AAC3.0 > AAC2.5 > AAC2.0 > AAC1.5 > AAC1.0 > AAC0.5. In addition, the H₂/N₂ selectivity of AAC composite membranes were calculated. The result demonstrated H₂/N₂ selectivity increased with increasing temperature. At 500 °C, ACC demonstrated highest H₂/N₂ selectivity with the value of 2.23, 2.52, 2.69, 2.40, 3.89 and 4.01 for AAC0.5, AAC1.0, AAC1.5, AAC2.0, AAC2.5 and AAC3.0, respectively.

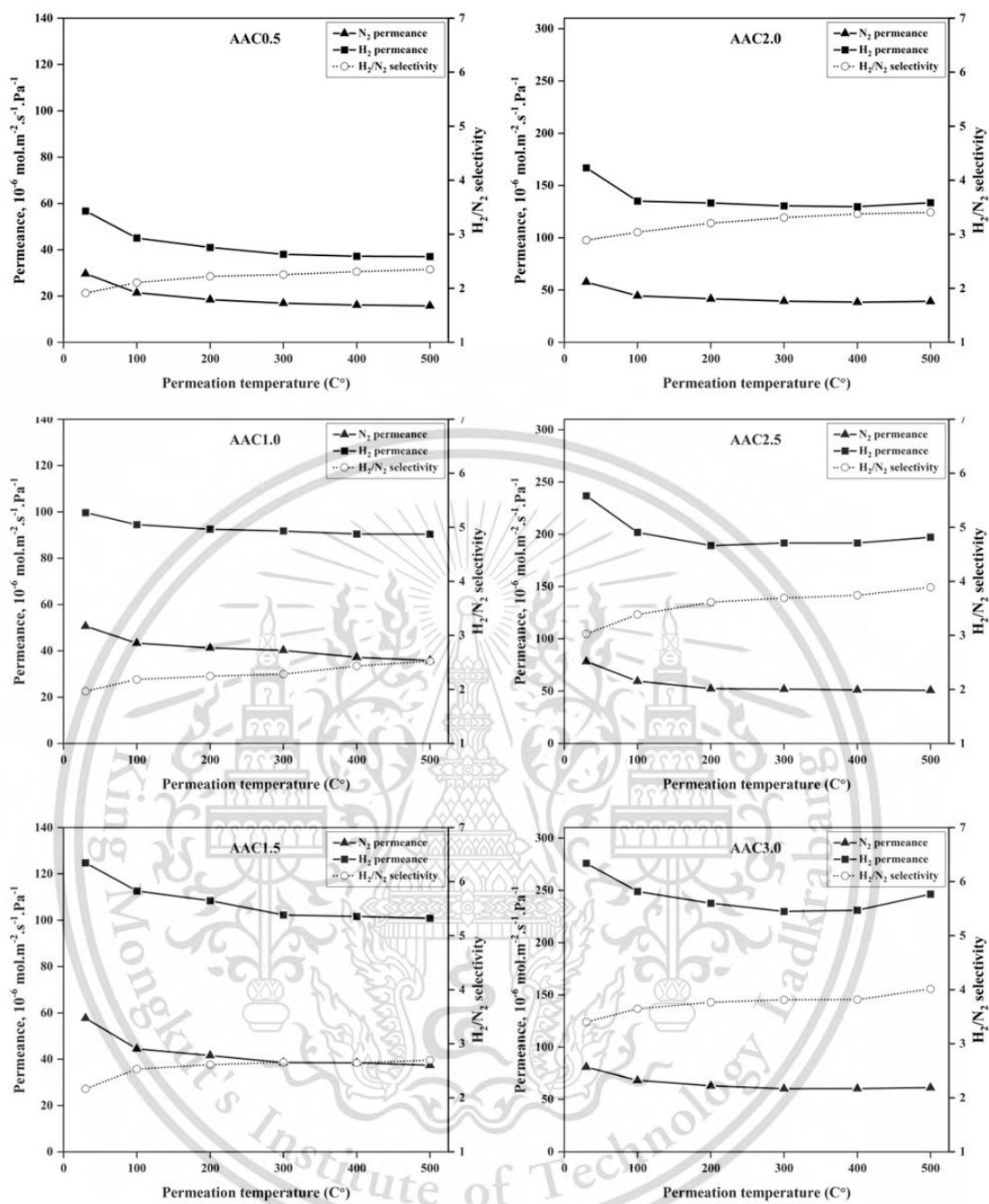


Figure 4.16 H_2 and N_2 gas permeation as a function of the temperature of AAC composite membranes with different activated carbon contents.

Figure 4.17 illustrates the gas permeance performance of ACB composite membranes. The graph reveals that, similar to the Al_2O_3 specimen, the permeance trends of ACB composite membranes generally decline as the transmembrane temperature increases for all the gases examined. Despite the varied rates at which different gases permeate and their distinct responses to changes in carbon black, the overall pattern suggests a common permeation mechanism for all gases. At 30 °C, the H_2 gas permeance values for ACB were determined as follows: $163 \times 10^{-6} \text{ mol m}^{-2} \text{ s}^{-1} \text{ Pa}^{-1}$ for ACB0.5, $186 \times 10^{-6} \text{ mol m}^{-2} \text{ s}^{-1} \text{ Pa}^{-1}$ for ACB1.0, $200 \times 10^{-6} \text{ mol m}^{-2} \text{ s}^{-1} \text{ Pa}^{-1}$ for ACB1.5, $340 \times 10^{-6} \text{ mol m}^{-2} \text{ s}^{-1} \text{ Pa}^{-1}$ for ACB2.0, $391 \times 10^{-6} \text{ mol m}^{-2} \text{ s}^{-1} \text{ Pa}^{-1}$ for ACB2.5, and $508 \times 10^{-6} \text{ mol m}^{-2} \text{ s}^{-1} \text{ Pa}^{-1}$ for ACB3.0. With an increase in temperature to 500 °C, the H_2 gas permeance of ACB composite membranes decreased to $100 \times 10^{-6} \text{ mol m}^{-2} \text{ s}^{-1} \text{ Pa}^{-1}$ for ACB0.5, $118 \times 10^{-6} \text{ mol m}^{-2} \text{ s}^{-1} \text{ Pa}^{-1}$ for ACB1.0, $146 \times 10^{-6} \text{ mol m}^{-2} \text{ s}^{-1} \text{ Pa}^{-1}$ for ACB1.5, $205 \times 10^{-6} \text{ mol m}^{-2} \text{ s}^{-1} \text{ Pa}^{-1}$ for ACB2.0, $328 \times 10^{-6} \text{ mol m}^{-2} \text{ s}^{-1} \text{ Pa}^{-1}$ for ACB2.5, and $356 \times 10^{-6} \text{ mol m}^{-2} \text{ s}^{-1} \text{ Pa}^{-1}$ for ACB3.0.

Under similar conditions, the N_2 gas permeance values also decreased with increasing temperature. At 30 °C, the N_2 permeance was measured as follows: ($56 \times 10^{-6} \text{ mol m}^{-2} \text{ s}^{-1} \text{ Pa}^{-1}$ for ACB0.5, $64 \times 10^{-6} \text{ mol m}^{-2} \text{ s}^{-1} \text{ Pa}^{-1}$ for ACB1.0, $75 \times 10^{-6} \text{ mol m}^{-2} \text{ s}^{-1} \text{ Pa}^{-1}$ for ACB1.5, $114 \times 10^{-6} \text{ mol m}^{-2} \text{ s}^{-1} \text{ Pa}^{-1}$ for ACB2.0, $133 \times 10^{-6} \text{ mol m}^{-2} \text{ s}^{-1} \text{ Pa}^{-1}$ for ACB2.5, and $159 \times 10^{-6} \text{ mol m}^{-2} \text{ s}^{-1} \text{ Pa}^{-1}$ for ACB3.0. As the temperature increased to 500 °C, the N_2 gas permeance of ACB composite membranes decreased to $36 \times 10^{-6} \text{ mol m}^{-2} \text{ s}^{-1} \text{ Pa}^{-1}$ for ACB0.5, $39 \times 10^{-6} \text{ mol m}^{-2} \text{ s}^{-1} \text{ Pa}^{-1}$ for ACB1.0, $44 \times 10^{-6} \text{ mol m}^{-2} \text{ s}^{-1} \text{ Pa}^{-1}$ for ACB1.5, $58 \times 10^{-6} \text{ mol m}^{-2} \text{ s}^{-1} \text{ Pa}^{-1}$ for ACB2.0, $90 \times 10^{-6} \text{ mol m}^{-2} \text{ s}^{-1} \text{ Pa}^{-1}$ for ACB2.5, and $93 \times 10^{-6} \text{ mol m}^{-2} \text{ s}^{-1} \text{ Pa}^{-1}$ for ACB3.0.

Based on the H_2 permeance at 30 °C, the ranking of ACB composite membranes is as follows: $\text{ACB3.0} > \text{ACB2.5} > \text{ACB2.0} > \text{ACB1.5} > \text{ACB1.0} > \text{ACB0.5}$. Additionally, the H_2/N_2 selectivity of AAC composite membranes was calculated, revealing an increase with temperature. At 500 °C, the H_2/N_2 selectivity values were 2.74, 3.01, 3.28, 2.50, 3.65, and 3.82 for ACB0.5, ACB1.0, ACB1.5, ACB2.0, ACB2.5, and ACB3.0, respectively.

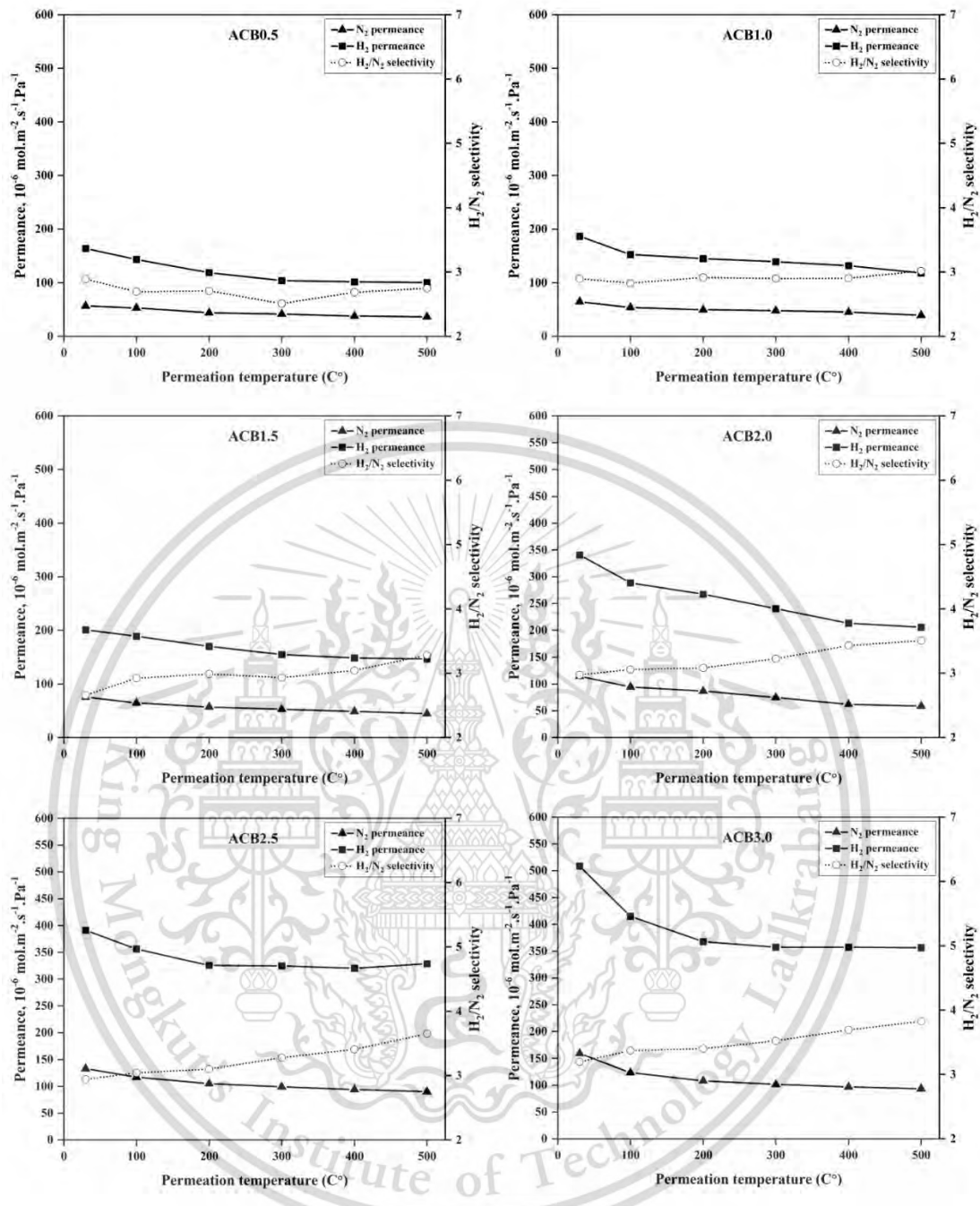


Figure 4.17 H₂ and N₂ gas permeation as a function of the temperature of ACB composite membranes with different carbon black contents.

Figure 4.18 illustrates the gas permeance performance of AGO composite membranes. The result indicates a general decrease in permeance behaviors with an increase in transmembrane temperature for all studied gases, similar to that observed in Al₂O₃ specimen. Although different gases permeate at varying rates and react

This material is reserved for educational use only, not allowed for commercial use.

Forbidden to modify the content, and cite the document when use.

differently to changes in content of graphene oxide, the overall behavior suggests a similar mechanism for all samples. At 30 °C, the H₂ gas permeance values for AGO were determined as follows: $40 \times 10^{-6} \text{ mol m}^{-2} \text{ s}^{-1} \text{ Pa}^{-1}$ for AGO0.5, $41 \times 10^{-6} \text{ mol m}^{-2} \text{ s}^{-1} \text{ Pa}^{-1}$ for AGO1.0, $124 \times 10^{-6} \text{ mol m}^{-2} \text{ s}^{-1} \text{ Pa}^{-1}$ for AGO1.5, $290 \times 10^{-6} \text{ mol m}^{-2} \text{ s}^{-1} \text{ Pa}^{-1}$ for AGO2.0, $408 \times 10^{-6} \text{ mol m}^{-2} \text{ s}^{-1} \text{ Pa}^{-1}$ for AGO2.5, and $410 \times 10^{-6} \text{ mol m}^{-2} \text{ s}^{-1} \text{ Pa}^{-1}$ for AGO3.0. With an increase in temperature to 500 °C, the H₂ gas permeance of AGO composite membranes decreased to $17 \times 10^{-6} \text{ mol m}^{-2} \text{ s}^{-1} \text{ Pa}^{-1}$ for AGO0.5, $24 \times 10^{-6} \text{ mol m}^{-2} \text{ s}^{-1} \text{ Pa}^{-1}$ for AGO1.0, $52 \times 10^{-6} \text{ mol m}^{-2} \text{ s}^{-1} \text{ Pa}^{-1}$ for AGO1.5, $146 \times 10^{-6} \text{ mol m}^{-2} \text{ s}^{-1} \text{ Pa}^{-1}$ for AGO2.0, $232 \times 10^{-6} \text{ mol m}^{-2} \text{ s}^{-1} \text{ Pa}^{-1}$ for AGO2.5, and $250 \times 10^{-6} \text{ mol m}^{-2} \text{ s}^{-1} \text{ Pa}^{-1}$ for AGO3.0.

Under similar conditions, the N₂ gas permeance values decreased with temperature. At 30 °C, the N₂ permeance was measured as follows: $16 \times 10^{-6} \text{ mol m}^{-2} \text{ s}^{-1} \text{ Pa}^{-1}$ for AGO0.5, $13 \times 10^{-6} \text{ mol m}^{-2} \text{ s}^{-1} \text{ Pa}^{-1}$ for AGO1.0, $20 \times 10^{-6} \text{ mol m}^{-2} \text{ s}^{-1} \text{ Pa}^{-1}$ for AGO1.5, $83 \times 10^{-6} \text{ mol m}^{-2} \text{ s}^{-1} \text{ Pa}^{-1}$ for AGO2.0, $99 \times 10^{-6} \text{ mol m}^{-2} \text{ s}^{-1} \text{ Pa}^{-1}$ for AGO2.5, and $101 \times 10^{-6} \text{ mol m}^{-2} \text{ s}^{-1} \text{ Pa}^{-1}$ for AGO3.0. As the experimental temperature increased, the H₂ gas permeance of AGO composite membranes decreased to $5 \times 10^{-6} \text{ mol m}^{-2} \text{ s}^{-1} \text{ Pa}^{-1}$ for AGO0.5, $7 \times 10^{-6} \text{ mol m}^{-2} \text{ s}^{-1} \text{ Pa}^{-1}$ for AGO1.0, $11 \times 10^{-6} \text{ mol m}^{-2} \text{ s}^{-1} \text{ Pa}^{-1}$ for AGO1.5, $41 \times 10^{-6} \text{ mol m}^{-2} \text{ s}^{-1} \text{ Pa}^{-1}$ for AGO2.0, $56 \times 10^{-6} \text{ mol m}^{-2} \text{ s}^{-1} \text{ Pa}^{-1}$ for AGO2.5, and $60 \times 10^{-6} \text{ mol m}^{-2} \text{ s}^{-1} \text{ Pa}^{-1}$ for AGO3.0 at a temperature of 500 °C.

In terms of H₂ permeance at 30 °C, AAC composite membranes are rated as follows: AGO2.5 > AGO3.0 > AGO2.0 > AGO1.5 > AGO1.0 > AGO0.5. Additionally, the H₂/N₂ selectivity of AAC composite membranes was calculated. The results demonstrated that H₂/N₂ selectivity tended to increase with graphene oxide addition, the each experimental showing the highest H₂/N₂ selectivity values of 3.08, 3.11, 3.01, 3.84, 4.45, and 4.20 for AGO0.5, AGO1.0, AGO1.5, AGO2.0, AGO2.5, and AGO3.0, respectively.

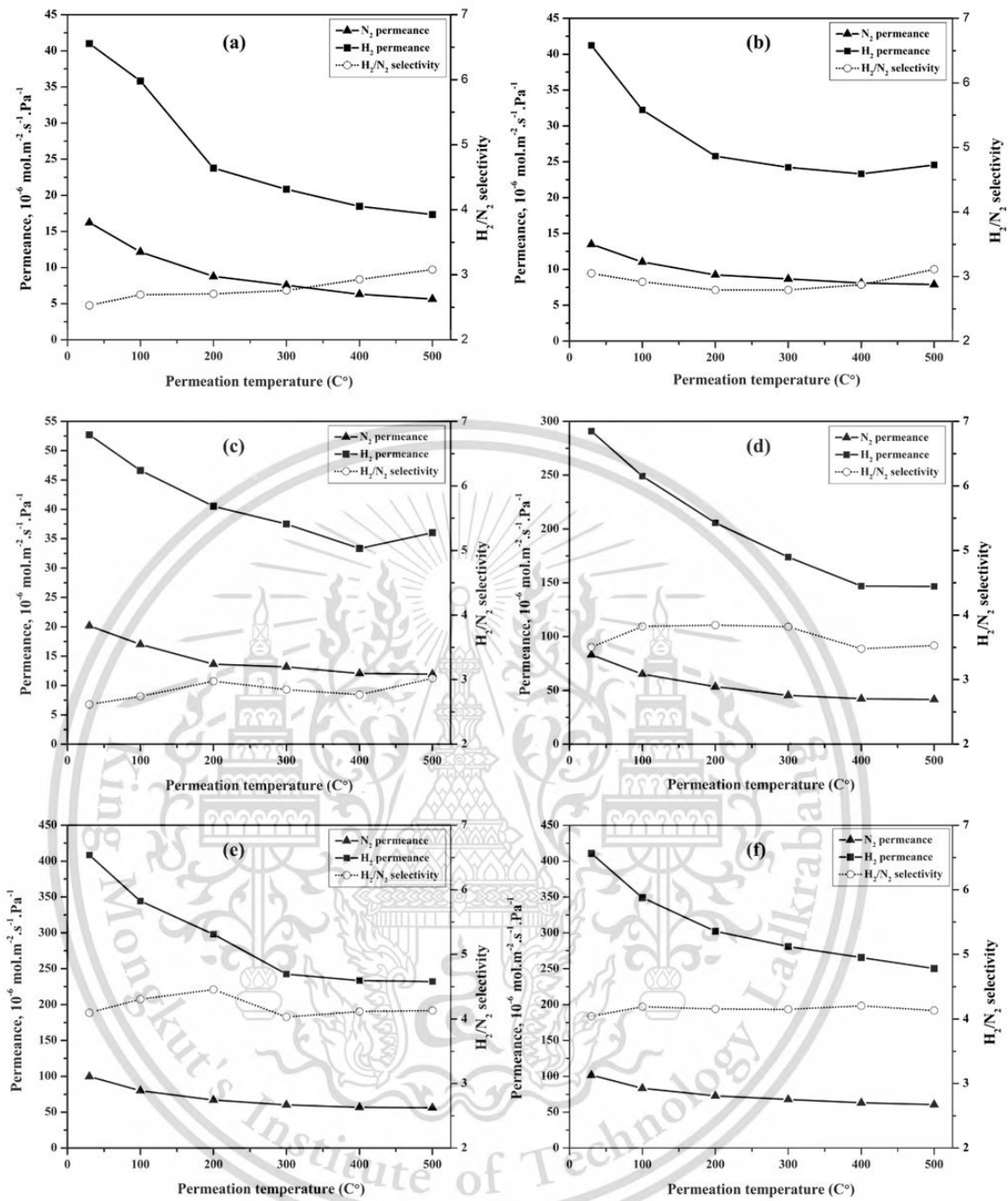


Figure 4.18 H_2 and N_2 gas permeation as a function of the temperature of AGO composite membranes with different graphene oxide contents.

Figure 4.19 illustrates the gas permeance performance of AGP composite membranes. The results indicate that, similar to the Al_2O_3 specimen, the permeance behaviors of AGP composite membranes generally decrease with increasing transmembrane temperature for all studied gases. Despite variations in permeation

This material is reserved for educational use only, not allowed for commercial use.

rates and responses to graphite changes among different gases, the overall trend suggests a similar permeation mechanism for all. At 30 °C, the H₂ gas permeance values for AGP were determined as follows: $222 \times 10^{-6} \text{ mol m}^{-2} \text{ s}^{-1} \text{ Pa}^{-1}$ for AGP0.5, $272 \times 10^{-6} \text{ mol m}^{-2} \text{ s}^{-1} \text{ Pa}^{-1}$ for AGP1.0, $298 \times 10^{-6} \text{ mol m}^{-2} \text{ s}^{-1} \text{ Pa}^{-1}$ for AGP1.5, $297 \times 10^{-6} \text{ mol m}^{-2} \text{ s}^{-1} \text{ Pa}^{-1}$ for AGP2.0, $336 \times 10^{-6} \text{ mol m}^{-2} \text{ s}^{-1} \text{ Pa}^{-1}$ for AGP2.5, and $403 \times 10^{-6} \text{ mol m}^{-2} \text{ s}^{-1} \text{ Pa}^{-1}$ for AGP3.0. As the temperature increased to 500 °C, the H₂ gas permeance of AGP composite membranes decreased to $72 \times 10^{-6} \text{ mol m}^{-2} \text{ s}^{-1} \text{ Pa}^{-1}$ for AGP0.5, $79 \times 10^{-6} \text{ mol m}^{-2} \text{ s}^{-1} \text{ Pa}^{-1}$ for AGP1.0, $80 \times 10^{-6} \text{ mol m}^{-2} \text{ s}^{-1} \text{ Pa}^{-1}$ for AGP1.5, $97 \times 10^{-6} \text{ mol m}^{-2} \text{ s}^{-1} \text{ Pa}^{-1}$ for AGP2.0, $137 \times 10^{-6} \text{ mol m}^{-2} \text{ s}^{-1} \text{ Pa}^{-1}$ for AGP2.5, and $251 \times 10^{-6} \text{ mol m}^{-2} \text{ s}^{-1} \text{ Pa}^{-1}$ for AGP3.0.

Under similar conditions, N₂ gas permeance values decreased with temperature. At 30 °C, the N₂ permeance was measured as follows: $72 \times 10^{-6} \text{ mol m}^{-2} \text{ s}^{-1} \text{ Pa}^{-1}$ for AGP0.5, $87 \times 10^{-6} \text{ mol m}^{-2} \text{ s}^{-1} \text{ Pa}^{-1}$ for AGP1.0, $90 \times 10^{-6} \text{ mol m}^{-2} \text{ s}^{-1} \text{ Pa}^{-1}$ for AGP1.5, $83 \times 10^{-6} \text{ mol m}^{-2} \text{ s}^{-1} \text{ Pa}^{-1}$ for AGP2.0, $93 \times 10^{-6} \text{ mol m}^{-2} \text{ s}^{-1} \text{ Pa}^{-1}$ for AGP2.5, and $99 \times 10^{-6} \text{ mol m}^{-2} \text{ s}^{-1} \text{ Pa}^{-1}$ for AGP3.0. As the experimental temperature increased, the N₂ gas permeance of AAC composite membranes decreased to $31 \times 10^{-6} \text{ mol m}^{-2} \text{ s}^{-1} \text{ Pa}^{-1}$ for AGP0.5, $30 \times 10^{-6} \text{ mol m}^{-2} \text{ s}^{-1} \text{ Pa}^{-1}$ for AGP1.0, $32 \times 10^{-6} \text{ mol m}^{-2} \text{ s}^{-1} \text{ Pa}^{-1}$ for AGP1.5, $33 \times 10^{-6} \text{ mol m}^{-2} \text{ s}^{-1} \text{ Pa}^{-1}$ for AGP2.0, $43 \times 10^{-6} \text{ mol m}^{-2} \text{ s}^{-1} \text{ Pa}^{-1}$ for AGP2.5, and $77 \times 10^{-6} \text{ mol m}^{-2} \text{ s}^{-1} \text{ Pa}^{-1}$ for AGP3.0 at a temperature of 500 °C.

In terms of H₂ permeance at 30 °C, AAC composite membranes are ranked as follows: AGP3.0 > AGP2.5 > AGP2.0 > AGP1.5 > AGP1.0 > AGP0.5. Additionally, the H₂/N₂ selectivity of AGP composite membranes was calculated. The results demonstrated that H₂/N₂ selectivity decreased with temperature. At 30 °C the membranes show the highest selectivity values of 3.08, 3.11, 3.30, 3.57, 3.62, and 4.03 for AAC0.5, AAC1.0, AAC1.5, AAC2.0, AAC2.5, and AAC3.0, respectively.

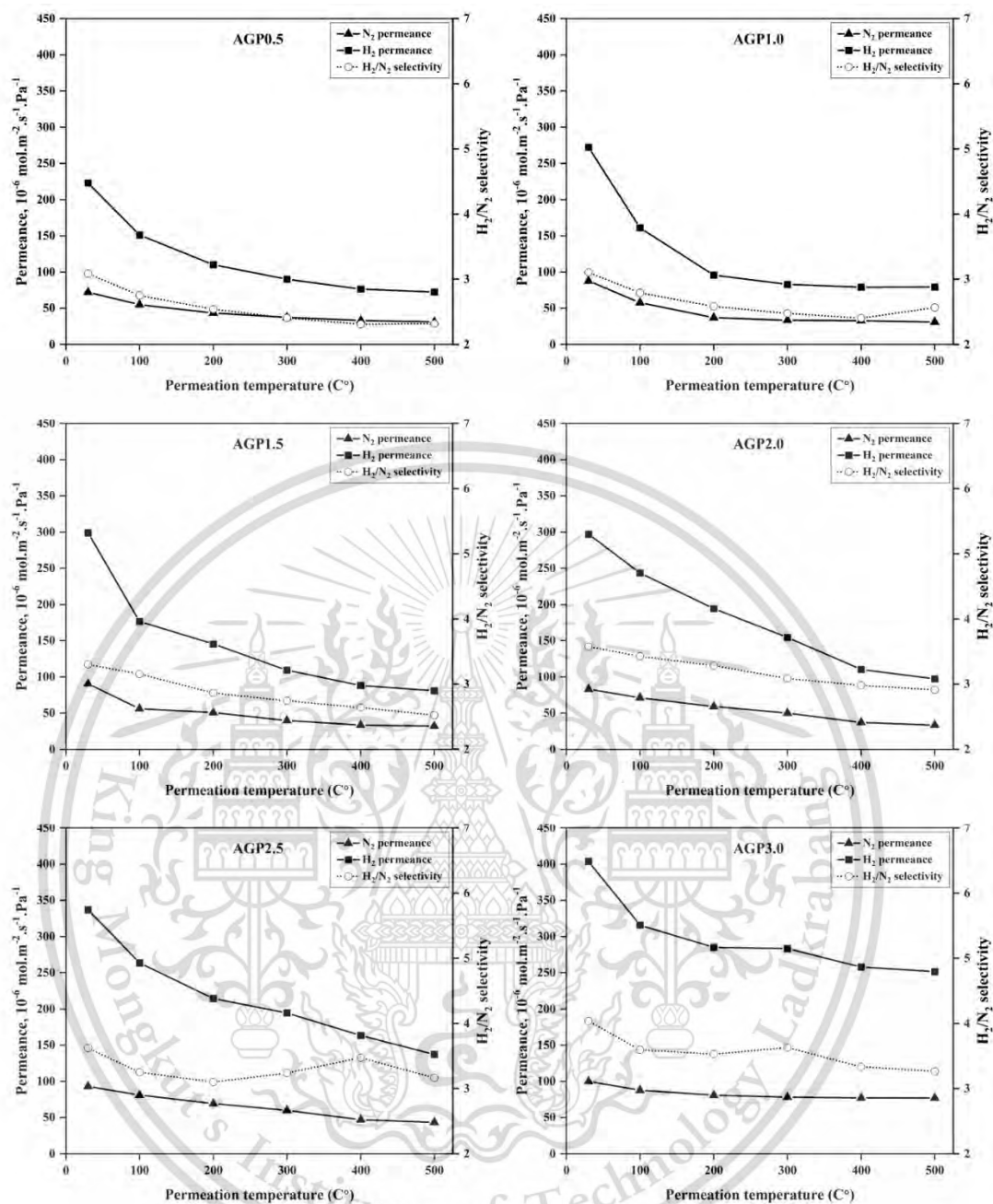


Figure 4.19 H₂ and N₂ gas permeation as a function of the temperature of AGP composite membranes with different graphite contents.

From above experiment, the details of the maximum permeability and selectivity values of Al₂O₃-carbon composite membranes with varying carbon content of 0.5-3.0wt% for all four types can be summarized as follows:

- For AAC membranes, the hydrogen gas permeability values ranged from 37 to 275 × 10⁻⁶ mol m⁻² s⁻¹ Pa⁻¹, with selectivity values falling within the range

This material is reserved for educational use only, not allowed for commercial use.

Forbidden to modify the content, and cite the document when use.

of 2.35 to 4.01. The composite with 3.0wt% activated carbon (AAC3.0) yielded the best test results, with a hydrogen gas permeance of $275 \times 10^{-6} \text{ mol m}^{-2} \text{ s}^{-1} \text{ Pa}^{-1}$ and a selectivity of 4.01 at 500 °C.

- For ACB membranes, the hydrogen gas permeance values ranged from 100 to $508 \times 10^{-6} \text{ mol m}^{-2} \text{ s}^{-1} \text{ Pa}^{-1}$, with selectivity values falling within the range of 3.08 to 3.82. The composite with 3.0wt% carbon black (ACB3.0) provided the best test results, with a hydrogen gas permeability of $508 \times 10^{-6} \text{ mol m}^{-2} \text{ s}^{-1} \text{ Pa}^{-1}$ and a selectivity of 3.82 at 500 °C.
- For AGO membranes, the hydrogen gas permeance values ranged from 17 to $408 \times 10^{-6} \text{ mol m}^{-2} \text{ s}^{-1} \text{ Pa}^{-1}$, with selectivity values falling within the range of 2.10 to 4.45. The composite with 2.5wt% graphene oxide (AGO2.5) exhibited the best test results, with a hydrogen gas permeability of $408 \times 10^{-6} \text{ mol m}^{-2} \text{ s}^{-1} \text{ Pa}^{-1}$ and a selectivity of 4.45 at 200 °C.
- For AGP membranes, the hydrogen gas permeability values ranged from 72 to $403 \times 10^{-6} \text{ mol m}^{-2} \text{ s}^{-1} \text{ Pa}^{-1}$, and selectivity values are within the range of 3.08 to 4.03. The composite with 3.0wt% graphite (AGP3.0) yielded the best test results, with a hydrogen gas permeability of $403 \times 10^{-6} \text{ mol m}^{-2} \text{ s}^{-1} \text{ Pa}^{-1}$ and a selectivity of 4.03 at a testing temperature of 30 °C.

Analysis of the results suggests that the permeation of hydrogen gas in alumina-carbon composite membranes primarily occurs via the Knudsen diffusion mechanism. This mechanism dominates when the average pore size within the membrane is smaller than the mean free path, which signifies the average distance a gas molecule travels between collisions. In such scenarios, the limited pore size facilitates frequent collisions between gas molecules and the pore walls, hindering their movement. Consequently, smaller and lighter molecules, like hydrogen, can permeate the membrane more efficiently, resulting in an ideal selectivity value of 3.75 for the H_2/N_2 separation [83,84]. The membrane achieves gas separation through the Knudsen diffusion mechanism rather than molecular sieving, mainly due to the relatively large pore sizes prepared in the membrane ranging from 0.086 to 0.235 μm . In addition, Figure 4.20 presented the permeance mechanism of the N_2 and H_2 across the composite membranes based on Al_2O_3 composite membranes. Incorporation of GO

This material is reserved for educational use only, not allowed for commercial use.

nanosheets or carbon materials into the Al₂O₃ matrix leads to the formation of confined gas transport pathways due to pore decoration and intergranular distribution. This restricted pore size impedes the diffusion of larger gas molecules, like N₂, promoting selective transport behavior.

Table 4.1 illustrates the correlation between hydrogen permeance and H₂/N₂ selectivity for GO-ceramic membranes as documented in existing literature alongside the findings of this study. Previous research examining GO modifications on ceramic hollow fibers or tubes revealed H₂ permeance levels below 10⁻⁶ mol m⁻² s⁻¹ Pa⁻¹, with selectivity ranging from 3.3 to 900. Notably, the AGO membranes developed in this study exhibit superior H₂ permeance, suggesting a significant enhancement in H₂ permeation performance attributable to the presence of GO within the membrane. Nevertheless, when incorporating other types of carbon, high hydrogen permeation rates of around 10⁻⁴ mol m⁻² s⁻¹ Pa⁻¹ were observed.

Table 4.1 Comparing the experimental performance qualitatively regarding hydrogen permeance and H₂/N₂ ideal selectivity.

Membranes	H ₂ permeance (mol m ⁻² s ⁻¹ Pa ⁻¹)	H ₂ /N ₂ Selectivity	References
Al ₂ O ₃ /GO (flat)	1.00 × 10 ⁻⁸	900	[85]
YSZ/GO (hollow)	4.46 × 10 ⁻⁸	64.0	[86]
Al ₂ O ₃ /Zeolite/GO (hollow)	1.22 × 10 ⁻⁷	40.7	[87]
Al ₂ O ₃ /TiO ₂ /GO (hollow)	3.00 × 10 ⁻⁷	9.00	[88]
GO (flat)	1.50 × 10 ⁻⁶	7.90	[89]
MgAl ₂ O ₃ /GO (hollow)	8.20 × 10 ⁻⁷	3.30	[90]
AAC3.0	275 × 10 ⁻⁶	4.01	This work
ACB3.0	508 × 10 ⁻⁶	3.82	
AGO2.5	408 × 10 ⁻⁶	4.20	
AGP3.0	403 × 10 ⁻⁶	4.03	

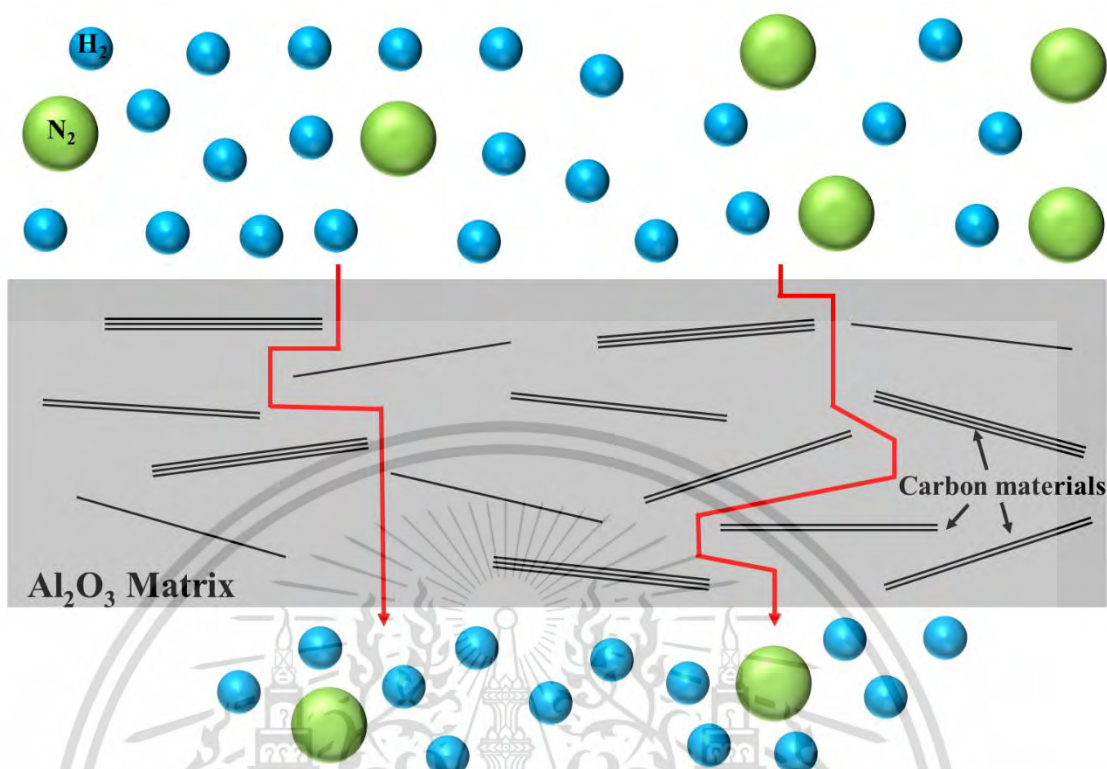


Figure 4.20 Schematic of gas separation of Al_2O_3 -carbon composite membranes.

4.7 Hydrogen sulfide removal

Based on the results from the previous section, the single gas permeation experiment the AGO composite membrane presented the good H_2/N_2 selectivity compared with another composite membranes. Therefore, further investigation was conducted on AGO composite membranes to investigate their performance in absorbing hydrogen sulfide (H_2S) gas. AGO composite sorbents were examined in terms of their ability to absorb H_2S and were compared with unmodified Al_2O_3 sorbents.

Figure 4.21 demonstrate the breakthrough curves of the AGO composites. The concentration of H_2S at the outlet of the reactor was monitored over time at ambient temperature. Irrespective of the initial graphene oxide (GO) content, no H_2S was released until a designated point in time, referred to as the H_2S breakthrough time. At this point, the concentration of H_2S experienced a sudden increase and then remained stable. The region above the breakthrough curve for each adsorbent material in Figure 4.21 was integrated, and subsequently, the overall concentration of released H_2S gas was determined, representing the H_2S breakthrough capacity.

This material is reserved for educational use only, not allowed for commercial use.

Forbidden to modify the content, and cite the document when use.

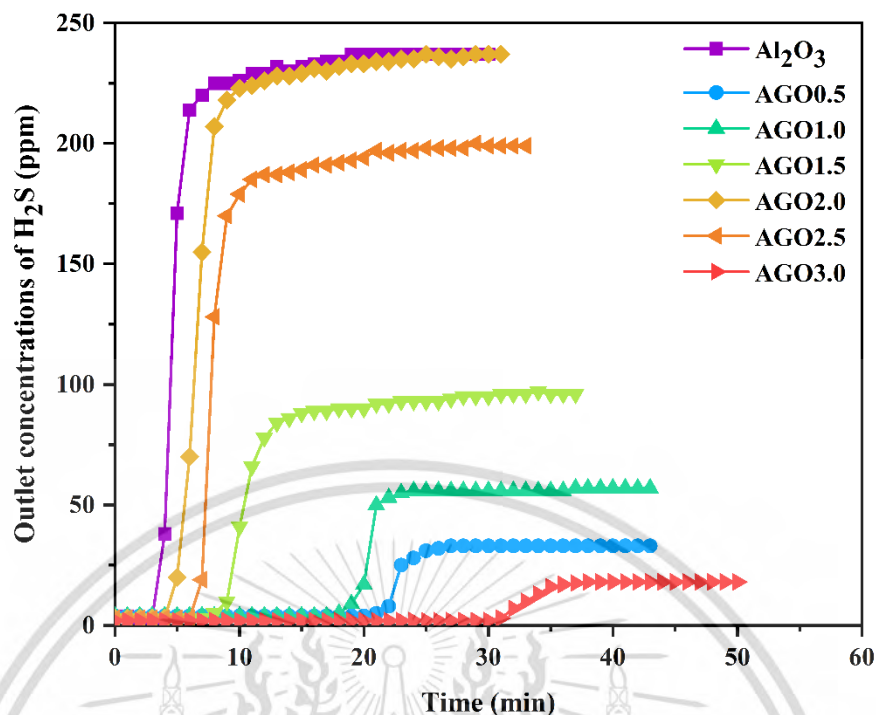


Figure 4.21 The H_2S concentration in the outlet gas stream as a function of time of AGO composite membranes.

Consequently, Figure 4.22 illustrates the obtained H_2S breakthrough capacity. Initially, the breakthrough capacity of AGO sorbent composites increased to 0.29 mg/g with the incorporation of AGO0.5. However, further addition of GO beyond 0.5 wt% resulted in a decline in breakthrough capacity, reaching the lowest value of 0.07 mg/g of AGO2.0. Subsequently, the breakthrough capacity started to rise again, reaching its peak at 0.43 mg/g with a AGO3.0.

According to the data depicted in Figure 4.22, the sorbents are ranked in terms of their efficacy in removing H_2S at ambient temperature as follows: AGO3.0 > AGO0.5 > AGO1.0 > AGO1.5 > AGO2.5 > AGO2.0 > pristine Al_2O_3 . The six novel GO-based sorbents exhibited superior performance compared to the pristine Al_2O_3 sorbent, indicating the efficacy of GO in H_2S removal. Typically, breakthrough capacity is correlated with the surface area of sorbents; however, the breakthrough capacity of AGO did not follow a clear trend with increasing surface area. This study suggests that the breakthrough capacity of the AGO adsorbent is influenced by both GO content and pore structure. When considering average pore diameter, the H_2S adsorption capacity

tended to decrease as the average pore diameter increased. It is hypothesized that the small pore size of the adsorbent resulted in a lower flow rate of H_2S gas, allowing for effective reaction with GO. AGO0.5, with the lowest average pore diameter (0.09 μm), demonstrated high H_2S adsorption capacity. On the other hand, AGO1.0 to AGO2.0 exhibited an increase in pore size (ranging from 0.12–0.23 μm), potentially facilitating the rapid transport of H_2S gas through the adsorbent and reducing the adsorption ability of GO. However, AGO3.0 displayed the highest breakthrough capacity despite its large pore size (0.23 μm), suggesting that the 3 wt% GO content might be the optimal amount enhancing the reaction of AGO sorbent with H_2S .

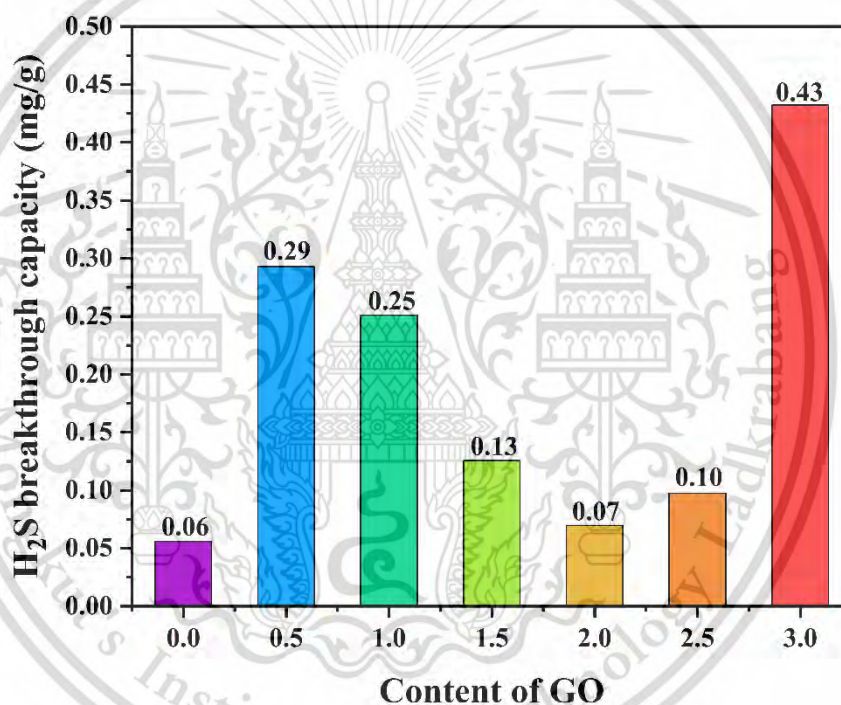


Figure 4.22 H_2S breakthrough capacity as a function of GO content.

Figure 4.23 provides a schematic representation of a mechanism for the removal of H_2S by AGO composites. When GO nanosheets in Al_2O_3 are exposed to an atmosphere containing H_2S , the functional oxygen in GO may initiate the reduction of H_2S molecules, producing sulfur that is captured at oxygen vacancy sites on the GO surface. The reduced hydrogen from H_2S then interacts with oxygen from GO to form H_2O molecules as byproducts.

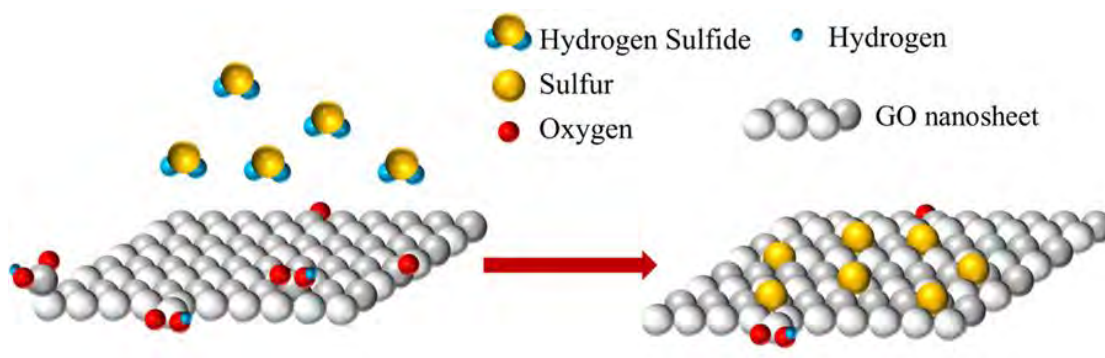


Figure 4.23 Schematic representation of one feasible mechanism of AGO composite for H₂S removal.

In addition, Table 4.2 presents a comparison of the H₂S breakthrough capacity with relevant literature. A review of the literature indicates that the H₂S breakthrough capacity of AGO3.0 is lower than that of metal oxides such as iron oxide (FeO) [91] and zinc oxide (ZnO) [92]. However, when compared to Kaolin/AC6% [93], AGO3.0 demonstrates superior performance and is comparable to α -FeOOH/AC30wt% [94]. In this study, the highest H₂S adsorption capacity was observed for AGO with 3 wt% GO. There is a possibility that a further increase in GO content could lead to an enhancement in H₂S adsorption capacity. It is noteworthy that the synthesis of GO in a college laboratory offers an economical and efficient sorbent for H₂S adsorption at ambient temperatures.

Table 4.2 The breakthrough time and H₂S breakthrough capacity compared to literature.

Type of adsorbent	Flow rate (mL/min)	Breakthrough h time (min)	H ₂ S	References
			breakthrough capacity (mg/g)	
Fe ₂ O ₃ -based	50	458	17.4	[91]
ZnO	150	76	28	[92]
ZnO ₂ -Al ₂ O ₃	150	140	52	[92]
Kaolin/6wt%AC	50	420	0.17	[93]
α -FeOOH/AC30wt%	300	-	0.48	[94]
AGO3.0	10	31	0.43	This study

This material is reserved for educational use only; not allowed for commercial use.

Forbidden to modify the content, and cite the document when use.

Chapter 5

Conclusion

In this research, The Al₂O₃-carbon composite membranes were successfully fabricated via high-temperature sintering at 1500 °C for 2 h with a heating rate and cooldown rate of 5 °C/min under argon atmosphere. Four types of carbon materials were utilized: activated carbon, carbon black, graphene oxide, and graphite. Each carbon material was added at content of 0.5, 1.0, 1.5, 2.0, 2.5, and 3.0 wt%. The characteristic of the Al₂O₃-carbon composite membranes was systemically investigated, a result can be summarized as following:

1. The low-cost Al₂O₃-carbon composite membranes with four types of carbon materials (activated carbon, carbon black, graphene oxide, and graphite) were successfully fabricated by high-temperature sintering at 1500 °C for 2 h under an argon atmosphere.
2. The phase identification of the precursor materials was systematically investigated. Al₂O₃ exhibited a hexagonal crystalline structure with strong peaks corresponding to the (002) plane. For the carbon materials, activated carbon and carbon black displayed an amorphous structure. Graphene oxide showed preferential orientation peaks for the (002) plane. Additionally, preferential orientation peaks for the (002) plane of graphite were observed. Both graphene oxide and graphite demonstrated hexagonal crystalline structures, with d-spacings of 0.8 nm and 0.4 nm for graphene oxide and graphite, respectively.
3. The phase identification of each Al₂O₃-carbon composite membrane was studied. Each Al₂O₃-carbon composite membrane demonstrated the single phase of Al₂O₃ only, owing to the strong peaks of Al₂O₃ inhibiting the carbon phase.
4. The physical properties of the Al₂O₃-carbon composite membranes were measured using Archimedes principle. The results demonstrated that the addition of carbon materials improves the physical properties of the composite membranes. In particular, the content of carbon at 0.5 wt% exhibited the most effective improvement in bulk density, with the density increasing by 59.83%,

This material is reserved for educational use only, not allowed for commercial use.

Forbidden to modify the content, and cite the document when use.

43.23%, 59.38%, and 51.97% for AAC, ACB, AGO, and AGP, respectively. Additionally, the relative density increased by over 60.16%, 31.22%, 61.01%, and 52.20% for AAC, ACB, AGO, and AGP, respectively, compared to the pure Al_2O_3 specimen.

5. Analysis of the Al_2O_3 -carbon composite membrane surfaces revealed that incorporating carbon materials resulted in clear grain boundaries compared to the pure Al_2O_3 specimen. Furthermore, the addition of carbon also led to an increase in the grain size of the composite membranes.
6. The pore sizes distribution analysis of the Al_2O_3 -carbon composite membranes reveals a consistent presence of macroporous structures for all specimens.
7. The mechanical properties of Al_2O_3 -carbon composite membranes were measured via Vickers hardness. The addition of carbon materials improved the hardness of the composite membranes. In Comparison the hardness between 0.5wt% of carbon addition specimens and pure Al_2O_3 specimens, the hardness increased to 333%, 383%, 506%, and 462% for AAC, ACB, AGO, and AGP, respectively,
8. The incorporation of carbon materials into Al_2O_3 significantly enhanced the hydrogen gas permeation through the resulting Al_2O_3 -carbon composite membranes. The highest hydrogen permeance values were observed for AAC (3.0 wt% carbon addition) at $275 \times 10^{-6} \text{ mol m}^{-2} \text{ s}^{-1} \text{ Pa}^{-1}$, followed by ACB (3.0 wt% carbon addition) at $508 \times 10^{-6} \text{ mol m}^{-2} \text{ s}^{-1} \text{ Pa}^{-1}$, AGO (2.5 wt% carbon addition) at $408 \times 10^{-6} \text{ mol m}^{-2} \text{ s}^{-1} \text{ Pa}^{-1}$, and AGP (3.0 wt% carbon addition) at $403 \times 10^{-6} \text{ mol m}^{-2} \text{ s}^{-1} \text{ Pa}^{-1}$. Additionally, H_2/N_2 selectivity was also enhanced, with the highest values for each carbon type being 4.01 (AAC, 3.0 wt% carbon), 3.82 (ACB, 3.0 wt% carbon), 4.20 (AGO, 2.5 wt% carbon), and 4.03 (AGP, 3.0 wt% carbon). In addition, based on the observed selectivity, the dominant gas transport mechanism in these Al_2O_3 -carbon composite membranes was Knudsen diffusion, generally of macroporous membranes.
9. Experiments measuring hydrogen sulfide (H_2S) capture revealed that AGO adsorbents are effective in enhancing H_2S adsorption. All AGO materials displayed

This material is reserved for educational use only, not allowed for commercial use.

Forbidden to modify the content, and cite the document when use.

greater H₂S adsorption capacity compared to the pure Al₂O₃ sorbent. Notably, AGO3.0 achieved the highest capacity, reaching 0.43 mg/g.

Based on the experimental results, the incorporation of carbon materials significantly enhanced the performance of Al₂O₃-carbon composite membranes. Considering the fabrication process, cost, and performance, Al₂O₃-carbon composite membranes have the potential to be used for industrial-scale gas separation, especially for primary separation applications.

Suggestions

Our research findings indicate that incorporating carbon materials significantly improved the physical and mechanical properties, as well as the single gas permeance, particularly in terms of hydrogen permeability, of the alumina-carbon composite membranes. However, the performance in terms of gas selectivity did not meet expectations. Therefore, further development of membranes to enhance hydrogen selectivity should be pursued. To address this issue, future work should focus on incorporating additional chemical elements to decrease pore size, thereby rejecting gases with molecular sizes larger than hydrogen. Additionally, employing coating techniques can further enhance hydrogen selectivity. However, it is crucial to ensure that these enhancements in selectivity do not compromise hydrogen permeability.

References

- [1] P.E. Brockway, A. Owen, L.I. Brand-Correa, L. Hardt, Estimation of global final-stage energy-return-on-investment for fossil fuels with comparison to renewable energy sources, *Nat Energy* 4 (2019) 612–621. <https://doi.org/10.1038/s41560-019-0425-z>.
- [2] M. Amin, H.H. Shah, A.G. Fareed, W.U. Khan, E. Chung, A. Zia, Z.U. Rahman Farooqi, C. Lee, Hydrogen production through renewable and non-renewable energy processes and their impact on climate change, *Int J Hydrogen Energy* 47 (2022) 33112–33134. <https://doi.org/10.1016/j.ijhydene.2022.07.172>.
- [3] C. Ruocco, V. Palma, A. Ricca, Kinetics of Oxidative Steam Reforming of Ethanol Over Bimetallic Catalysts Supported on CeO₂–SiO₂: A Comparative Study, *Top Catal* 62 (2019) 467–478. <https://doi.org/10.1007/s11244-019-01173-2>.
- [4] M.A. Valenzuela, B. Zapata, Hydrogen production, Hydroprocessing of Heavy Oils and Residua (2007) 313–338. https://doi.org/10.1299/jsmemag.119.1169_182.
- [5] I. Dincer, Green methods for hydrogen production, *Int J Hydrogen Energy* 37 (2012) 1954–1971. <https://doi.org/10.1016/j.ijhydene.2011.03.173>.
- [6] Z. Abdin, A. Zafaranloo, A. Rafiee, W. Mérida, W. Lipiński, K.R. Khalilpour, Hydrogen as an energy vector, *Renewable and Sustainable Energy Reviews* 120 (2020). <https://doi.org/10.1016/j.rser.2019.109620>.
- [7] W.T. LIBERSON, Functional electrotherapy., *Trans Am Soc Artif Intern Organs* 8 (1962) 373–377. <https://doi.org/10.1097/00002480-196204000-00075>.
- [8] N. Sazali, A review of the application of carbon-based membranes to hydrogen separation, *J Mater Sci* 55 (2020) 11052–11070. <https://doi.org/10.1007/s10853-020-04829-7>.
- [9] R. Yukesh Kannah, S. Kavitha, Preethi, O. Parthiba Karthikeyan, G. Kumar, N.V. Dai-Viet, J. Rajesh Banu, Techno-economic assessment of various hydrogen production methods – A review, *Bioresour Technol* 319 (2021) 124175. <https://doi.org/10.1016/j.biortech.2020.124175>.

This material is reserved for educational use only, not allowed for commercial use.

Forbidden to modify the content, and cite the document when use.

- [10] I. Dincer, C. Zamfirescu, Hydrogen Production by Biochemical Energy, Sustainable Hydrogen Production (2016) 393–409. <https://doi.org/10.1016/b978-0-12-801563-6.00006-6>.
- [11] J. Li, W. Cheng, Comparative life cycle energy consumption, carbon emissions and economic costs of hydrogen production from coke oven gas and coal gasification, Int J Hydrogen Energy 45 (2020) 27979–27993. <https://doi.org/10.1016/j.ijhydene.2020.07.079>.
- [12] V. Singh, I. Dincer, M.A. Rosen, Life Cycle Assessment of Ammonia Production Methods, Elsevier, 2018. <https://doi.org/10.1016/B978-0-12-813734-5.00053-6>.
- [13] G. Perkins, Underground coal gasification – Part I: Field demonstrations and process performance, Prog Energy Combust Sci 67 (2018) 158–187. <https://doi.org/10.1016/j.pecs.2018.02.004>.
- [14] Y. Wang, Y. Wang, S. Song, T. Wang, D. Li, H. Tan, Effects of coal types and combustion conditions on carbonaceous aerosols in flue gas and their light absorption properties, Fuel 277 (2020) 118148. <https://doi.org/10.1016/j.fuel.2020.118148>.
- [15] J.M.K. O’Keefe, A. Bechtel, K. Christanis, S. Dai, W.A. DiMichele, C.F. Eble, J.S. Esterle, M. Mastalerz, A.L. Raymond, B. V. Valentim, N.J. Wagner, C.R. Ward, J.C. Hower, On the fundamental difference between coal rank and coal type, Int J Coal Geol 118 (2013) 58–87. <https://doi.org/10.1016/j.coal.2013.08.007>.
- [16] T. Lepage, M. Kammoun, Q. Schmetz, A. Richel, Biomass-to-hydrogen: A review of main routes production, processes evaluation and techno-economical assessment, Biomass Bioenergy 144 (2021) 105920. <https://doi.org/10.1016/j.biombioe.2020.105920>.
- [17] F. Suleman, I. Dincer, M. Agelin-Chaab, Environmental impact assessment and comparison of some hydrogen production options, Int J Hydrogen Energy 40 (2015) 6976–6987. <https://doi.org/10.1016/j.ijhydene.2015.03.123>.

- [18] M. Ball, M. Wietschel, The future of hydrogen - opportunities and challenges, *Int J Hydrogen Energy* 34 (2009) 615–627. <https://doi.org/10.1016/j.ijhydene.2008.11.014>.
- [19] X. Sun, H.K. Atiyeh, R.L. Huhnke, R.S. Tanner, Syngas fermentation process development for production of biofuels and chemicals: A review, *Bioresour Technol Rep* 7 (2019) 100279. <https://doi.org/10.1016/j.biteb.2019.100279>.
- [20] W.X. Peng, L.S. Wang, M. Mirzaee, H. Ahmadi, M.J. Esfahani, S. Fremaux, Hydrogen and syngas production by catalytic biomass gasification, *Energy Convers Manag* 135 (2017) 270–273. <https://doi.org/10.1016/j.enconman.2016.12.056>.
- [21] E. Shayan, V. Zare, I. Mirzaee, Hydrogen production from biomass gasification; a theoretical comparison of using different gasification agents, *Energy Convers Manag* 159 (2018) 30–41. <https://doi.org/10.1016/j.enconman.2017.12.096>.
- [22] G. Moral, R. Ortiz-lmedio, A. Ortiz, D. Gorri, I. Ortiz, Hydrogen Recovery from Coke Oven Gas. Comparative Analysis of Technical Alternatives, *Ind Eng Chem Res* 61 (2022) 6106–6124. <https://doi.org/10.1021/acs.iecr.1c04668>.
- [23] P.S. Adsorption, Production, (2010) 414–450.
- [24] D. Edlund, Hydrogen Membrane Technologies and Application in Fuel Processing, *Hydrogen and Syngas Production and Purification Technologies* (2009) 357–384. <https://doi.org/10.1002/9780470561256.ch8>.
- [25] P. Bernardo, E. Drioli, G. Golemme, *Ind. Eng. Chem. Res.* 2009, 48, 4638–4663
Gas Sep State of the art Bernardo et al.pdf, *Ind. Eng. Chem.* (2009) 4638–4663.
- [26] I. Uehara, Separation and Purification of Hydrogen, *Encyclopedia of Life Support Systems I* (2009) 268–282.
- [27] Y. Shirasaki, T. Tsuneki, Y. Ota, I. Yasuda, S. Tachibana, H. Nakajima, K. Kobayashi, Development of membrane reformer system for highly efficient hydrogen production from natural gas, *Int J Hydrogen Energy* 34 (2009) 4482–4487. <https://doi.org/10.1016/j.ijhydene.2008.08.056>.

- [28] J.W. Phair, S.P.S. Badwal, Materials for separation membranes in hydrogen and oxygen production and future power generation, *Sci Technol Adv Mater* 7 (2006) 792–805. <https://doi.org/10.1016/j.stam.2006.11.005>.
- [29] R. Zeynali, K. Ghasemzadeh, A. Iulianelli, A. Basile, Experimental evaluation of graphene oxide/TiO₂-alumina nanocomposite membranes performance for hydrogen separation, *Int J Hydrogen Energy* 45 (2020) 7479–7487. <https://doi.org/10.1016/j.ijhydene.2019.02.225>.
- [30] V. Abetz, T. Brinkmann, M. Dijkstra, K. Ebert, D. Fritsch, K. Ohlrogge, D. Paul, K.V. Peinemann, S.P. Nunes, N. Scharnagl, M. Schossig, Developments in membrane research: From material via process design to industrial application, *Adv Eng Mater* 8 (2006) 328–358. <https://doi.org/10.1002/adem.200600032>.
- [31] S.-J. Song, T.H. Lee, E.D. Wachsman, L. Chen, S.E. Dorris, U. Balachandran, Defect Structure and Transport Properties of Ni-SrCeO_{3-δ} Cermet for Hydrogen Separation Membrane, *J Electrochem Soc* 152 (2005) J125. <https://doi.org/10.1149/1.2060690>.
- [32] J.H. Xu, J. Xiang, H. Ding, T.Q. Yu, J. Le Li, Z.G. Li, Y.W. Yang, X. Le Shao, Synthesis and electrical properties of BaCeO₃-based proton conductors by calcinations of metal-polyvinyl alcohol gel, *J Alloys Compd* 551 (2013) 333–337. <https://doi.org/10.1016/j.jallcom.2012.10.107>.
- [33] J.W. Phair, S.P.S. Badwal, Materials for separation membranes in hydrogen and oxygen production and future power generation, *Sci Technol Adv Mater* 7 (2006) 792–805. <https://doi.org/10.1016/j.stam.2006.11.005>.
- [34] T. Norby, R. Haugrud, Dense Ceramic Membranes for Hydrogen Separation, 2006. <https://doi.org/10.1002/3527608796.ch1>.
- [35] J.W. Phair, S.P.S. Badwal, Review of proton conductors for hydrogen separation, *Ionics (Kiel)* 12 (2006) 103–115. <https://doi.org/10.1007/s11581-006-0016-4>.
- [36] S.C. Emerson, S.C. Emerson, N.J. Magdefrau, Y. She, C. Thibaud-erkey, Advanced Palladium Membrane Scale-up for Hydrogen Separation, (2013).
- [37] J. Kozeny, *Ber. Wien. Akad.*, 136a (1927) 27.

This material is reserved for educational use only, not allowed for commercial use.

Forbidden to modify the content, and cite the document when use.

- [38] Y. Wei, J. Xue, H. Wang, J. Caro, Hydrogen permeability and stability of BaCe_{0.85}Tb_{0.05}Zr_{0.1}O_{3- δ} asymmetric membranes, *J Memb Sci* 488 (2015) 173–181. <https://doi.org/10.1016/j.memsci.2015.04.035>.
- [39] N. Sazali, A review of the application of carbon-based membranes to hydrogen separation, *J Mater Sci* 55 (2020) 11052–11070. <https://doi.org/10.1007/s10853-020-04829-7>.
- [40] W.N.W. Salleh, A.F. Ismail, Effect of Stabilization Condition on PEI/PVP-Based Carbon Hollow Fiber Membranes Properties, *Separation Science and Technology (Philadelphia)* 48 (2013) 1030–1039. <https://doi.org/10.1080/01496395.2012.727938>.
- [41] Production & Characterization of Activated Carbon Membranes 81, n.d.
- [42] N.S. Lazarenko, V. V. Golovakhin, A.A. Shestakov, N.I. Lapekin, A.G. Bannov, Recent Advances on Membranes for Water Purification Based on Carbon Nanomaterials, *Membranes (Basel)* 12 (2022). <https://doi.org/10.3390/membranes12100915>.
- [43] C. Li, J. Yang, L. Zhang, S. Li, Y. Yuan, X. Xiao, X. Fan, C. Song, Carbon-based membrane materials and applications in water and wastewater treatment: a review, *Environ Chem Lett* 19 (2021) 1457–1475. <https://doi.org/10.1007/s10311-020-01112-8>.
- [44] S. Sun, B. Sun, Y. Wang, M. Fordjour Antwi-Afari, H.Y. Mi, Z. Guo, C. Liu, C. Shen, Carbon black and polydopamine modified non-woven fabric enabling efficient solar steam generation towards seawater desalination and wastewater purification, *Sep Purif Technol* 278 (2022). <https://doi.org/10.1016/j.seppur.2021.119621>.
- [45] M.E.A. Ali, S. Elbakry, M. Aboelfadl, H. Shawky, Q. Li, F. Perreault, Preparation and characterization of carbon black coated membranes for the treatment of saline water by membrane distillation, *J Coat Technol Res* 20 (2023) 1477–1488. <https://doi.org/10.1007/s11998-023-00759-6>.

- [46] S. Han, B.M. Jun, J.S. Choi, C.M. Park, M. Jang, S.N. Nam, Y. Yoon, Removal of endocrine disruptors and pharmaceuticals by graphene oxide-based membranes in water: A review, *J Environ Manage* 363 (2024). <https://doi.org/10.1016/j.jenvman.2024.121437>.
- [47] R. Zeynali, K. Ghasemzadeh, A.B. Sarand, F. Kheiri, A. Basile, Performance evaluation of graphene oxide (GO) nanocomposite membrane for hydrogen separation: Effect of dip coating sol concentration, *Sep Purif Technol* 200 (2018) 169–176. <https://doi.org/10.1016/j.seppur.2018.02.032>.
- [48] N. Carboni, L. Mazzapioda, A. Capri, I. Gatto, A. Carbone, V. Baglio, M.A. Navarra, Composite anion exchange membranes based on graphene oxide for water electrolyzer applications, *Electrochim Acta* 486 (2024). <https://doi.org/10.1016/j.electacta.2024.144090>.
- [49] X. Chen, Z. Qu, M. Xie, M. Zhang, J. Ai, G. Ren, Y. Gao, Y. Yang, In-situ crosslinking reaction of graphene oxide & waterborne epoxy resin to construct continuous phase anticorrosive coating, *Arabian Journal of Chemistry* 17 (2024). <https://doi.org/10.1016/j.arabjc.2024.105795>.
- [50] A.L. Yurkov, A.P. Malakho, A. V. Ivanov, E.A. Chernova, A.A. Belogorlov, V. V. Avdeev, Studying the porosity of graphite foil with different densities: pore space model and gas permeability, *J Mater Sci* 57 (2022) 21156–21171. <https://doi.org/10.1007/s10853-022-07677-9>.
- [51] A. V. Ivanov, N. V. Maksimova, M.S. Manylov, A.N. Kirichenko, I.L. Kalachev, A.P. Malakho, V. V. Avdeev, Gas permeability of graphite foil prepared from exfoliated graphite with different microstructures, *J Mater Sci* 56 (2021) 4197–4211. <https://doi.org/10.1007/s10853-020-05541-2>.
- [52] E.A. Efimova, D.A. Syrtsova, V. V. Teplyakov, Gas permeability through graphite foil: The influence of physical density, membrane orientation and temperature, *Sep Purif Technol* 179 (2017) 467–474. <https://doi.org/10.1016/j.seppur.2017.02.023>.
- [53] L. Silva, A. Plaza, J. Romero, J. Sanchez, G.M. Rios, Characterization of MFI zeolite membranes by means of permeability determination of near critical

- and supercritical CO₂, *Journal of the Chilean Chemical Society* 53 (2008) 1415–1421. <https://doi.org/10.4067/S0717-97072008000100017>.
- [54] H. Li, Z. Song, X. Zhang, Y. Huang, S. Li, Y. Mao, H.J. Ploehn, Y. Bao, M. Yu, Ultrathin, molecular-sieving graphene oxide membranes for selective hydrogen separation, *Science* (1979) 342 (2013) 95–98. <https://doi.org/10.1126/science.1236686>.
- [55] R. Zeynali, K. Ghasemzadeh, A. Iulianelli, A. Basile, Experimental evaluation of graphene oxide/TiO₂-alumina nanocomposite membranes performance for hydrogen separation, *Int J Hydrogen Energy* 45 (2020) 7479–7487. <https://doi.org/10.1016/j.ijhydene.2019.02.225>.
- [56] S.R.F.L. Ribeiro, L.P. Bessa, V.L. Cardoso, M.H.M. Reis, Enhanced hydrogen permeance through graphene oxide membrane deposited on asymmetric spinel hollow fiber substrate, *Int J Hydrogen Energy* 47 (2022) 9616–9626. <https://doi.org/10.1016/j.ijhydene.2022.01.049>.
- [57] S. Ma, Z. Tang, Y. Fan, J. Zhao, X. Meng, N. Yang, S. Zhuo, S. Liu, Surfactant-modified graphene oxide membranes with tunable structure for gas separation, *Carbon N Y* 152 (2019) 144–150. <https://doi.org/10.1016/j.carbon.2019.06.006>.
- [58] K.I. Kim, T.W. Hong, Hydrogen permeation of TiN-graphene membrane by hot press sintering (HPS) process, *Solid State Ion* 225 (2012) 699–702. <https://doi.org/10.1016/j.ssi.2012.06.003>.
- [59] N.R. Lee, S.S. Lee, K. Il Kim, W.G. Kim, H. Ju, D.M. Kim, T.W. Hong, Fabrications and evaluations of hydrogen permeation on Al₂O₃/CeO₂/graphene (ACG) composites membrane by Hot Press Sintering (HPS), *Int J Hydrogen Energy* 38 (2013) 7654–7658. <https://doi.org/10.1016/j.ijhydene.2012.08.080>.
- [60] M. Kitiwan, T. Goto, Fabrication of tungsten carbide–diamond composites using SiC-coated diamond, *Int J Refract Metals Hard Mater* 85 (2019) 105053. <https://doi.org/10.1016/j.ijrmhm.2019.105053>.

- [61] S. Wang, H. Nam, T.B. Gebreegziabher, H. Nam, Adsorption of acetic acid and hydrogen sulfide using NaOH impregnated activated carbon for indoor air purification, *Engineering Reports 2* (2020). <https://doi.org/10.1002/eng2.12083>.
- [62] M. Singh, R. Vander Wal, Nanostructure Quantification of Carbon Blacks, *C (Basel)* 5 (2018) 2. <https://doi.org/10.3390/c5010002>.
- [63] B. Lian, J. Deng, G. Leslie, H. Bustamante, V. Sahajwalla, Y. Nishina, R.K. Joshi, Surfactant modified graphene oxide laminates for filtration, *Carbon N Y* 116 (2017) 240–245. <https://doi.org/10.1016/j.carbon.2017.01.102>.
- [64] Z.Q. Li, C.J. Lu, Z.P. Xia, Y. Zhou, Z. Luo, X-ray diffraction patterns of graphite and turbostratic carbon, *Carbon N Y* 45 (2007) 1686–1695. <https://doi.org/10.1016/j.carbon.2007.03.038>.
- [65] F.T. Johra, J.W. Lee, W.G. Jung, Facile and safe graphene preparation on solution based platform, *Journal of Industrial and Engineering Chemistry* 20 (2014) 2883–2887. <https://doi.org/10.1016/j.jiec.2013.11.022>.
- [66] B. Yazdani, F. Xu, I. Ahmad, X. Hou, Y. Xia, Y. Zhu, Tribological performance of Graphene/Carbon nanotube hybrid reinforced Al₂O₃ composites, *Sci Rep* 5 (2015). <https://doi.org/10.1038/srep11579>.
- [67] D. Bogachuk, R. Tsuji, D. Martineau, S. Narbey, J.P. Herterich, L. Wagner, K. Suginuma, S. Ito, A. Hinsch, Comparison of highly conductive natural and synthetic graphites for electrodes in perovskite solar cells, *Carbon N Y* 178 (2021) 10–18. <https://doi.org/10.1016/j.carbon.2021.01.022>.
- [68] L. Golubewa, T. Kulahava, Y. Kunitskaya, P. Bulai, M. Shuba, R. Karpicz, Enhancement of single-walled carbon nanotube accumulation in glioma cells exposed to low-strength electric field: Promising approach in cancer nanotherapy, *Biochem Biophys Res Commun* 529 (2020) 647–651. <https://doi.org/10.1016/j.bbrc.2020.06.100>.
- [69] D. López-Díaz, M. López Holgado, J.L. García-Fierro, M.M. Velázquez, Evolution of the Raman Spectrum with the Chemical Composition of Graphene Oxide,

- Journal of Physical Chemistry C 121 (2017) 20489–20497.
<https://doi.org/10.1021/acs.jpcc.7b06236>.
- [70] J. Shen, Y. Hu, M. Shi, X. Lu, C. Qin, C. Li, M. Ye, Fast and facile preparation of graphene oxide and reduced graphene oxide nanoplatelets, *Chemistry of Materials* 21 (2009) 3514–3520. <https://doi.org/10.1021/cm901247t>.
- [71] S. Claramunt, A. Varea, D. López-Díaz, M.M. Velázquez, A. Cornet, A. Cirera, The importance of interbands on the interpretation of the raman spectrum of graphene oxide, *Journal of Physical Chemistry C* 119 (2015) 10123–10129. <https://doi.org/10.1021/acs.jpcc.5b01590>.
- [72] A.H.C. Neto, F. Guinea, N.M.R. Peres, K.S. Novoselov, A.K. Geim, The electronic properties of graphene, (2007). <https://doi.org/10.1103/RevModPhys.81.109>.
- [73] E.N. Mohamed, A.I. Abd-Elhamid, A.A. El-Bardan, H.M.A. Soliman, M.S. Mohy-Eldin, Development of carboxymethyl cellulose-graphene oxide biobased composite for the removal of methylene blue cationic dye model contaminate from wastewater, *Sci Rep* 13 (2023). <https://doi.org/10.1038/s41598-023-41431-8>.
- [74] Kurniasari, A. Maulana, A.Y. Nugraheni, D.N. Jayanti, S. Mustofa, M.A. Baqiya, Darminto, Defect and Magnetic Properties of Reduced Graphene Oxide Prepared from Old Coconut Shell, in: *IOP Conf Ser Mater Sci Eng*, Institute of Physics Publishing, 2017. <https://doi.org/10.1088/1757-899X/196/1/012021>.
- [75] X. Wang, H. Wang, Y. Wang, J. Gao, J. Liu, Y. Zhang, Hydrotalcite/graphene oxide hybrid nanosheets functionalized nanofiltration membrane for desalination, *Desalination* (2019) 209–218. <https://doi.org/10.1016/j.desal.2017.05.012>.
- [76] M. Ikram, A. Raza, M. Imran, A. Ul-Hamid, A. Shahbaz, S. Ali, Hydrothermal Synthesis of Silver Decorated Reduced Graphene Oxide (rGO) Nanoflakes with Effective Photocatalytic Activity for Wastewater Treatment, *Nanoscale Res Lett* 15 (2020). <https://doi.org/10.1186/s11671-020-03323-y>.

- [77] L. Chen, Z. Li, P. Dai, P. Fu, J. Chen, Q. Tang, Effects of carbon addition on microstructure and mechanical properties of Fe₅₀Mn₃₀Co₁₀Cr₁₀ high-entropy alloy prepared by powder metallurgy, *Journal of Materials Research and Technology* 20 (2022) 73–87. <https://doi.org/10.1016/j.jmrt.2022.07.067>.
- [78] T. Cygan, J. Wozniak, M. Kostecki, M. Petrus, A. Jastrzebska, W. Ziemkowska, A. Olszyna, Mechanical properties of graphene oxide reinforced alumina matrix composites, *Ceram Int* 43 (2017) 6180–6186. <https://doi.org/10.1016/j.ceramint.2017.02.015>.
- [79] L. Zhang, M.D. Allendorf, R. Balderas-Xicohtencatl, D.P. Broom, G.S. Fanourgakis, G.E. Froudakis, T. Gennett, K.E. Hurst, S. Ling, C. Milanese, P.A. Parilla, D. Pontiroli, M. Riccò, S. Shulda, V. Stavila, T.A. Steriotis, C.J. Webb, M. Witman, M. Hirscher, Fundamentals of hydrogen storage in nanoporous materials, *Progress in Energy* 4 (2022). <https://doi.org/10.1088/2516-1083/ac8d44>.
- [80] W.A. Shah, X. Luo, Y.Q. Yang, Microstructure, mechanical, and thermal properties of graphene and carbon nanotube-reinforced Al₂O₃ nanocomposites, *Journal of Materials Science: Materials in Electronics* 32 (2021) 13656–13672. <https://doi.org/10.1007/s10854-021-05944-0>.
- [81] A. Centeno, V.G. Rocha, B. Alonso, A. Fernández, C.F. Gutierrez-Gonzalez, R. Torrecillas, A. Zurutuza, Graphene for tough and electroconductive alumina ceramics, *J Eur Ceram Soc* 33 (2013) 3201–3210. <https://doi.org/10.1016/j.jeurceramsoc.2013.07.007>.
- [82] T. Cygan, J. Wozniak, M. Kostecki, M. Petrus, A. Jastrzebska, W. Ziemkowska, A. Olszyna, Mechanical properties of graphene oxide reinforced alumina matrix composites, *Ceram Int* 43 (2017) 6180–6186. <https://doi.org/10.1016/j.ceramint.2017.02.015>.
- [83] M.S.H. Boutilier, N.G. Hadjiconstantinou, R. Karnik, Knudsen Effusion through Polymer-Coated Three-Layer Porous Graphene Membranes, n.d.
- [84] P. Pandey, R.S. Chauhan, Membranes for gas separation, n.d. www.elsevier.com/locate/ppolysci.

- [85] H. Li, Z. Song, X. Zhang, Y. Huang, S. Li, Y. Mao, H.J. Ploehn, Y. Bao, M. Yu, Ultrathin, molecular-sieving graphene oxide membranes for selective hydrogen separation, *Science* (1979) 342 (2013) 95–98.
<https://doi.org/10.1126/science.1236686>.
- [86] J. Zhu, X. Meng, J. Zhao, Y. Jin, N. Yang, S. Zhang, J. Sunarso, S. Liu, Facile hydrogen/nitrogen separation through graphene oxide membranes supported on YSZ ceramic hollow fibers, *J Memb Sci* 535 (2017) 143–150.
<https://doi.org/10.1016/j.memsci.2017.04.032>.
- [87] X. Meng, Y. Fan, J. Zhu, Y. Jin, C. Li, N. Yang, J. Zhao, J. Sunarso, S. Liu, Improving hydrogen permeation and interface property of ceramic-supported graphene oxide membrane via embedding of silicalite-1 zeolite into Al₂O₃ hollow fiber, *Sep Purif Technol* 227 (2019).
<https://doi.org/10.1016/j.seppur.2019.115712>.
- [88] R. Zeynali, K. Ghasemzadeh, A. Iulianelli, A. Basile, Experimental evaluation of graphene oxide/TiO₂-alumina nanocomposite membranes performance for hydrogen separation, *Int J Hydrogen Energy* 45 (2020) 7479–7487.
<https://doi.org/10.1016/j.ijhydene.2019.02.225>.
- [89] F. Zhou, Q. Dong, J.-T. Chen, B. Sengupta, J. Jiang, W.L. Xu, H. Li, S. Li, M. Yu, Printed graphene oxide-based membranes for gas separation and carbon capture, 2021.
- [90] S.R.F.L. Ribeiro, L.P. Bessa, V.L. Cardoso, M.H.M. Reis, Enhanced hydrogen permeance through graphene oxide membrane deposited on asymmetric spinel hollow fiber substrate, *Int J Hydrogen Energy* 47 (2022) 9616–9626.
<https://doi.org/10.1016/j.ijhydene.2022.01.049>.
- [91] N.Q. Long, T.X. Loc, Experimental and modeling study on room-temperature removal of hydrogen sulfide using a low-cost extruded Fe₂O₃-based adsorbent, *Adsorption* 22 (2016) 397–408. <https://doi.org/10.1007/s10450-016-9790-0>.
- [92] H. Tajizadegan, M. Rashidzadeh, M. Jafari, R. Ebrahimi-Kahrizsangi, Novel ZnO-Al₂O₃ composite particles as sorbent for low temperature H₂S removal,

Chinese Chemical Letters 24 (2013) 167–169.

<https://doi.org/10.1016/j.ccllet.2013.01.027>.

- [93] H.W. Liu, S. Feng, A.K. Leung, Effects of nano-activated carbon on water and gas permeability and hydrogen sulphide removal in compacted kaolin, *Appl Clay Sci* 172 (2019) 80–84. <https://doi.org/10.1016/j.clay.2019.02.012>.
- [94] S. Lee, T. Lee, D. Kim, Adsorption of Hydrogen Sulfide from Gas Streams Using the Amorphous Composite of α -FeOOH and Activated Carbon Powder, *Ind Eng Chem Res* 56 (2017) 3116–3122. <https://doi.org/10.1021/acs.iecr.6b04747>.





This material is reserved for educational use only, not allowed for commercial use.

Forbidden to modify the content, and cite the document when use.



Research Article

Hydrogen Sulfide Adsorption on Alumina/Graphene Oxide Composites at Ambient Temperature

Montree Hankoy [a], Mettaya Kitiwan*[a,b,c], Chaiwat Phrompet [a,c], Chesta Ruttanapun [a,c], Prangtip Rittichote Kaewpengkrow [d], Supawan Vichaphund [e], Duangduen Atong [e] and Phacharaphon Tunthawiroon [b,c,f]

- [a] Department of Physics, School of Science, King Mongkut's Institute of Technology Ladkrabang, Bangkok 10520, Thailand
 [b] Devices and Systems for Energy and Environment Research Unit, School of Science, King Mongkut's Institute of Technology Ladkrabang, Bangkok 10520, Thailand
 [c] Center of Excellence in Smart Materials Research and Innovation, King Mongkut's Institute of Technology Ladkrabang, Bangkok 10520, Thailand
 [d] Rattanakosin College for Sustainable Energy and Environment (RCSEE), Rajamangala University of Technology Rattanakosin, 96 Moo 3 Phutthamonthon Sai 5 Rd., Salaya, Phutthamonthon, Nakhon Pathom, 73170, Thailand
 [e] National Metal and Materials Technology Center (MTEC), National Science and Technology Development Agency (NSTDA), Thailand Science Park, Pathum Thani, 12120, Thailand
 [f] Department of Industrial Engineering, School of Engineering, King Mongkut's Institute of Technology Ladkrabang, Bangkok 10520, Thailand

*Author for correspondence; e-mail: mettaya.ki@kmitl.ac.th

Received: 13 May 2022

Revised: 16 September 2022

Accepted: 21 September 2022

ABSTRACT

Hydrogen sulfide (H_2S) is one of the most common pollutants found in natural gas and industrial waste. Over the few decades, the removal of H_2S has become a significant problem. In the field of a clean environment such as water purification and toxic gas removal, graphene oxide (GO) has been found to have advantages. In this study, the influence of GO on alumina (Al_2O_3) as an adsorbent of H_2S was examined. A series of Al_2O_3/GO (AGO) composites with varying graphene oxide addition (0.5–3.0 wt%) were prepared using the high-temperature sintering method. The X-ray diffraction patterns indicate the primary phase of Al_2O_3 with hexagonal crystal structure for all AGO composites. Raman spectrometry measurements confirmed that the GO particles were incorporated in AGO composites. The TEM image indicated that GO nanosheets were embedded between Al_2O_3 grains. The efficiency of AGO adsorbent at ambient temperature was investigated and compared with the pristine Al_2O_3 adsorbent. The AGO composites adsorbent demonstrated the H_2S breakthrough capacity in the range of 0.07–0.43 mg/g, which is higher than that of pristine Al_2O_3 (0.06 mg/g). Furthermore, the highest H_2S breakthrough capacity of 0.43 mg/g was obtained from AGO containing 3.0 wt% GO. This investigation demonstrates that the AGO adsorbent fabricated using a simple method has the potential to be used for H_2S removal at ambient temperature.

Keywords: hydrogen sulfide, graphene oxide, alumina, sintering, adsorbent

1. INTRODUCTION

Recently, many industrial processes produce substantial amounts of hydrogen sulfide (H_2S). H_2S is a colorless gas with a distinct rotten egg odor, which can be detected even at a low concentration by smelling [1–2]. Inhalation of H_2S in high amounts can rapidly paralyze a human nerve, impair the respiratory system, make breathing difficult, and cause death. In industrial operation, the equipments exposed to H_2S are also damaged from corrosion [3–5]. In addition, H_2S emissions into the atmosphere contaminate the ecosystem and alter the ecological equilibrium [6]. For these reasons, H_2S should be removed from the system before being released into the environment.

Several technological approaches have been developed to efficiently eliminate H_2S , including hydrodesulfurization, scrubbing, catalytic oxidation, adsorption and biological process and treatment [7–9]. Among different methods, adsorption processes have attracted a lot of attention in the removal of H_2S since they are relatively low-cost, environmentally friendly, and easy to use at an ambient temperature. Many researchers have focused on the study of improved functioning solid sorbent materials. The well-known materials for the removal of H_2S such as zinc oxide (ZnO) [10], metal-organic frameworks (MOFs) [11], zeolites [12], metal oxide [13], and carbon-based materials [12–13] are remarkable candidates for desulfurization adsorbents. Carbon-based material is one of the most interesting adsorbent materials due to its highly porous structure, high stability, good adsorption capacity, and large internal surface area [14–17].

The effects of carbon addition in adsorbents on the H_2S removal have been studied extensively. Liu et al. [18] investigated the influence of the nano-activated carbon/kaolin composites on H_2S removal and discovered that the addition of activated carbon to the composites improved the adsorption capacity when compared to pure kaolin. Abbasabadi et al. [19] reported that a novel method

for H_2S removal using amido-functionalized reduced graphene oxide (AFRGO) exhibited higher H_2S adsorption capacity. According to Barkovskii et al. [20], carbon materials were treated with a NaOH solution, and the results demonstrated that their sorption capacity for H_2S was enhanced. The H_2S adsorbents were usually prepared and employed as powders to provide a high surface area and adsorption capacity. However, the adsorbent powder is associated with a lower gas flow rate. In this regard, the porous pellet adsorbents offer a high surface area as well as good mechanical properties and ease of usage could be able to alleviate this problem. For example, Zhao et al. [21] developed a mixed metal oxide-based sorbent with pellet-shaping that had a high sulfur capacity and excellent reusability for the removal of H_2S .

H_2S has been eliminated from gas streams using various carbon-based adsorbents. These adsorbents include activated carbon, coal, and reduced graphene oxide (rGO). However, GO which is a novel material was rarely investigated on its performance of adsorbed H_2S . Most carbon-based adsorbents for the H_2S removal were the powder-type adsorbent and the production processes were complicated. Furthermore, powder sorbents are limited in some applications since they restrict the gas flow in the system. Therefore, this research aims to fabricate pellets-shape sorbent based on alumina/graphene oxide (AGO) composites with different loadings of GO using a high-temperature sintering technique. The characterization of the phase composition, microstructure, porous characteristics, and specific surface area of AGO sorbent composites were examined. Additionally, the influence of GO contents in AGO on the H_2S breakthrough capacity was conducted. Each characterization study was compared with pristine Al_2O_3 as reference material. The functionalization and mechanism of AGO composites on the H_2S adsorption was discussed.

2. MATERIALS AND METHODS

2.1 Materials

The starting powders are commercial α - Al_2O_3 powder (Nippon Light Metal, Japan) with a purity of 99.9% and an average size of 1 μm and the MgO powder (Fujifilm Wako Chemical, Japan) with a purity of 99.9% and an average size of 0.2 μm . GO was prepared by a modified Hummer's method through the Center of Excellence in Smart Materials Research and Innovation, King Mongkut's Institute of Technology Ladkrabang,

as previously reported by Phrompet et al. [22] using the commercial graphite with a purity of 99.9% (Sigma-Aldrich, USA).

2.2 Preparation of the AGO sorbents

Figure 1 illustrates the schematic of AGO composites preparation. First, the mixture of Al_2O_3 , MgO, and GO with different content, i.e., 0.5, 1.0, 1.5, 2.0, 2.5, and 3.0 wt% GO, were transferred to a ball milling with an ethanal solution and alumina ball with size 3 mm, the

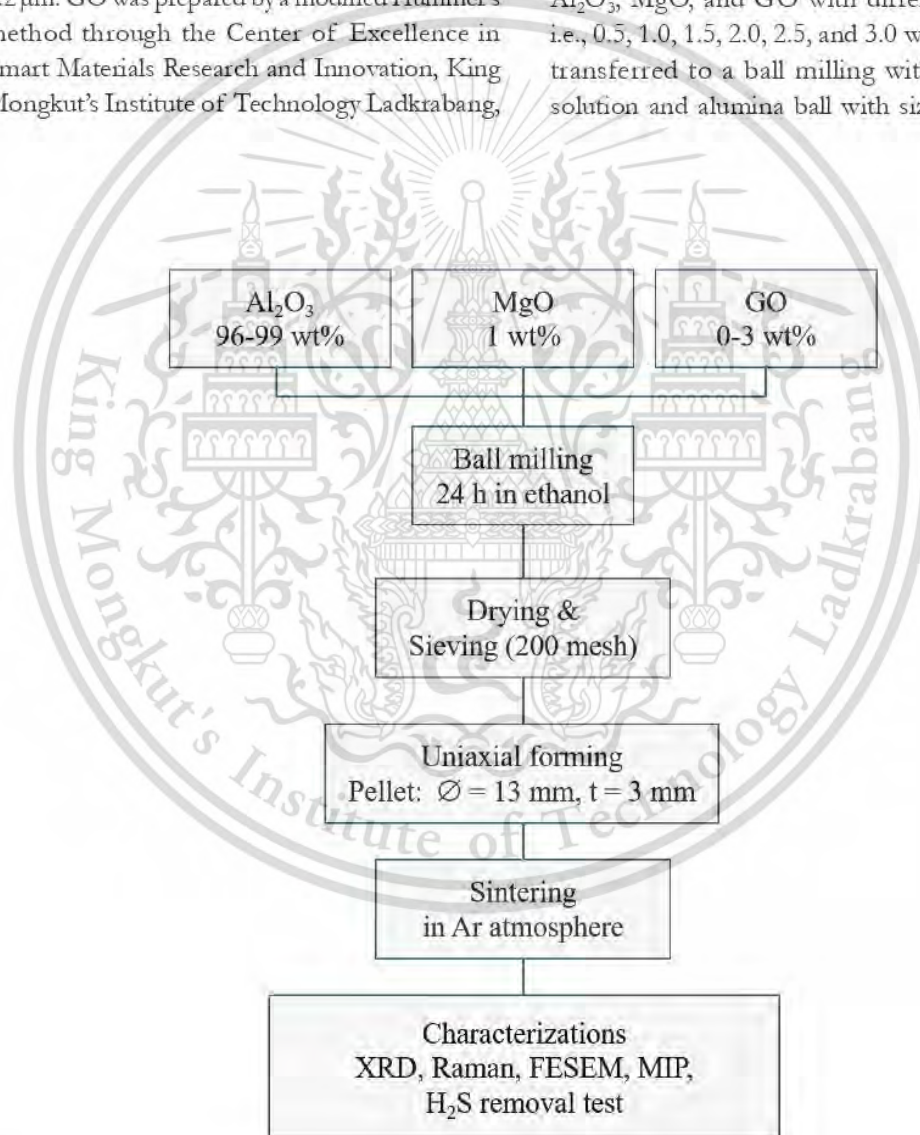


Figure 1. Schematic of alumina/graphene oxide (AGO) composites preparation.

milling speed was 300 rpm for 24 h to produce the slurry. Next, the slurry was dried at 120°C for 24 h and then sieved using 200 mesh to obtain the homogeneous mixture. The sieved powder was compacted under a uniaxial pressure of 24 MPa to obtain a disk shape specimen with a diameter of 13 mm. After that, the AGO disk was sintered at 1500°C under an argon atmosphere with a heating rate of 5°C/min and a holding time of 2 h. Figure 2 presents the pellets of pristine Al_2O_3 and AGO composites with the different GO content after sintering.

2.3 Characterizations

The crystalline phases of AGO sorbents sintered specimen were examined using an X-ray diffractometer (XRD; Rigaku Miniflex 600, Japan) with $\text{CuK}\alpha$ radiation ($\lambda = 1.5406 \text{ nm}$). The operated XRD patterns for each specimen were shown in the 2θ range of 5° – 80° using a scanning rate of $0.02^\circ/\text{s}$. The ICDD standard files were employed to compare with the XRD results. Raman spectra

analysis was conducted using a Raman spectrometer (DXR Smart Raman, Thermo Foshier Scientific, USA) at a 532 nm laser excitation wavelength. The microstructure of composite was examined using the and Field emission scanning electron microscope (FESEM, Apreo S-Thermo Fisher Scientific, USA). Furthermore, the average grain size of the specimen was estimated from FESEM micrograph by the mean linear intercept method using ImageJ software. The morphologies of GO and AGO composites were investigated using Transmission electron microscopy (TEM, JEOL-JME-2100 plus, Japan) equipped with Energy dispersive X-ray spectroscopy (EDX). The specific surface area and average pore diameter of the sorbent were measured using mercury intrusion porosimetry method (MIP, AutoPore V 9600, ATS Scientific Inc, Canada). For MIP measurement, the sorbent composite was polished to a square specimen with an area of approximately $10 \text{ mm} \times 10 \text{ mm}$.



Figure 2. The appearance of pristine Al_2O_3 and AGO composites sintered at 1500°C.

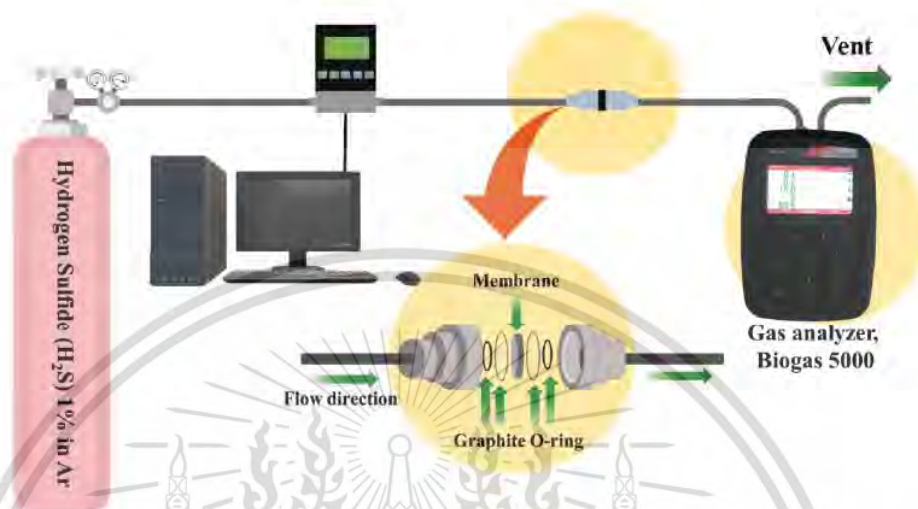


Figure 3. Schematic of hydrogen sulfide (H₂S) adsorption experiment setup.

2.4 Adsorption Experiments

The H₂S adsorption experiment was investigated using a fixed housing at room temperature. Figure 3 displays the H₂S adsorption experiment setup. The pellet of AGO sorbents with a thickness of 3 mm was packed into the housing. After that, H₂S (composition: 1% or 10000 ppm H₂S; balanced with Ar) was released into the reactor with a flow rate of 10 mL/min. The gas analyzer (Geotech; Biogas 5000) was used to detect the H₂S outlet gas from the reactor. In addition, the duration of the experiment was defined as H₂S breakthrough time, and it was also employed to evaluate the H₂S breakthrough capacity of the produced AGO. The adsorption capacity of the AGO sorbent was estimated by the following equation [23]:

$$\text{Ads}_{\text{Cap}} = \frac{t_b \cdot \text{FR} \cdot C_{\text{in}}}{V_{\text{mol}} \cdot W} \quad (1)$$

where t_b is the breakthrough time (min), FR is the total flow rate (ml/min), C_{in} is the inlet

concentration of H₂S, V_{mol} is the molar volume (22.4 ml/mol), and W is the weight of sorbents materials (g). The tests were repeated three times for each specimen to get the reliability data, then the average value was reported.

3. RESULTS AND DISCUSSION

Figure 4 demonstrates the XRD patterns of GO starting powder, pristine Al₂O₃ and AGO composites. The results show that all the diffraction of pristine Al₂O₃ and AGO composites are located at 2θ of 25.62°, 35.22°, 37.47°, 43.43°, 52.65°, 57.62°, 61.44°, 66.64°, 68.33°, and 77.06° that can be assigned to (012), (104), (110), (113), (024), (116), (018), (214), (300), and (1010), respectively. This indicates the single crystal phase of hexagonal Al₂O₃ (ICDD no. 01-073-1123) in the AGO composites. For GO starting powder, the X-ray intense characteristic diffraction peak of GO was observed at 2θ of 10.83°, which corresponds to the (002) plane. The interlayer spacing (d) of the GO starting powder was calculated using

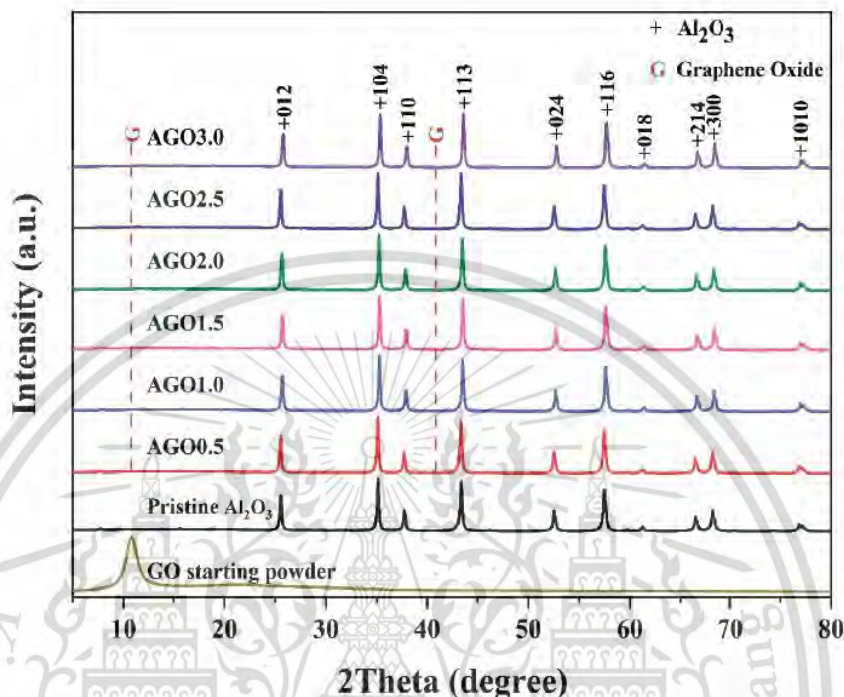


Figure 4. The X-ray diffraction (XRD) patterns of GO starting powder, pristine Al_2O_3 and AGO composites.

Bragg's law, indicating that the interlayer spacing d_{002} of GO value was approximately 0.816 nm. However, the GO characteristic peak was not found for all AGO specimens, suggesting that the strong intensity of the Al_2O_3 hinders the low concentration phase of GO, as reported by an earlier studies [22–23]. According to the literature, the position of GO peak should be discovered at 2θ of -10.9° , -43.0° [26–29] as indicated by the G and dash line in Figure 4.

Figure 5 shows the Raman spectrum of GO starting powder and AGO composites with varying GO addition. The two characteristic peaks in accord with the G and D band of graphene were clearly observed. The G band corresponds to the E_{2g} phonon of the sp^2 carbon atom, while the D band originates from a breathing mode of π -point phonon with A_{1g} symmetry [27–28]. The present

study demonstrated that the G band at 1580 cm^{-1} , D band at 1348 cm^{-1} , and 2D band at 2681 cm^{-1} conform with the results of the other literature [29–30]. The intensity ratio between the D band and G band (I_D/I_G) can be employed to quantify the defect structure of graphene. The I_D/I_G ratios of AGO composites were 0.94, 0.97, 0.99, 1.00, 1.02, and 1.03 for AGO0.5, AGO1.0, AGO1.5, AGO2.0, AGO2.5, and AGO3.0, respectively. The Raman result can thus infer that the AGO composite material consists of GO, which was not found in the XRD results

Figure 6 depicts the TEM image of GO starting materials. The as-received GO displays a stacking of nano layers structure. The transparent area indicated the few layers of GO nanosheets. The darker area indicated the extensive stacking of GO exfoliation since the functional group

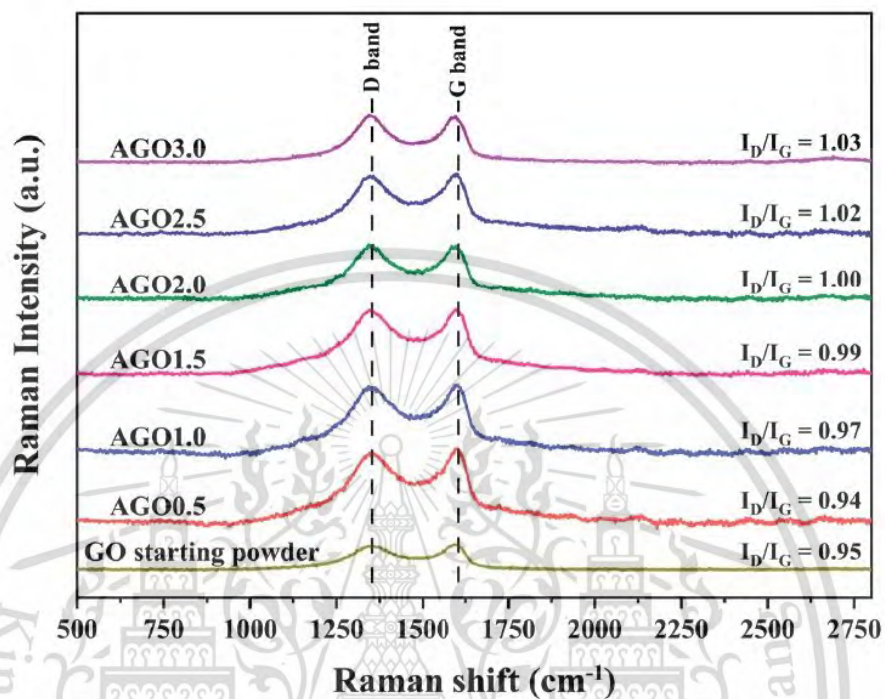


Figure 5. Raman spectra of GO starting powder and AGO composites.

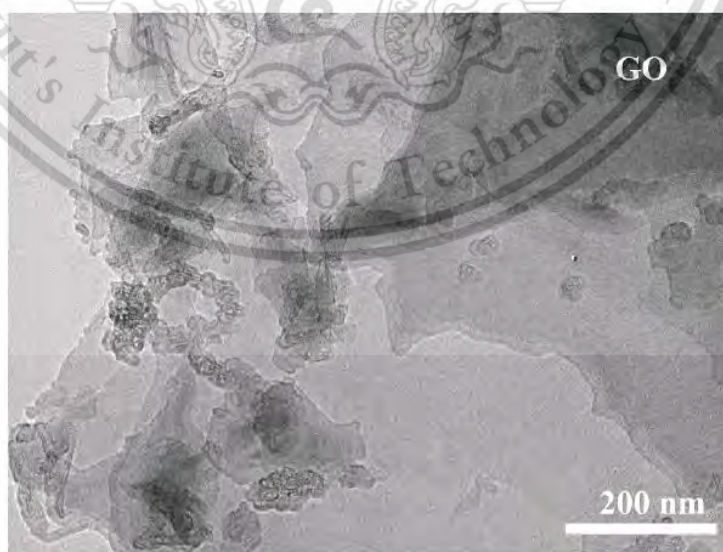


Figure 6. TEM image of GO starting material.

This material is reserved for educational use only, not allowed for commercial use.

Forbidden to modify the content, and cite the document when use.

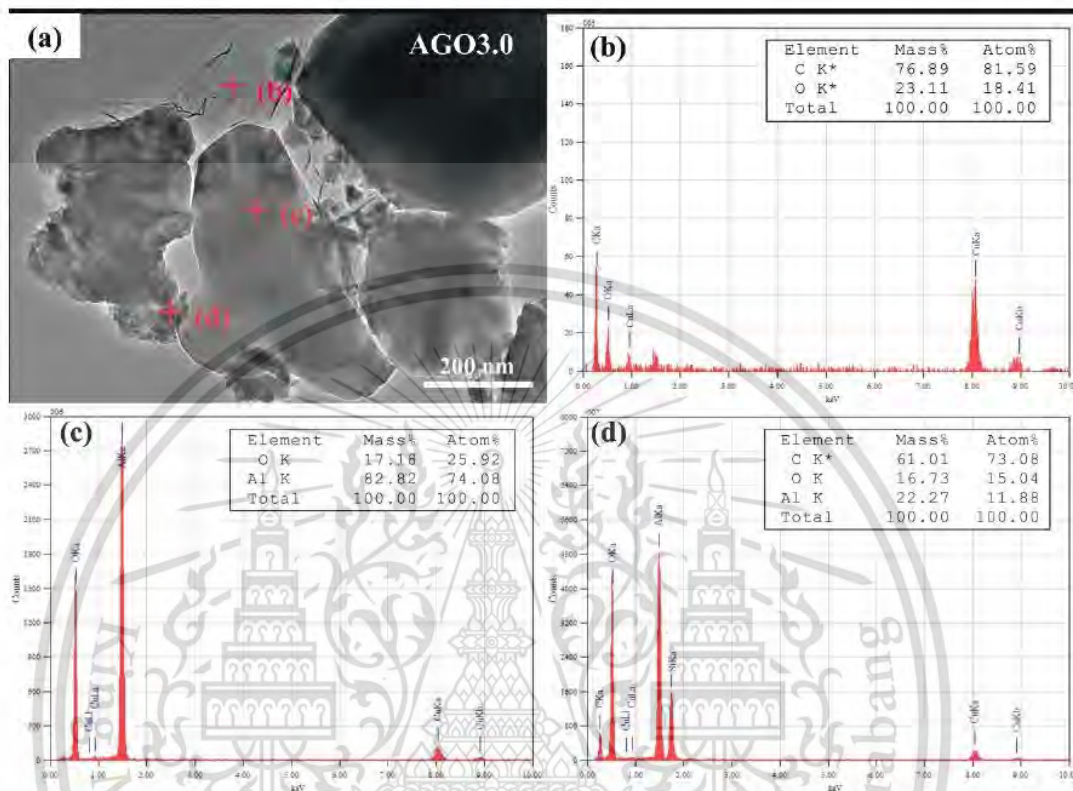


Figure 7. TEM image of AGO3.0 composite (a) and EDX spectra of points (b), (c), and (d).

and electrostatic interaction of oxygen caused the GO sheets to have an additional thickness [34]. Figure 7 shows the TEM image of AGO3.0 composite and the EDX spectra analysis. It was observed that GO are distributed between the grains of Al_2O_3 grains. According to the point analysis spectra, the thin layer at point (b) contains C and O, indicating the composition of GO. On the other hand, the analysis on the large grain at point (c) reveals that this area is enriched in Al and O, suggesting the composition of Al_2O_3 . Additionally, the region between the large grain at point (c) discovers the C, Al, and O elements, which confirmed that the GO were embedded at Al_2O_3 grain boundary. It should be noted that the Cu peaks originate from the TEM grid and the Si peaks originate from silicon escape peak.

Figure 8 depicts the FESEM micrograph of the surface of the sorbent materials. The pristine Al_2O_3 specimen had a coarse surface and irregular shape grain implying the poor sinterability. On the other hand, the AGO composites demonstrated uniform microstructure with an almost round shape grain and clearly visible grain boundary when compared to pristine Al_2O_3 . Figure 9 depicts the average grain size of AGO composites as a function of GO content. The average grain size of AGO specimen was larger than that of pristine Al_2O_3 since GO promoted the sintering of Al_2O_3 particles and resulted in grain growth. The maximum grain size was $1.22 \mu\text{m}$ at 1.0 wt% GO. However, the continued addition of the GO resulted in the grain size being slightly reduced to $1.07 \mu\text{m}$ at 3.0 wt% GO. The reason might be

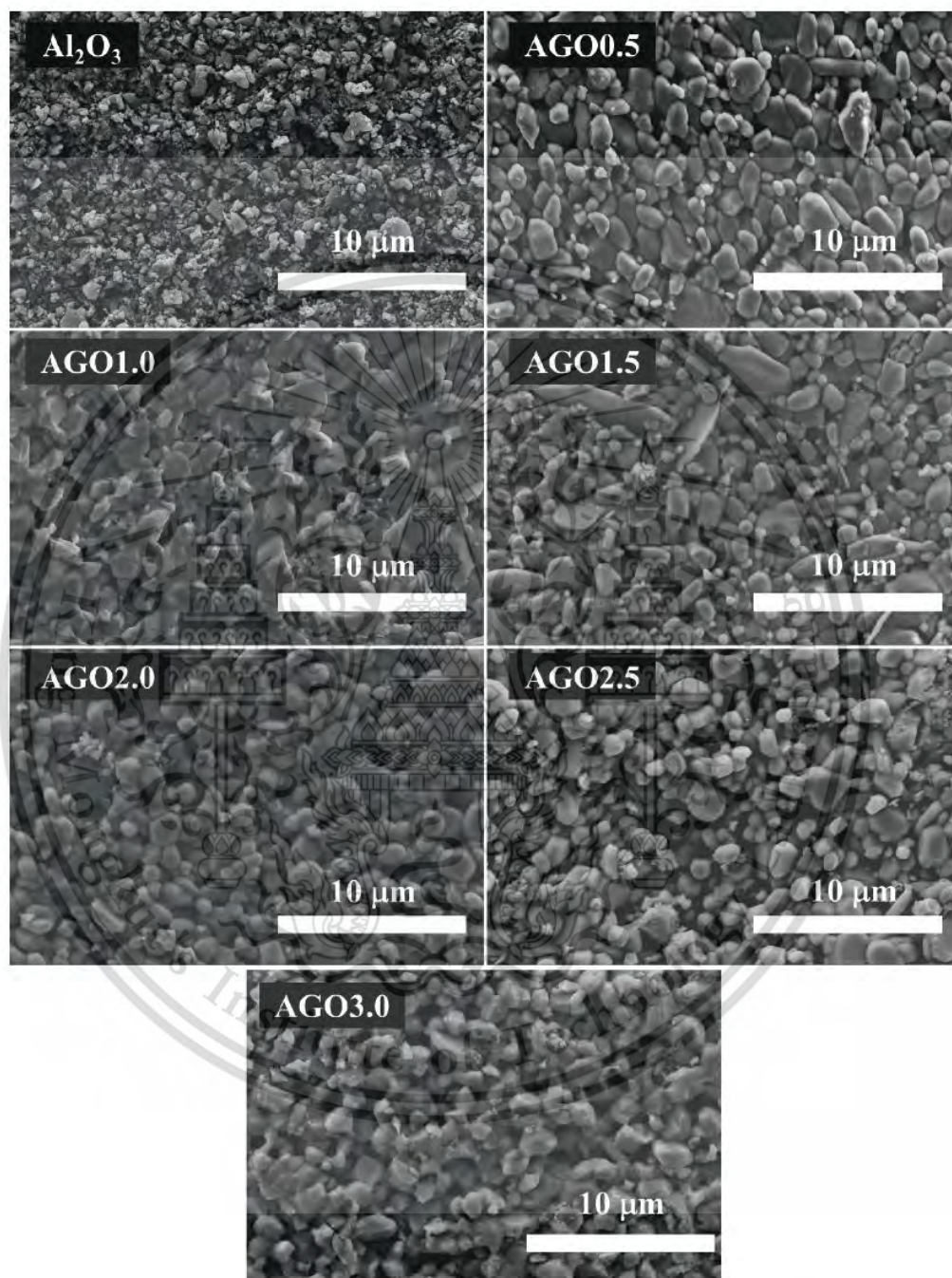


Figure 8. Field emission scanning electron microscope (FESEM) micrographs of AGO sorbent.

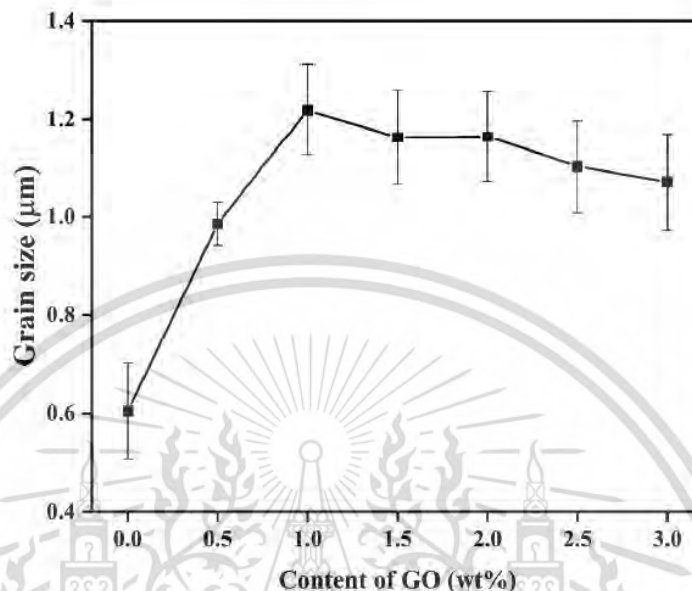


Figure 9. The average grain size of AGO composites as a function of GO content.

due to, at a higher amount of GO addition, the presence of GO at the grain boundary of Al_2O_3 could inhibit the grain growth [35].

It was also noticed that the surface morphology of AGO sorbents revealed several open pores. Thus, the specific surface area and average pore diameter of the sorbents were examined using MIP. In Figure 10(a), the highest specific surface area of $4.74 \text{ m}^2/\text{g}$ was observed for pristine Al_2O_3 due to a poor densification and porous microstructure, while the specific area of AGO composite demonstrated a lower value. However, the specific surface area of AGO sorbents was likely to increase as the function of GO content, which were 0.77, 0.66, 0.89, 0.99, 1.43, and $1.82 \text{ m}^2/\text{g}$ for AGO0.5, AGO1.0, AGO1.5, AGO2.0, AGO2.5, and AGO3.0, respectively. The average pore diameter showed a similar trend with the specific surface area as can be observed in Figure 10(b). The average pore diameter of pristine Al_2O_3 was $0.15 \mu\text{m}$, while those of AGO

composites tended to increase from $0.09 \mu\text{m}$ to $0.24 \mu\text{m}$ with an increase in GO content from 0.5 wt% to 3.0 wt%.

AGO composite sorbents were investigated for the H_2S adsorption and compared to pristine Al_2O_3 sorbents. Figure 11 shows the breakthrough curves for analyzing the dynamic adsorption behavior of AGO sorbents. The H_2S concentration at the reactor outlet was measured as a function of time, while operating at ambient temperature. Regardless of the GO content initially no H_2S was discharged until a specified point in time (described as H_2S breakthrough time), when the concentration of the H_2S increased suddenly and then continues steadiness. The area above the breakthrough curve of each adsorbent material in Figure 9 was integrated, then the total concentration of H_2S gas released was calculated to the H_2S breakthrough capacity [36]. Thus, the H_2S breakthrough capacity was obtained and shown in Figure 12. First, the H_2S breakthrough

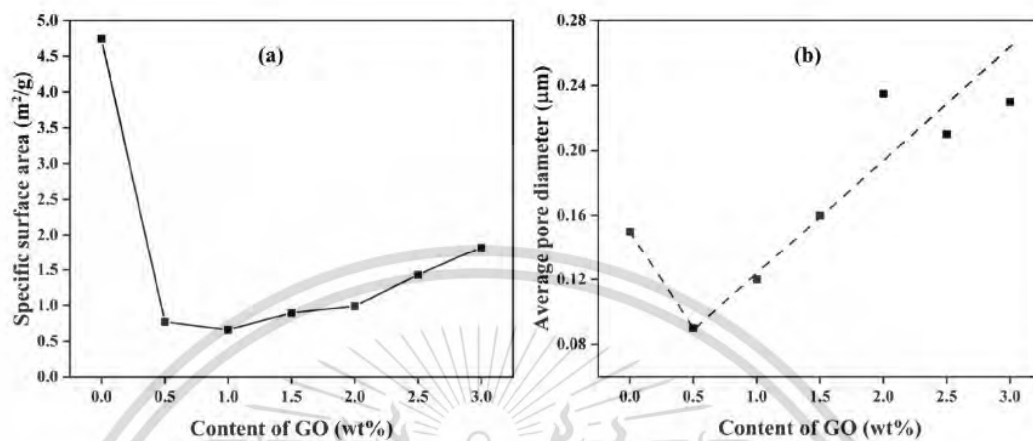


Figure 10. The effects of GO content on (a) specific surface area and (b) average pore diameter of AGO composites.

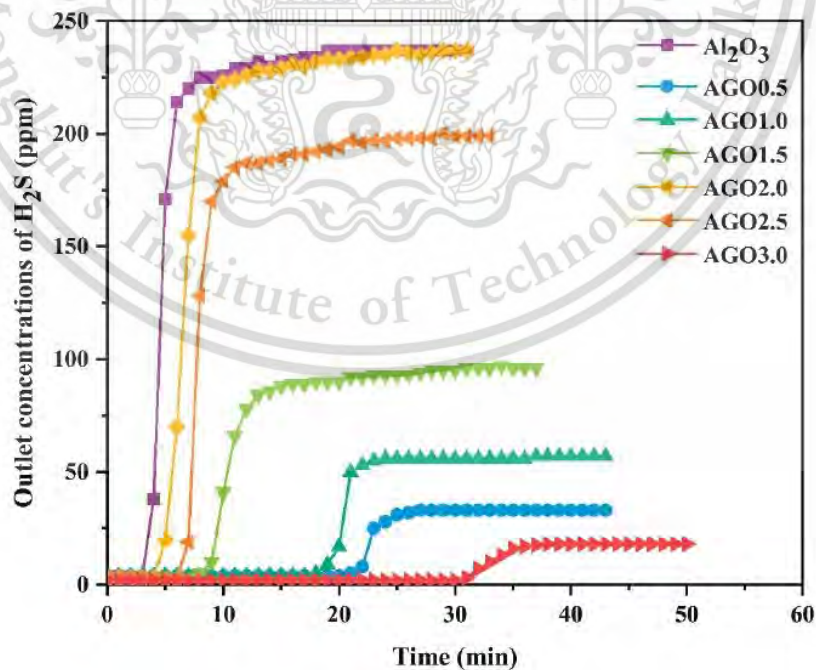


Figure 11. Effects of GO content on H_2S breakthrough of AGO sorbent.

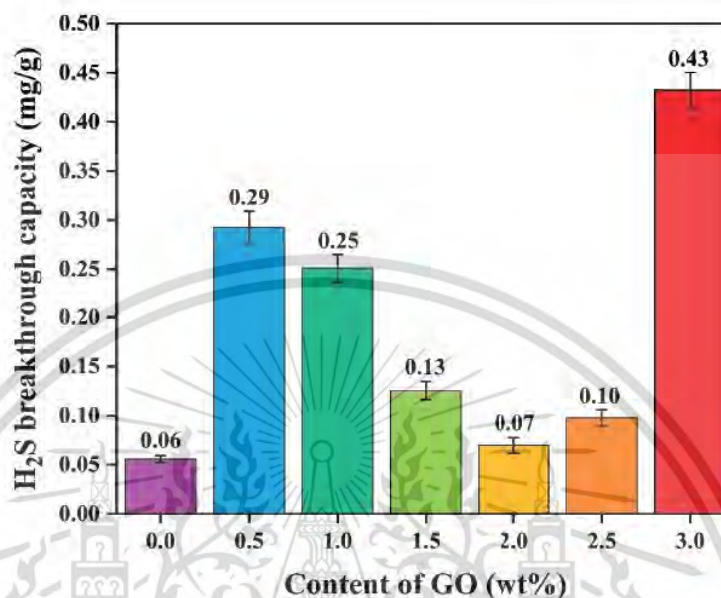


Figure 12. Effects of GO content on H₂S breakthrough capacity.

capacity of AGO sorbent composites increased to 0.29 mg/g with the addition of 0.5 wt% of GO. Then, adding the GO of > 0.5 wt% led to a decrease in breakthrough capacity, and the lowest capacity was 0.07 mg/g with 2.0 wt% of GO. After that, the breakthrough capacity began to increase, and the highest capacity was 0.43 mg/g with 3.0 wt% of GO content.

According to the data presented in Figure 12, in terms of their ability to remove H₂S at ambient temperature, the sorbents are rated as follows: AGO3.0 > AGO0.5 > AGO1.0 > AGO1.5 > AGO2.5 > AGO2.0 > pristine Al₂O₃. The six novel GO-based sorbents presented in this research demonstrated better performance than that of pristine Al₂O₃ sorbent suggesting the ability of GO in the removal of H₂S. Generally, the breakthrough capacity should be related to the surface area of sorbents but the breakthrough capacity of AGO did not have a trend with increasing surface area. In this study, the breakthrough capacity of AGO

adsorbent was believed to influence by both GO content and pore structure. When considering the average pore diameter, the H₂S adsorption capacity tended to decrease as the average pore diameter increased. It was assumed that the small pore size of adsorbent led to a lower flow rate of H₂S gas, then GO could react with H₂S effectively. As can be seen that AGO0.5 has the lowest average pore diameter (0.09 μm) giving the high H₂S adsorption capacity. On the other hands, AGO1.0 to AGO2.0 exhibited an increase in pore size (in the range of 0.12–0.23 μm), which might enable the rapid transport of H₂S gas through the adsorbent and thus reduced the adsorption ability of GO. However, AGO3.0 demonstrates the highest breakthrough capacity despite the large pore size (0.23 μm), which implied that the high GO content at 3 wt% might be the adequate amount that enhanced the reaction of AGO sorbent with H₂S. Figure 13 illustrates the schematic representation of one feasible mechanism of AGO composite

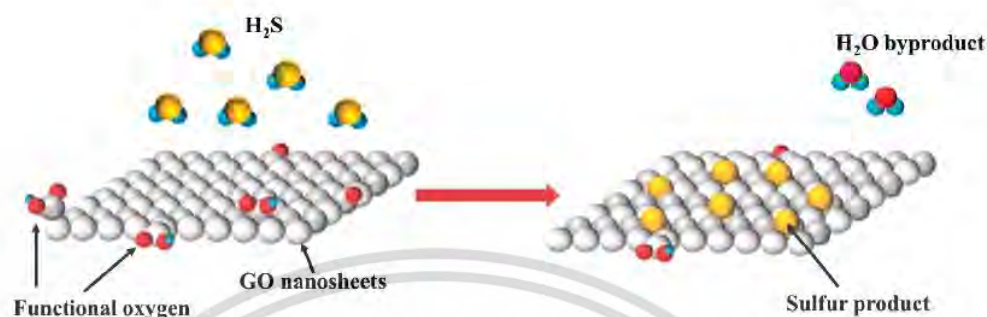


Figure 13. Schematic representation of one feasible mechanism of AGO composite for H_2S removal.

Table 1. The breakthrough time and H_2S breakthrough capacity compared to literature.

Type of adsorbent	Flow rate (ml/min)	Breakthrough time (min)	H_2S breakthrough Capacity (mg/g)	References
Fe_2O_3 -based	50	458	17.4	[13]
ZnO	150	76	28	[10]
ZnO- Al_2O_3	150	140	52	[10]
Kaolin/6wt%AC	50	420	0.17	[18]
α -FeOOH/AC30wt%	300	-	0.48	[38]
AGO3.0	10	31	0.43	This study

for removal H_2S . When the GO nanosheets in Al_2O_3 are exposed to an atmosphere containing H_2S , the functional oxygen in GO might cause the reduction of H_2S molecule and produced sulfur which is then captured at oxygen vacancy site on the GO surface. The reduced hydrogen from H_2S is subsequently interacted with oxygen from GO to form a H_2O molecule as a byproduct [37].

Table 1 provides the H_2S breakthrough capacity compared to the literature. From the literature, it can be seen that the H_2S breakthrough capacity performance of AGO3.0 is lower than that of the metal oxides such as iron oxide (FeO) [13] and zinc oxide (ZnO) [10]. However, compared to Kaolin/AC6% [18], AGO3.0 showed better performance and has comparable performance to

α -FeOOH/AC30wt% [38]. In this research, the highest H_2S adsorption capacity was observed for AGO with 3 wt% GO. The further increase in the GO content possible results in an increase in H_2S adsorption capacity. It should also be noted that the GO synthesis in a college laboratory provides an economical and efficient sorbent for H_2S adsorption at ambient temperatures.

4. CONCLUSIONS

A series of GO-modified Al_2O_3 (AGO) adsorbent pellets were fabricated using the high-temperature sintering method at $1500^\circ C$ for 2 h in ab argon atmosphere. The XRD patterns of the AGO sorbent composites demonstrated the single phase of the hexagonal crystal structure of

Al₂O₃. The characteristics of D band and G band of the GO and AGO composites were observed by Raman spectroscopy. TEM analysis revealed that the GO nanosheets were existed at the grain boundary of Al₂O₃. The specific surface area and average pore size of AGO composites were found to increase with an increase in GO content. The H₂S breakthrough experiment demonstrated that the AGO adsorbents could improve the H₂S adsorption capacity. The adsorption capacities of H₂S of all AGO sorbents were higher than that of pristine Al₂O₃ sorbent. The highest adsorption capacity of 0.43 mg/g was achieved from AGO3.0. The AGO composites produced using the easy method showed a potential to be developed as adsorbents for the elimination of H₂S at ambient temperature.

ACKNOWLEDGEMENTS

This study was financially supported by the National Research Council of Thailand (NRCT); grant number 400/2563). Montree Hankoy would like to thank Thailand Graduate Institute of Science and Technology (TGIST), National Science and Technology Development Agency (NSTDA) for his Ph.D. scholarship [Grant Number SCA-CO-2563-12077-TH]. Grateful to Prof. Vissanu Meeyoo (Mahanakorn University of Technology, MUT) for their continued facility and other technical assistance with the H₂S adsorption experiment.

CONFLICT OF INTEREST STATEMENT

The authors declare no conflict of interest.

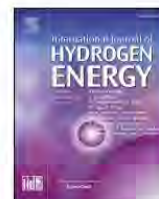
REFERENCES

- [1] Shah M.S., Tsapatsis M. and Siepmann J.I., *Chem. Rev.*, 2017; **117(14)**: 9755–9803. DOI 10.1021/acs.chemrev.7b00095.
- [2] Geng Q., Wang L.J., Yang C., Zhang H.Y., Zhao Y.R., Fan H.L., et al., *Fuel Process. Technol.*, 2019; **185**: 26–37. DOI 10.1016/j.fuproc.2018.11.013.
- [3] Avelino A.F., Araújo W.S., Dias D.F., dos Santos L.P.M., Correia A.N. and de Lima-Neto P., *Electrochim. Acta*, 2018; **286**: 339–349. DOI 10.1016/j.electacta.2018.08.042.
- [4] Zheng Y., Brown B. and Nešić S., *Corrosion*, 2014; **70(4)**: 351–365. DOI 10.5006/0937.
- [5] Choi Y.S., Nesić S. and Ling S., *Electrochim. Acta*, 2011; **56(4)**: 1752–1760. DOI 10.1016/j.electacta.2010.08.049.
- [6] Gupta A.K., Ibrahim S. and Al Shoaibi A., *Prog. Energ. Combust.*, 2016; **54**: 65–92. DOI 10.1016/j.peccs.2015.11.001.
- [7] Jirachaisakdeacha D., Kumdhithahutsawakul L., Pholchan P., Kantha U., Pathom-aree W. and Bovonsombut S., *Chiang Mai J. Sci.*, 2020; **47**: 872–886.
- [8] Vellingiri K., Deep A. and Kim K.H., *ACS Appl. Mater. Interf.*, 2016; **8(44)**: 29835–29857. DOI 10.1021/acsami.6b10482.
- [9] Kamchompoo S., Mudchimo T., Wongnongwa Y., Kunaseth M. and Jungsuttiwong S., *Chiang Mai J. Sci.*, 2020; **47**: 195–206.
- [10] Tajizadegan H., Rashidzadeh M. and Jafari M., *Chinese Chem. Lett.*, 2013; **24(2)**: 167–169. DOI 10.1016/j.ccllet.2013.01.027.
- [11] Joshi J.N., Zhu G., Lee J.J., Carter E.A., Jones C.W., Lively R.P., et al., *Langmuir*, 2018; **34(29)**: 8443–8450. DOI 10.1021/acs.langmuir.8b00889.
- [12] Liu X. and Wang R., *J. Hazard. Mater.*, 2017; **326**: 157–164. DOI 10.1016/j.jhazmat.2016.12.030.
- [13] Long N.Q. and Loc T.X., *Adsorption*, 2016; **22(3)**: 397–408. DOI 10.1007/s10450-016-9790-0.
- [14] Qi J., Wei G., Li Y., Li J., Sun X., Shen J., et al., *Chem. Eng. J.*, 2018; **339**: 499–508. DOI 10.1016/j.cej.2018.01.157.
- [15] Yang C., Wang J., Fan H., Hu Y., Shen J., Shangguan J., et al., *Energ. Fuel*, 2018; **32(5)**: 6064–6072. DOI 10.1021/acs.energyfuels.8b00532.
- [16] Chen Y., Ma C., Wu Y., Ke C., Liu X., Wang J., et al., *Micropor. Mesopor. Mat.*, 2022; **333**: 111712. DOI 10.1016/j.micromeso.2022.111712.

- [17] Sitthikhankaew R., Chadwick D., Assabumrungrat S. and Laosiripojana N., *Chem. Eng. Commun.*, 2014; **201(2)**: 257–271. DOI 10.1080/00986445.2013.767799.
- [18] Liu H.W., Feng S. and Leung A.K., *Appl. Clay Sci.*, 2019; **172**: 80–84. DOI 10.1016/j.clay.2019.02.012.
- [19] Khaleghi A.M., Rashidi A., Safaei-Ghomi J., Khodabakhshi S. and Rahighi R., *J. Sulfur Chem.*, 2015; **36(6)**: 660–671. DOI 10.1080/17415993.2015.1079711.
- [20] Barkovskii I.E., Lysikov A.I., Veselovskaya J.V., Maltseva N.V. and Okunev A.G., *Catal. Ind.*, 2019; **11(4)**: 335–341. DOI 10.1134/S2070050419040020.
- [21] Zhao W., Manno M., Al Wahedi Y., Tsapatsis M. and Stein A., *Ind. Eng. Chem. Res.*, 2021; **60(50)**: 18443–18451. DOI 10.1021/acs.iecr.1c03738.
- [22] Phrompet C., Sriwong C. and Ruttanapun C., *Compos. Part B-Eng.*, 2019; **175**: 107128. DOI 10.1016/j.compositesb.2019.107128.
- [23] Janetaisong P., Lailuck V. and Supasitmongkol S., *Key Eng. Mater.*, 2017; **751**: 449–454. DOI 10.4028/www.scientific.net/KEM.751.449.
- [24] Smirnov A., Peretyagin P., Pinargote N.W.S., Gershman I. and Bartolomé J.F., *Nanomaterials*, 2019; **9(2)**: 1–10. DOI 10.3390/nano9020151.
- [25] Duntu S.H., Tetteh F., Ahmad I., Islam M. and Boakye-Yiadom S., *Ceram. Int.*, 2021; **47(1)**: 367–380. DOI 10.1016/j.ceramint.2020.08.142.
- [26] Yuan W., Li B. and Li L., *Appl. Surf. Sci.*, 2011; **257(23)**: 10183–10187. DOI 10.1016/j.apsusc.2011.07.015.
- [27] Justh N., Berke B., László K., Bakos P.L., Szabó A., Hernádi K., et al., *Appl. Surf. Sci.*, 2018; **453**: 245–251. DOI 10.1016/j.apsusc.2018.05.064.
- [28] Taherialekhouhi R., Rasouli S. and Khosravi A., *Int. J. Heat Mass Tran.*, 2019; **145**: 118751. DOI 10.1016/j.ijheatmasstransfer.2019.118751.
- [29] Wang H., Zhao W., Chen Y., Yang X., Li Y. and Meng X., *Chiang Mai J. Sci.*, 2021; **48**: 506–519.
- [30] Zhu C., Guo S., Fang Y. and Dong S., *ACS Nano*, 2010; **4(4)**: 2429–2437. DOI 10.1021/nn1002387
- [31] Hsu K.C. and Chen D.H., *Nanoscale Res. Lett.*, 2014; **9(1)**: 484. DOI 10.1186/1556-276X-9-484
- [32] Shen J., Hu Y., Shi M., Lu X., Qin C., Li C., et al., *Chem. Mater.*, 2009; **21**: 3514–3520. DOI 10.1021/cm901247t.
- [33] Rashad M., Pan F., Yu Z. and Asif M., *Prog. Nat. Sci.-Mater.*, 2015; **25**: 460–470. DOI 10.1016/j.pnsc.2015.09.005
- [34] Stobinski L., Lesiak B., Malolepszy A., Mazurkiewicz A., Mierzwa B., Zemek J., et al., *J. Electron. Spectros.*, 2014; **195**: 145–154. DOI 10.1016/j.elspec.2014.07.003.
- [35] Cygan T., Wozniak J., Kostecki M., Petrus M., Jastrzębska A., Ziemkowska W., et al., *Ceram. Int.*, 2017; **43**: 6180–6186. DOI 10.1016/j.ceramint.2017.02.015.
- [36] Gupta N.K., Kim S., Bae J. and Kim K.S., *RSC Adv.*, 2021; **11(9)**: 4890–4900. DOI 10.1039/d0ra09017d.
- [37] Daraee M., Ghasemy E. and Rashidi A.J., *J. Environ. Chem. Eng.*, 2020 ;**8**: 1–10. DOI 10.1016/j.jece.2020.103836
- [38] Lee S., Lee T. and Kim D., *Ind. Eng. Chem. Res.*, 2017; **56(11)**: 3116–3122. DOI 10.1021/acs.iecr.6b04747.

Available online at www.sciencedirect.com

ScienceDirect

journal homepage: www.elsevier.com/locate/ijhe

Enhancing the hydrogen permeation of alumina composite porous membranes via graphene oxide addition

Montree Hankoy^{a,b}, Chaiwat Phrompet^{a,c}, Chesta Ruttanapun^{a,c},
Prangtip Rittichote Kaewpengkrow^d, Supawan Vichaphund^e,
Duangduen Atong^e, Mettaya Kitiwan^{a,b,c,f},
Phacharaphon Tunthawiroon^{b,c,f}

^a Department of Physics, School of Science, King Mongkut's Institute of Technology Ladkrabang, Bangkok 10520, Thailand

^b Devices and Systems for Energy and Environment Research Unit, School of Science, King Mongkut's Institute of Technology Ladkrabang, Bangkok 10520, Thailand

^c Center of Excellence in Smart Materials Research and Innovation, King Mongkut's Institute of Technology Ladkrabang, Bangkok 10520, Thailand

^d Rattanakosin College for Sustainable Energy and Environment (RCSEE), Rajamangala University of Technology Rattanakosin, 96 Moo 3 Phutthamonthon Sai 5 Rd., Salaya, Phutthamonthon, Nakhon Pathom, 73170, Thailand

^e National Metal and Materials Technology Center (MTEC), National Science and Technology Development Agency (NSTDA), Thailand Science Park, Pathum Thani, 12120, Thailand

^f Department of Industrial Engineering, School of Engineering, King Mongkut's Institute of Technology Ladkrabang, Bangkok 10520, Thailand

HIGHLIGHTS

- Effect of graphene oxide (GO) on properties of Al₂O₃/GO porous membrane are studied.
- Addition of 2.5–3.0 wt.% GO improves H₂ permeance and H₂/N₂ selectivity.
- High H₂ permeance of $232\text{--}410 \times 10^{-6} \text{ mol m}^{-2} \text{ s}^{-1} \text{ Pa}^{-1}$ was achieved.
- H₂/N₂ selectivity is in range of 4.0–4.2, suggesting Knudsen diffusion mechanism.

ARTICLE INFO

Article history:

Received 10 July 2022

Received in revised form

13 September 2022

Accepted 3 October 2022

Available online 28 October 2022

Keywords:

Graphene oxide

Al₂O₃

ABSTRACT

Graphene oxide (GO) membranes have attracted considerable interest for hydrogen (H₂) purification applications. However, the addition of GO into matrix materials to enhance the efficiency of H₂ permeation remains a challenge. In this study, the fabrication of alumina/graphene oxide (AGO) composites containing varying contents of GO (0.5–3.0 wt.%) was investigated. The AGO composites were formed into pellets and sintered for 2 h at 1500 °C. Accordingly, the presence of GO in the membranes following sintering was confirmed by Raman spectroscopy. Additionally, the porosity of the AGO composites increased from 3.7% to 26.9% as the GO concentration increased from 0.5 wt.% to 3.0 wt.%. Furthermore, the average pore diameter of the AGO composites was in the range of 87–228 nm, and the pore size distribution was unimodal. The performance of the AGO membranes was

* Corresponding author. Department of Physics, School of Science, King Mongkut's Institute of Technology Ladkrabang, Bangkok 10520, Thailand.

E-mail address: mettaya.ki@kmitl.ac.th (M. Kitiwan).

<https://doi.org/10.1016/j.ijhydene.2022.10.027>

0360-3199/© 2022 Hydrogen Energy Publications LLC. Published by Elsevier Ltd. All rights reserved.

H₂ permeance
H₂/N₂ selectivity
Knudsen diffusion
Porous membrane

investigated for the permeance of single gases H₂ and N₂ at 30–500 °C to evaluate their potential for H₂ separation applications. The AGO membranes with a GO addition of 2.5 and 3.0 wt% exhibited a high hydrogen permeance of 232–410 × 10⁻⁶ mol m⁻² s⁻¹ Pa⁻¹, which was approximately 10 times greater than that of pristine Al₂O₃ membrane. Additionally, the ideal H₂/N₂ selectivity values ranged from 4.02 to 4.20. Furthermore, gas permeation through the AGO membrane was observed to follow the Knudsen diffusion mechanism.

© 2022 Hydrogen Energy Publications LLC. Published by Elsevier Ltd. All rights reserved.

Introduction

Porous ceramics have numerous advantages, including high permeability, high specific surface area, high stability, low density, low thermal conductivity, and damage tolerance [1,2]. The combination of these distinctive properties enables the use of porous ceramics in numerous applications, such as separation membranes [3–5], high-temperature gas filters [6], lightweight structures [7,8], high refractory bricks [1], and biomedical replacements for bone and teeth [9–11]. Owing to the enormous global demand for cleaner energy and the search for more energy-efficient processes, many researchers have recently concentrated on developing novel porous ceramics membrane technologies for hydrogen separation that have the potential to reduce fabrication costs and complexity [12–14].

Separation membranes comprised of graphene [15,16] and its derivatives, such as reduced graphene oxide (rGO) [17] and graphene oxide (GO) [18–20], have attracted a great deal of interest because of the unique two-dimensional structure of these materials, which has been demonstrated to offer exceptional permeability and selectivity. Accordingly, GO has been investigated as a potential membrane material for hydrogen separation owing to its high mechanical strength, scalability, chemical stability, and thermal conductivity. In addition, a single layer of carbon can be used to create separation membranes with a short transport distance and high flux [21–23]. The mechanism of gas permeation through the GO membrane involves diffusion and molecular sieving, which are dependent on surface chemistry and pore size distribution, respectively [24]. Gases permeate through the nanoscale channels between GO sheets and/or through the pore defects in the GO sheets. Thus, the arrangement and imperfections of the GO layer play a significant role in the permeation efficiency of the GO membrane [25]. The potential of porous graphene for H₂/N₂ separation was investigated by Du et al. [26], using a molecular dynamics simulation. Different shapes and sizes affected the performance of H₂ and N₂ selectivity and permeability. In addition, H₂ and N₂ permeation mechanisms through porous graphene are distinct. Owing to the size restriction, only H₂ molecules can pass through nanopores of small size. Conversely, N₂ molecules collect on the surface of graphene because of van der Waals interactions between graphene and the larger nanopores, which allow more N₂ to permeate.

By adjusting deposition parameters, such as the thickness of the layer and concentration of GO, which have a significant

impact on the performance of the hydrogen separation, GO membranes can be used to achieve exceptional hydrogen separation properties [22]. The preparation of GO layers on ceramics supports, such as disks, hollow fibers, and tubes, by vacuum filtration was proposed as a straightforward method for achieving stable GO membranes for H₂ separation. Li et al. [22] used vacuum filtration to create a GO membrane with an ultrathin 1.8 nm layer on anodic alumina oxide. This membrane exhibited a high H₂/N₂ selectivity of 900, indicating molecular sieving behavior due to an intrinsic defect, while the H₂ permeance was estimated to be 10⁻⁸ mol m⁻² s⁻¹ Pa⁻¹. Zeynali et al. [23] investigated the modification of an alumina tube with a TiO₂ intermediate layer to improve the adhesion of the GO layer to the support; the composite membrane exhibited a H₂ permeance of 0.3 × 10⁻⁶ mol m⁻² s⁻¹ Pa⁻¹ and H₂/N₂ selectivity of 9. Furthermore, Zeynali et al. [25] modified an alumina tube with boehmite sol prior to coating GO on the top surface; as a result, the membrane demonstrated a H₂ permeance of 5.9 × 10⁻⁷ mol m⁻² s⁻¹ Pa⁻¹ and H₂/N₂ selectivity of 16.5 for permeation at 3 bar and ambient temperature. Ma et al. [27] fabricated a surfactant-modified GO membrane on hollow alumina fibers; the membrane exhibited a H₂ permeance of 0.77 × 10⁻⁷ mol m⁻² s⁻¹ Pa⁻¹ and H₂/N₂ selectivity of 28 at room temperature. Zhu et al. [28] fabricated a GO membrane with a thickness of 230 nm by vacuum-suction impregnation on yttrium-stabilized zirconia hollow fibers that provided a H₂ permeance of 4.46 × 10⁻⁸ mol m⁻² s⁻¹ Pa⁻¹ and H₂/N₂ selectivity of 64. Meng et al. [29] used silicate-1 as an intermediate layer to enhance the deposition of GO on the surface of the Al₂O₃ hollow fiber, achieving a H₂ permeance of 1.22 × 10⁻⁷ mol m⁻² s⁻¹ Pa⁻¹ and H₂/N₂ selectivity of 40.7. Ribeiro et al. [30], investigated GO layer addition on spinel (MgAl₂O₄) hollow fibers using a vacuum-assisted method. With a GO layer thickness of 1.7 μm, the membrane exhibited a H₂ permeance of 8.2 × 10⁻⁷ mol m⁻² s⁻¹ Pa⁻¹ and H₂/N₂ selectivity of 3.3. Cheng et al. [31] fabricated a cross-link GO nano sheet with an ultrathin layer (~50 nm) on an anodized aluminum oxide substrate; the membrane exhibited a H₂/CO₂ selectivity of 21.3 and H₂ permeance of 1.7 × 10⁻⁸ mol m⁻² s⁻¹ Pa⁻¹. Zhou et al. [32] fabricated a g-C₃N₄/GO nano sheet membrane with a H₂/CO₂ selectivity of 39.2 and H₂ permeance of 2.2 × 10⁻⁷ mol m⁻² s⁻¹ Pa⁻¹. A novel method for preparing GO thin films for gas separation was recently proposed. Zhou et al. [33], prepared a GO film with a thickness of less than 20 nm using ink-jet printing on a polysulfone polymer support. Using 1.0 mg/mL GO ink with three layers of printing, a high H₂/N₂ selectivity of 7.9 and H₂ permeance of approximately 1.5 × 10⁻⁶ mol m⁻² s⁻¹ Pa⁻¹ were obtained.

An examination of the existing literature revealed that membranes with high H₂ selectivity typically have a low H₂ permeance [22,23,25,27–33], making them unsuitable for large-scale commercial hydrogen production. Moreover, the use of GO-coated polymer membranes is restricted in a number of applications, particularly those that operate at high temperatures [13]. Consequently, porous ceramic membranes with the capability of high gas flow and the ability to maintain stability at high temperatures can enhance the hydrogen permeability of the membrane. The incorporation of GO into porous ceramics is also a promising strategy for enhancing the hydrogen selectivity. To improve the efficiency of H₂ permeation, however, GO incorporation into porous ceramics remains a challenge. In this study, we investigated the effect of GO content on the H₂ separation performance of porous Al₂O₃ composite membranes. The Al₂O₃/GO (AGO) membranes were fabricated using a cost-effective and facile approach by directly combining Al₂O₃ powder with varying amounts of GO, followed by high-temperature consolidation. The influence of GO addition on the physical properties, morphology, and hardness of AGO membranes were also examined. The single-gas permeation and separation performance of AGO composite membranes was systematically evaluated at different pressures and temperatures.

Materials and method

Raw materials

Commercial alpha-alumina powder (Al₂O₃, 99.9% purity, Nippon Light Metal, Japan) was used as the starting material. Additionally, magnesium oxide powder (MgO, 99.9% purity, Fujifilm Wako Chemical, Japan) was used as a sintering additive. GO powder was synthesized via a modified Hummers method as previously reported [34]. Briefly, GO was synthesized through an oxidation process of graphite with H₂SO₄ and KMnO₄ oxidizing agent. Subsequently, GO was re-dispersed in acetone after 1.30 h of ultrasonication and 15 min of centrifugation at 8000 rpm. Finally, a dark brown supernatant containing 5 mg/mL aqueous GO was obtained.

Preparation of AGO composites membrane

First, the green Al₂O₃ powder was prepared by doping Al₂O₃ with 1 wt% MgO. The Al₂O₃/GO mixture powder was then prepared with varying GO content (0, 0.5, 1.0, 1.5, 2.0, 2.5, and 3.0 wt%), represented as Al₂O₃, AGO0.5, AGO1.0, AGO1.5, AGO2.0, AGO2.5, and AGO3.0, respectively. The powders were mixed by ball-milling using alumina balls (3 mm in diameter) and an ethanol medium in a polypropylene bottle for 24 h at a rotational speed of 300 rpm. Following ball-milling, the slurry was dried in an oven at 120 °C for 24 h. The mixed powders were then sieved using a 200-mesh screen to reduce agglomerates. Under uniaxial pressure of 24 MPa, the powder mixtures were pressed into disk-shaped specimens with a diameter of 13 mm and a height of 3 mm using a stainless steel mold. Following this, the specimens were sintered at 1500 °C in an argon atmosphere with a constant heating rate of 5 °C/min and dwell time of 2 h.

Characterizations

The phases of the composites were identified using high-resolution X-ray diffraction (XRD; Miniflex600, Rigaku, Japan) employing Cu K- α radiation ($\lambda = 1.5406$ nm) generated at 40 kV and 30 mA to scan the diffraction angles (2θ) between 10 and 80° with a stepping interval of 0.02° per second. Additionally, the characteristic structures of the GO powder and AGO composites were confirmed using Raman spectrometry (DXR SmartRaman, Thermo Fisher Scientific, USA) with an excitation wavelength of 352 nm. The surface morphology of the sintered specimens was observed using field-emission scanning electron microscopy (FESEM, Apreo 2, Thermo Fisher Scientific, USA), while the average grain size was determined using the mean linear intercept method and ImageJ software. The Archimedes method was used to measure the densification parameters of the sintered specimens in terms of porosity and relative density. Using the rule of mixtures, the theoretical densities of Al₂O₃ and GO were calculated to be 3.98 g/cm³ and 1.8 g/cm³, respectively [35], while the relative density was calculated by dividing the bulk density by the theoretical density. Additionally, the pore size distribution of the specimens was analyzed using mercury porosimetry (MicroActive AutoPore V 9600, ATS Scientific Inc, Canada). The hardness of the sintered samples was measured using a Vickers's hardness indentation tester (Zwick Roell, Ulm, Germany) by applying a 98 N load with a loading time of 15 s, and ten measurements were taken and averaged for each sample. Accordingly, the Vickers hardness was determined using the following equation [36]:

$$H_v = 1.854 \times 10^9 \left(\frac{P}{d^2} \right) \quad (1)$$

where P is the applied load and d is the average of the two diagonal lengths.

Single-gas permeance measurement

The single-gas permeation experiment was conducted using pure nitrogen and hydrogen (purity 99.99% and 99.999%, respectively). N₂ and H₂ had kinetic diameters of 3.64 Å and 2.89 Å, respectively. The schematic diagram of the experimental setup for permeation gas tests and membrane cells is shown in Fig. 1. Both single-gas permeation tests were conducted over a temperature range of 25–500 °C, with transmembrane pressures of $\Delta P = 50$ –150 kPa for nitrogen gas and $\Delta P = 25$ –125 kPa for hydrogen gas. The permeation area was 0.77 cm². A soap-film flow meter was used to measure the flux of the permeated gases. Before each measurement, the membranes were outgassed to atmospheric pressure.

Results and discussion

The crystallographic phases of the GO starting powder, Al₂O₃ specimen, and AGO composites, as examined by XRD, are shown in Fig. 2. One prominent diffraction peak is observed at 10.83° for the GO powder, which corresponds to its hexagonal structure with the (002) reflection plane. The interplanar spacing distance of $d_{002} = 0.816$ nm agrees well with the result

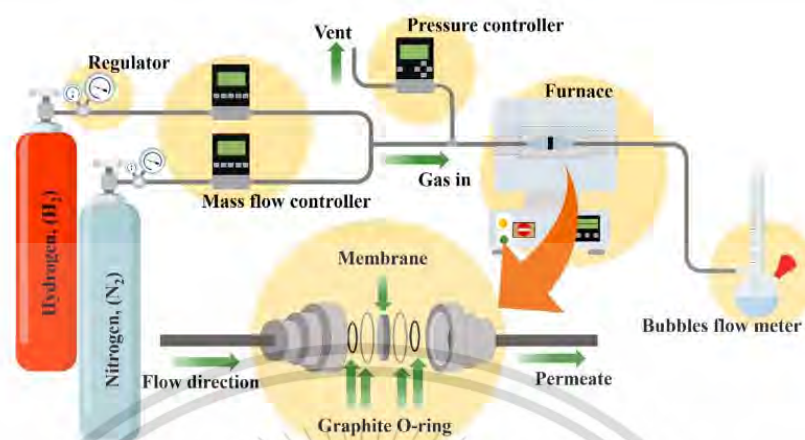


Fig. 1 – Schematic representation of the equipment for gas permeation tests and membrane cell.

reported by Lian et al. [37]. The interplanar spacing distance of GO is greater than that of graphite (0.336 nm) owing to the addition of oxygen-containing groups at the edge of each layer, resulting in a larger space between the layers [38]. The presence of GO with small interlayer spacing in the matrix will enhance the membrane's selectivity by delaying the passage of larger gas molecules [29]. The Bragg refraction of the sintered Al_2O_3 and AGO composites exhibits peaks that correspond well with the hexagonal structure (JCPDS no. 01-073-1123). However, the prominent GO peak is not observed in the AGO composites, which may have been caused by the small amount of GO used or by the strong peaks of Al_2O_3 . The XRD results confirm that there is no phase transformation in this system that could affect hydrogen permeation.

Raman spectroscopy is an efficient method for studying the crystalline structure and disordering of carbon-based materials. The Raman spectra of the GO starting powder and AGO3.0 composite are shown in Fig. 3. The GO spectrum has

two characteristic bands, the D band resulting from the stretching vibration of sp^3 carbon atoms that induces disorder and defects, and the G band resulting from the stretching vibration of sp^2 carbon atoms that conforms to the first order scattering of the E_{2g} phonon [39–41]. Moreover, the GO powder spectrum, with a D peak at 1350 cm^{-1} and a G peak at 1600 cm^{-1} , is consistent with previous studies [42–44]. The D peak appears at 1348 cm^{-1} and the G peak at 1580 cm^{-1} in the AGO3.0 composite. The ratio of the D band to G band intensity, I_D/I_G , can be used to determine the defect content of GO [45]. The I_D/I_G ratio of GO is 0.95, while that of AGO3.0 is slightly higher at 0.98, indicating that the in-plane sp^2 domain size is smaller or that structural defects in graphene increase [46,47]. Consequently, the Raman spectra confirm the presence of GO in the sintered AGO composite.

Fig. 4 illustrates the effect of GO content on the porosity and relative density of the Al_2O_3 specimen and AGO composites. The Al_2O_3 sample exhibits a high level of porosity

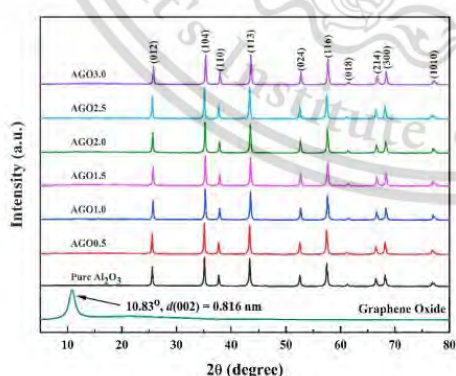


Fig. 2 – XRD patterns of the GO starting powder, Al_2O_3 specimen, and AGO composites.

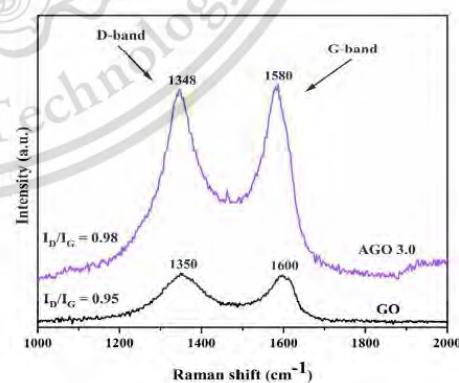


Fig. 3 – Raman spectra of the GO starting powder and AGO3.0 composite.

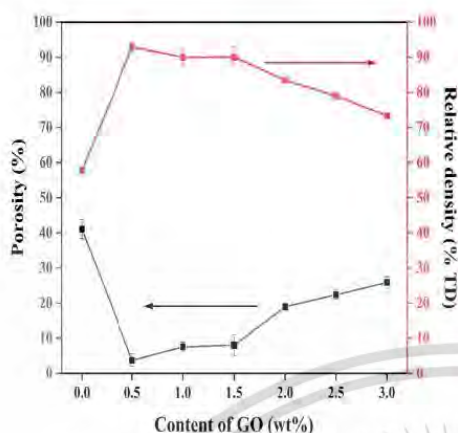


Fig. 4 – Porosity and relative density of the Al_2O_3 specimen and AGO composites with varying GO content.

(41.1%). With the addition of 0.5 wt.% GO, the porosity reduces to 3.7%. The porosity of AGO increases from 3.7% to 26.9% as the GO content increases from 0.5 wt.% to 3.0 wt.%. Correspondingly, the Al_2O_3 specimen has a low relative density of 57.8%. The addition of 0.5 wt.% GO increases the relative density of AGO to 92.9%, whereas the addition of 3.0 wt.% GO tends to decrease the relative density to 73.4%. All AGO samples have superior physical properties to those of pristine Al_2O_3 specimen. This suggests that a small quantity of GO fills the pores of the AGO composites and promotes densification. As a result, it can be deduced that the incorporation of GO improves the physical properties of the AGO composites, as it results in an increased density and decreased porosity. The porosity of the membrane has a direct effect on the amount of gas that can pass through it, as a high porosity typically results in a high permeability. Similarly, the relative density may indicate the permeability of a membrane, as density increases, gas permeation decreases. However, the presence of GO in the membrane also influenced the gas permeation behavior observed in this study. Accordingly, the influence of GO on membrane performance in relation to porosity will be discussed later.

Fig. 5 depicts the surface morphology of the Al_2O_3 specimen and AGO composites with varying amounts of GO, as determined by FESEM. In Fig. 5(a), numerous loose particles are observed in the Al_2O_3 specimen, indicating that the material is inadequately sintered. Additionally, the shape and distribution of the Al_2O_3 grains are atypical. In contrast, the AGO composites depicted in Fig. 5(b)–(g) have a microstructure that is densely packed. Additionally, the grain boundaries of the AGO composites are readily discernible. In addition, the pore volume of the composites increases as a function of GO content, which is consistent with the observed porosity. Fig. 5(h) displays the average grain size of the AGO composites with various GO additions as determined by the ImageJ software. The results indicate that the grain size increases from 0.60 to 1.22 μm as GO content increases from 0 to 1.0 wt.%, and then slightly decreases to 1.07 μm at 3.0 wt.% GO. At GO

concentrations greater than 1.0 wt.%, GO is more widely distributed at the Al_2O_3 grain boundaries, which may have inhibited grain growth [48]. As indicated by the arrow in the FESEM photograph, GO is found to be embedded between the Al_2O_3 grains. Accordingly, the dispersion of GO in Al_2O_3 matrix would improve the hydrogen separation performance of the membrane.

Mercury intrusion porosimetry (MIP) was used to determine the pore size distribution of the Al_2O_3 specimen and AGO composites with different GO contents. The results are depicted in Fig. 6 as log differential intrusion. All specimens display a unimodal pore size distribution, with average pore diameters of 148, 87, 117, 161, 235, 211, and 228 nm for composites containing 0, 0.5, 1.0, 1.5, 2.0, 2.5, and 3.0 wt.% GO, respectively. The average pore diameter of each sample is in good agreement with the position of the pore size distribution peak. In addition, pore sizes in the composites range between 40 and 380 nm, as indicated by the peak width values. According to IUPAC terminology, porous materials can be categorized into three groups: microporous (pore size <2 nm), mesoporous (pore size 2–50 nm), and macroporous (pore size >50 nm) [49–52]. Pore size of AGO composites in this study fell within the macroporous category.

The Vickers hardness (H_V) of the Al_2O_3 specimen and AGO composites with varying amounts of GO was measured, and the results are depicted in Fig. 7. The H_V of the Al_2O_3 specimen is 1.85 ± 0.08 GPa, whereas the addition of 0.5 wt.% GO increases it to the maximum value of 10.92 ± 0.63 GPa. However, the increase in the GO content from 1.0 wt.% to 3.0 wt.% causes the H_V to decrease from 10.49 ± 0.96 GPa to 4.42 ± 0.59 GPa. The density of a sample is strongly correlated with its hardness. The addition of GO at a high concentration decreases the density, resulting in a decrease in the H_V . In addition, this can be attributed to the non-uniform GO distribution; the agglomeration of GO at high concentrations leads to the formation of a network with a diminished reinforcement effect. Our observation regarding the effect of GO content on the reduction of hardness of composite is consistent with previous studies [48,53]. The hardness of a membrane may not have a direct effect on the hydrogen permeability. However, hardness is an important parameter because the composite must be durable enough to be installed in a high-pressure gas separation system. In this study, all the AGO membranes demonstrate sufficient hardness for use as separation membranes. As observed during the experiment, the membrane can be securely installed in the permeation cell, and no damage was detected during the gas permeation test.

Fig. 8 shows the permeances of H_2 and N_2 , and the H_2/N_2 selectivity of the Al_2O_3 membrane as a function of temperature. The H_2 permeance of the Al_2O_3 membrane decreases from $134 \times 10^{-6} \text{ mol m}^{-2} \text{ s}^{-1} \text{ Pa}^{-1}$ to $76 \times 10^{-6} \text{ mol m}^{-2} \text{ s}^{-1} \text{ Pa}^{-1}$ between 25 °C and 500 °C, whereas the N_2 permeance decreases from $63 \times 10^{-6} \text{ mol m}^{-2} \text{ s}^{-1} \text{ Pa}^{-1}$ to $30 \times 10^{-6} \text{ mol m}^{-2} \text{ s}^{-1} \text{ Pa}^{-1}$. As a result, the H_2/N_2 selectivity slightly increases from 2.13 to 2.53 over the range of 25–500 °C. The decrease in the H_2 and N_2 permeance with increasing temperature is similar to that observed in a porous Al_2O_3 membrane [54]; as the temperature increased, the activation energy for gas molecule transport became less negative and the adsorption mechanism

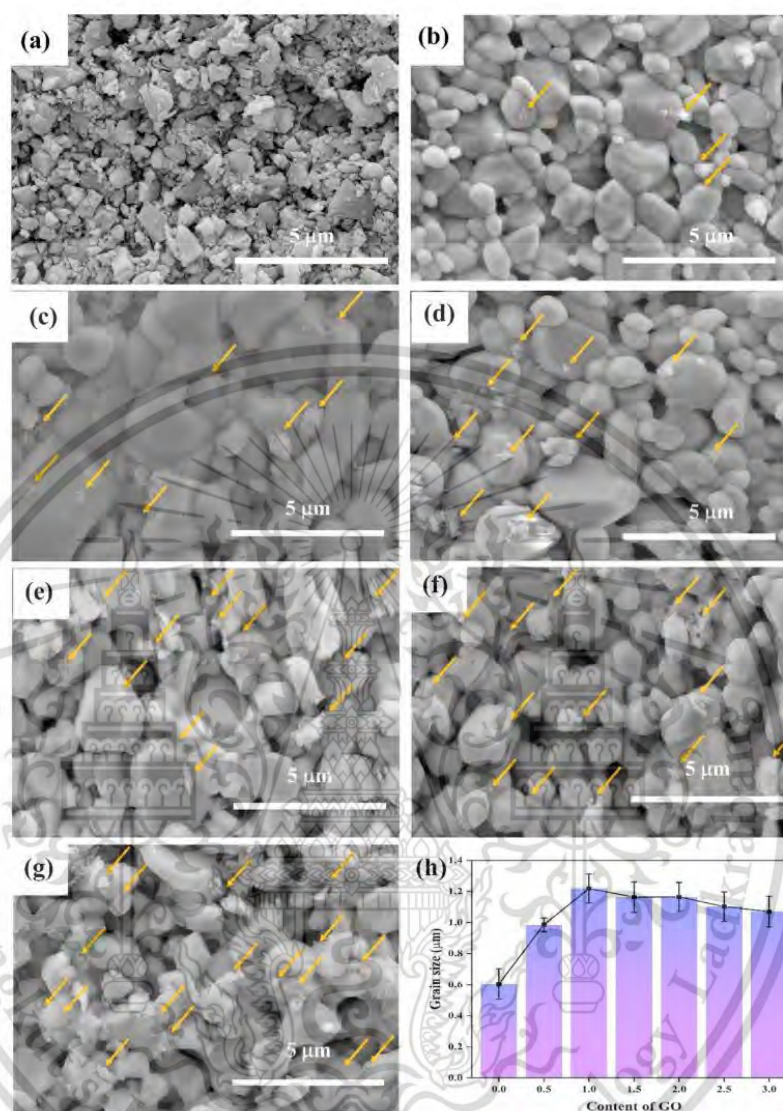


Fig. 5 – FESEM microstructure of the surface of the AGO composites with varying GO content (a) pure Al_2O_3 , (b) AGO0.5, (c) AGO1.0, (d) AGO1.5, (e) AGO2.0, (f) AGO2.5, (g) AGO3.0, and (h) the average grain size of the AGO composites. The arrows indicate the GO embedded at the grain boundary of Al_2O_3 .

weakened, resulting in a decrease in the amount of gas molecules transported through the membrane [55,56].

The gas permeation of the AGO membranes was studied, and the results are depicted in Fig. 9. At 30 °C, the H_2 permeances of AGO0.5, AGO1.0, and AGO1.5 are in the range of $41\text{--}53 \times 10^{-6} \text{ mol m}^{-2} \text{ s}^{-1} \text{ Pa}^{-1}$, which is lower than that of the Al_2O_3 membrane. These AGO membranes have significantly lower porosities (3.7%–8.0%) than the Al_2O_3 membrane (41.1%), making it more challenging for H_2 to pass through. In contrast,

the H_2 permeances of AGO2.0, AGO2.5, and AGO3.0 significantly improve to $291\text{--}411 \times 10^{-6} \text{ mol m}^{-2} \text{ s}^{-1} \text{ Pa}^{-1}$, which are significantly higher than that of Al_2O_3 membrane. Although the porosities of these AGO membranes (18.9%–26.9%) are roughly twice as low as those of the Al_2O_3 membrane (41.1%), the high content of GO (2.0 wt.% – 3.0 wt.%) likely increases the H_2 permeance. The N_2 permeance of the AGO membrane follows a similar pattern as the H_2 permeance. The N_2 permeances of AGO0.5, AGO1.0, and AGO1.5 are $14\text{--}20 \times$

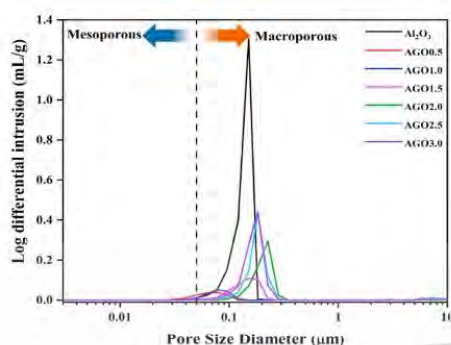


Fig. 6 – Pore size distribution of the Al_2O_3 specimen and AGO composites.

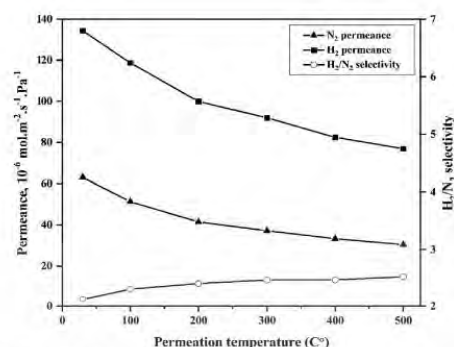


Fig. 8 – Single-gas H_2 and N_2 permeances and H_2/N_2 selectivity of the Al_2O_3 membrane as a function of temperature.

$10^{-6} \text{ mol m}^{-2} \text{ s}^{-1} \text{ Pa}^{-1}$, whereas those of AGO2.0, AGO2.5, and AGO3.0 are higher, in the range of $80\text{--}102 \times 10^{-6} \text{ mol m}^{-2} \text{ s}^{-1} \text{ Pa}^{-1}$. The increase in the permeation temperature from 30°C to 500°C leads to a reduction in the H_2 and N_2 permeance in a similar fashion to that observed in the case of the Al_2O_3 membrane. Fig. 10 depicts the mechanism of the H_2 and N_2 permeance through a membrane composed of the graphene-based composites. The GO nanosheets are filled at the pores and embedded between the grains of the Al_2O_3 matrix which created gas transport channels with a narrow diameter. Consequently, the presence of GO can retard the passage of larger gas molecules, such as N_2 [57].

Since the permeance of H_2 and N_2 decreases as the permeation temperature increases, the H_2/N_2 selectivity values of all the AGO membranes slightly change at all temperatures. The GO content has been observed to affect the H_2/N_2

N_2 selectivity. AGO0.5, AGO1.0, and AGO1.5 have H_2/N_2 selectivities between 2.53 and 3.05, whereas AGO2.0, AGO2.5, and AGO3.0 have selectivities between 3.50 and 4.09. The Knudsen selectivity for H_2 over N_2 can be calculated using the formula

$$S_{\text{H}_2/\text{N}_2} = \sqrt{M_{\text{N}_2}/M_{\text{H}_2}} \quad (2)$$

where M_{H_2} is the molecular mass of H_2 (2.016 g/mol) and M_{N_2} is the molecular mass of N_2 (28.014 g/mol); thus, the theoretical H_2/N_2 selectivity value is 3.73 [24,58]. The selectivity values in this study indicate that the permeation mechanism of the AGO membranes is in accordance with Knudsen diffusion, which provides a modest degree of selectivity.

In this study, the addition of 2.5 wt.% GO and 3.0 wt.% GO into Al_2O_3 improves the H_2 permeance and H_2/N_2 selectivity of

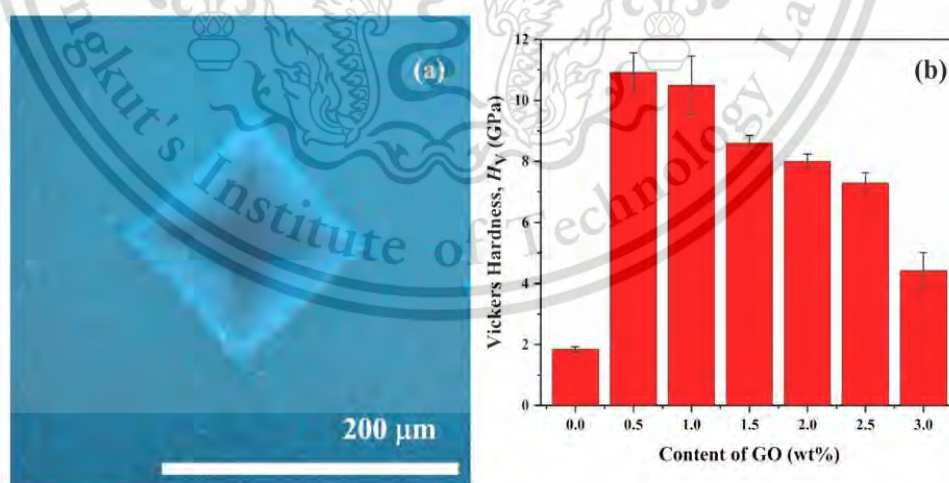


Fig. 7 – (a) Optical microscopy image of the Vickers indentation on the surface of AGO0.5 and (b) the effect of the GO content on the Vickers hardness of the Al_2O_3 specimen and AGO composites.

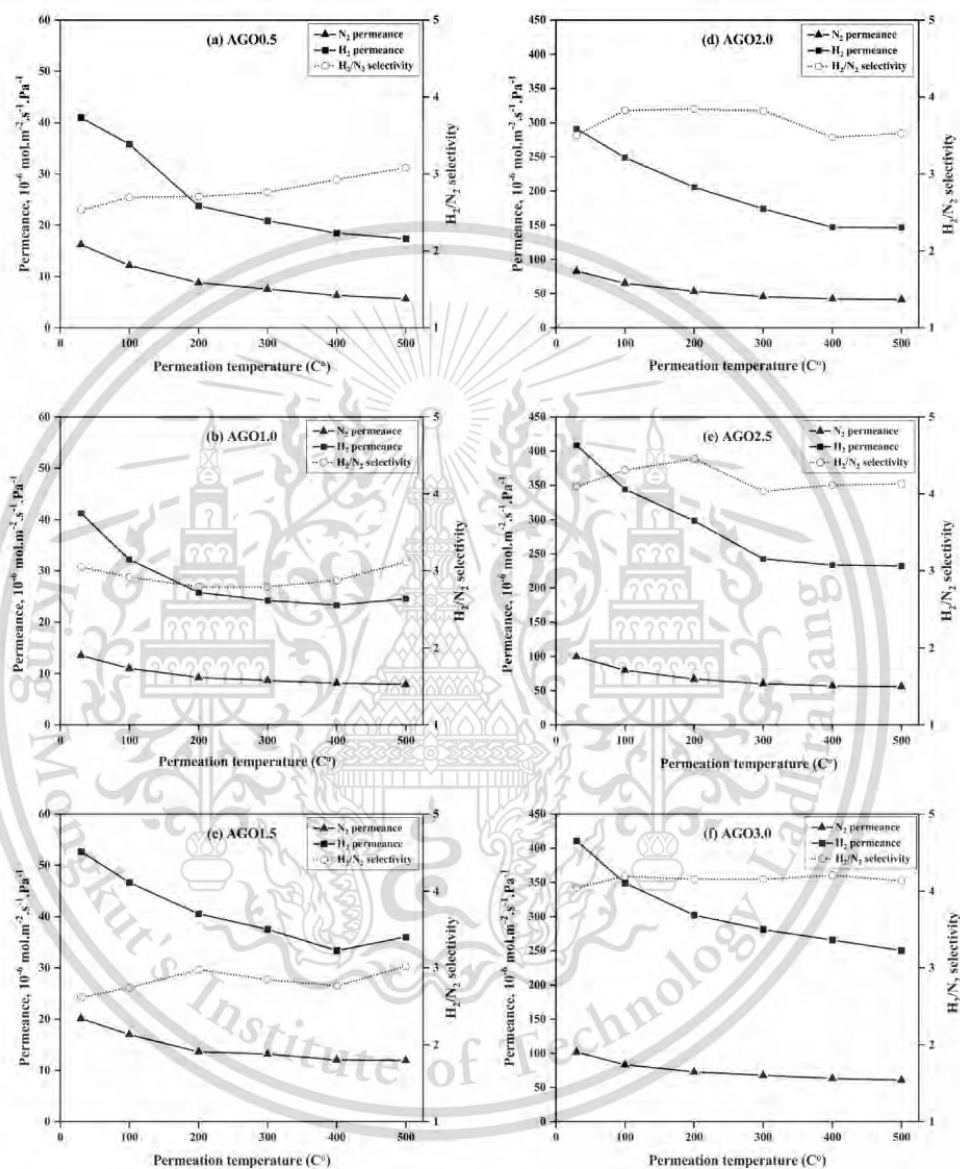


Fig. 9 – Gas permeation through the AGO membranes (a) AGO0.5, (b) AGO1.0, (c) AGO1.5, (d) AGO2.0, (e) AGO2.5, and (f) AGO3.0.

the membrane. The H_2 permeance and H_2/N_2 selectivity of AGO2.5 are $239\text{--}408 \times 10^{-6} \text{ mol m}^{-2} \text{ s}^{-1} \text{ Pa}^{-1}$ and 4.03–4.45, respectively, while those of AGO3.0 are $250\text{--}410 \times 10^{-6} \text{ mol m}^{-2} \text{ s}^{-1} \text{ Pa}^{-1}$ and 4.04–4.20, respectively, over the temperature range 30–500 $^{\circ}\text{C}$. The addition of a suitable amount of GO (2.5–3.0 wt%) increases the H_2 permeance to approximately 10 times that of the Al_2O_3 membrane. The relationship between hydrogen permeance and H_2/N_2 selectivity of GO-

ceramic membranes in the literature and the result of this work is depicted in Fig. 11. Compared to the investigation of GO modification on the surface of a ceramic hollow fiber or tube, their H_2 permeance was less than $10^{-6} \text{ mol m}^{-2} \text{ s}^{-1} \text{ Pa}^{-1}$, and their selectivities ranged from 3.3 to 900 [22,23,25,27–33]. In this study, the H_2 permeance of the AGO membranes (higher than $10^{-4} \text{ mol m}^{-2} \text{ s}^{-1} \text{ Pa}^{-1}$) is greater than that reported in the literature, and the selectivity is greater than that

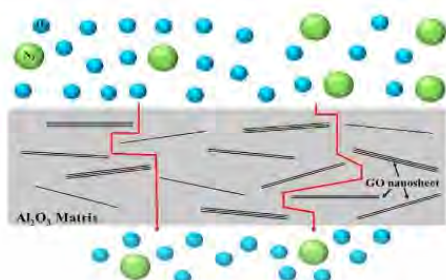


Fig. 10 – Schematic representation of gas permeation mechanism through the AGO membrane.

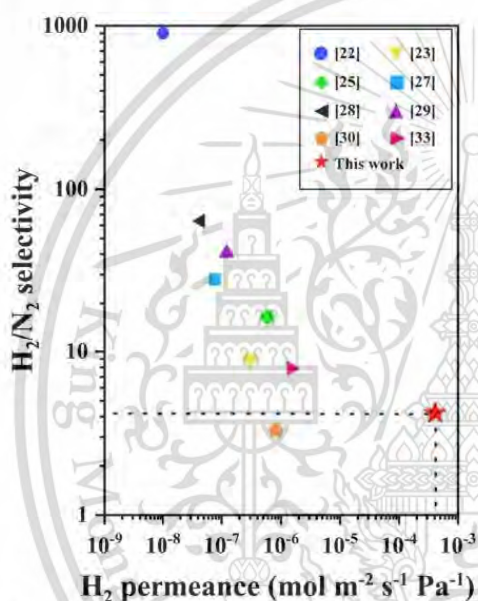


Fig. 11 – Relationship between hydrogen permeance and H_2/N_2 selectivity of the GO-ceramic membranes in literature compared to result in this work.

reported in some studies. Additionally, the AGO membranes fabricated in this study demonstrate a superior H_2 permeance. Moreover, it appears that the presence of GO in the membrane significantly improves the H_2 permeation performance.

Conclusion

Alumina/graphene oxide (AGO) composites with varying concentrations of GO (0, 0.5, 1.0, 1.5, 2.0, 2.5, and 3.0 wt.%) were sintered at 1500 °C for 2 h in an Ar atmosphere. The XRD pattern of the GO starting powder exhibited a hexagonal crystal structure with an interplanar spacing distance of 0.816 nm. The Raman spectra confirmed that the AGO

composites were composed of GO. The addition of GO influenced the physical and mechanical properties as well as improved the hydrogen separation performance. The presence of GO in the composite membranes contributed to decrease the porosity by pore filling effect of GO nanoparticles. As a result, the densification of AGO membranes increased remarkably. However, an increase of GO content from 0.5 wt.% to 3.0 wt.% led to an increase in porosity from 3.7% to 26.9% and a reduction in relative density from 92.8% to 73.4%. The microstructure of the AGO composites revealed the distribution of GO at the grain boundary of the Al_2O_3 matrix. At 0.5–3.0 wt.% GO, MIP revealed that the average pore diameter increased from 87 to 228 nm indicating that the pore size of the AGO composites were in the range of macroporous category. The effect of the GO content on the mechanical properties was studied, and the results indicated that the AGO composites were harder than pristine Al_2O_3 . The AGO composites with hardness values between 4.42 ± 0.59 GPa and 10.49 ± 0.96 GPa had sufficient strength for use as separation membranes. The evaluation of the permeation of hydrogen through the AGO composites was successfully done. The addition of 2.5–3.0 wt.% GO enhanced the H_2 permeation through the AGO membrane in the range of $232\text{--}410 \times 10^{-6} \text{ mol m}^{-2} \text{ s}^{-1} \text{ Pa}^{-1}$, as well as and enhanced the H_2/N_2 selectivity in the range of 4.02–4.20, at 30–500 °C. Thus, the current study demonstrated that the addition of GO to an Al_2O_3 membrane improves hydrogen permeation and selectivity. Accordingly, the AGO membrane developed herein, demonstrates significant potential for future use in hydrogen separation applications.

Declaration of competing interest

The authors declare that they have no known competing financial interests or personal relationships that could have appeared to influence the work reported in this paper.

Acknowledgements

This study was financially supported by the Thailand Research Fund; Grant Numbers MRG6280028. M. Hankoy would like to thank the Thailand Graduate Institute of Science and Technology (TGIST) for his Ph.D. scholarship; Grant Number SCA-CO-2563-12077-TH.

REFERENCES

- [1] Shimizu T, Matsuura K, Furue H, Matsuzak K. Thermal conductivity of high porosity alumina refractory bricks made by a slurry gelation and foaming method. *J Eur Ceram Soc* 2013;33:3429–35. <https://doi.org/10.1016/j.jeurceramsoc.2013.07.001>.
- [2] Yang Y, Shimai S, Sun Y, Dong M, Kamiya H, Wang S. Fabrication of porous Al_2O_3 ceramics by rapid gelation and mechanical foaming. *J Mater Res* 2013;28:2012–6. <https://doi.org/10.1557/jmr.2013.170>.

- [3] Liu Y, Zhu W, Guan K, Peng C, Wu J. Preparation of high permeable alumina ceramic membrane with good separation performance: via UV curing technique. *RSC Adv* 2018;8:13567–77. <https://doi.org/10.1039/c7ra13195j>.
- [4] Aouadja F, Bouzerara F, Guvenc CM, Demir MM. Fabrication and properties of novel porous ceramic membrane supports from the (Sig) diatomite and alumina mixtures. *Bol La Soc Esp Ceram y Vidr* 2021;1–10. <https://doi.org/10.1016/j.bsecv.2021.04.002>.
- [5] Vercauteren S, Keizer K, Vansant EF, Luyten J, Leysen R. Porous ceramic membranes: preparation, transport properties and applications. *J Porous Mater* 1998;5:241–58. <https://doi.org/10.1023/a:1009634305315>.
- [6] Park JK, Lee JS, Lee SI. Preparation of porous cordierite using gelcasting method and its feasibility as a filter. *J Porous Mater* 2002;9:203–10. <https://doi.org/10.1023/A:1020939018359>.
- [7] Muth JT, Dixon PG, Woish L, Gibson LJ, Lewis JA. Architected cellular ceramics with tailored stiffness via direct foam writing. *Proc Natl Acad Sci USA* 2017;114:1832–7. <https://doi.org/10.1073/pnas.1616769114>.
- [8] Zhang R, Ye C, Hou X, Li S, Wang B. Microstructure and properties of lightweight fibrous porous mullite ceramics prepared by vacuum squeeze moulding technique. *Ceram Int* 2016;42:14843–8. <https://doi.org/10.1016/j.ceramint.2016.06.118>.
- [9] Haugen HJ, Monjo M, Rubert M, Verket A, Lyngstadaas SP, Ellingsen JE, Rønold HJ, Wohlfahrt JC. Porous ceramic titanium dioxide scaffolds promote bone formation in rabbit peri-implant cortical defect model. *Acta Biomater* 2013;9:5390–9. <https://doi.org/10.1016/j.actbio.2012.09.003>.
- [10] Panzeri S, Montesi M, Hautcoeur D, Dozio SM, Chamary S, De Barra E, Tampieri A, Leriche A. Bone-like ceramic scaffolds designed with bioinspired porosity induce a different stem cell response. *J Mater Sci Mater Med* 2021;32. <https://doi.org/10.1007/s10856-020-06486-3>.
- [11] Kaplan M, Park J, Young Kim S, Ozturk A. Production and properties of tooth-colored yttria stabilized zirconia ceramics for dental applications. *Ceram Int* 2018;44:2413–8. <https://doi.org/10.1016/j.ceramint.2017.10.211>.
- [12] Hotza D, Di M, Wilhelm M, Iwamoto Y, Bernard S, Diniz C. Silicon carbide filters and porous membranes: a review of processing, properties, performance and application. *J Membr Sci* 2020;610:118193. <https://doi.org/10.1016/j.memsci.2020.118193>.
- [13] Shimonosono T, Imada H, Maeda H, Hirata Y. Separation of hydrogen from carbon dioxide through porous ceramics. *Materials* 2016;9:930. <https://doi.org/10.3390/ma9110930>.
- [14] Jiang DE, Cooper VR, Dai S. Porous graphene as the ultimate membrane for gas separation. *Nano Lett* 2009;9:4019–24. <https://doi.org/10.1021/nl9021946>.
- [15] Chuah CY, Lee J, Bae TH. Graphene-based membranes for H_2 separation: recent progress and future perspective. *Membranes* 2020;10:1–30. <https://doi.org/10.3390/membranes10110336>.
- [16] Remanan S, Padmavathy N, Ghosh S, Mondal S, Bose S, Das NC. Porous graphene-based membranes: preparation and properties of a unique two-dimensional nanomaterial membrane for water purification. *Separ Purif Technol* 2021;50:262–82. <https://doi.org/10.1080/15422119.2020.1725048>.
- [17] Shen Y, Maurizi L, Magnacca G, Boffa V, Yue Y. Tuning porosity of reduced graphene oxide membrane materials by alkali activation. *Nanomaterials* 2020;10:1–14. <https://doi.org/10.3390/nano10112093>.
- [18] Madauß L, Foller T, Plaß J, Kumar PV, Musso T, Dunkhorst K, Joshi R, Schleberger M. Selective proton transport for hydrogen production using graphene oxide membranes. *J Phys Chem Lett* 2020;11:9415–20. <https://doi.org/10.1021/acs.jpcclett.0c02481>.
- [19] Sy S, Jiang G, Zhang J, Zarrin H, Cumberland T, Abureden S, Bell E, Gostick J, Yu A, Chan Z. A near-isotropic proton-conducting porous graphene oxide membrane. *ACS Nano* 2020;14:14947–59. <https://doi.org/10.1021/acsnano.0c04533>.
- [20] Joshi RK, Alwarappan S, Yoshimura M, Sahajwalla V, Nishina Y. Graphene oxide: the new membrane material. *Appl Mater Today* 2015;1:1–12. <https://doi.org/10.1016/j.apmt.2015.06.002>.
- [21] Zeynali R, Ghasemzadeh K, Sarand AB, Khairi F, Basile A. Performance evaluation of graphene oxide (GO) nanocomposite membrane for hydrogen separation: effect of dip coating sol concentration. *Separ Purif Technol* 2018;200:169–76. <https://doi.org/10.1016/j.seppur.2018.02.032>.
- [22] Li H, Song Z, Zhang X, Huang Y, Li S, Mao Y, et al. Ultrathin, molecular-sieving graphene oxide membranes for selective hydrogen separation. *Science* 2013;342:95–8. <https://doi.org/10.1126/science.1236686>.
- [23] Zeynali R, Ghasemzadeh K, Iulianelli A, Basile A. Experimental evaluation of graphene oxide/TiO₂-alumina nanocomposite membranes performance for hydrogen separation. *Int J Hydrogen Energy* 2020;45:7479–87. <https://doi.org/10.1016/j.ijhydene.2019.02.225>.
- [24] Boutilier MSH, Hadjiconstantinou NG, Karnik R. Knudsen effusion through polymer-coated three-layer porous graphene membranes. *Nanotechnology* 2017;28:184003. <https://doi.org/10.1088/1361-6528/aa680f>.
- [25] Zeynali R, Ghasemzadeh K, Behrooz A, Khairi F, Basile A. Experimental study on graphene-based nanocomposite membrane for hydrogen purification: effect of temperature and pressure. *Catal Today* 2019;330:16–23. <https://doi.org/10.1016/j.cattod.2018.05.047>.
- [26] Du H, Li J, Zhang J, Su G, Li X, Zhao Y. Separation of hydrogen and nitrogen gases with porous graphene membrane. *J Phys Chem C* 2011;23261–6. <https://doi.org/10.1021/jp206258u>.
- [27] Ma S, Tang Z, Fan Y, Zhao J, Meng X, Yang N, Zhou S, Liu S. Surfactant-modified graphene oxide membranes with tunable structure for gas separation. *Carbon* 2019;152:144–50. <https://doi.org/10.1016/j.carbon.2019.06.006>.
- [28] Zhu J, Meng X, Zhao J, Jin Y, Yang N, Zhang S, Sunarso J, Liu S. Facile hydrogen/nitrogen separation through graphene oxide membranes supported on YSZ ceramic hollow fibers. *J Membr Sci* 2017;535:143–50. <https://doi.org/10.1016/j.jmetsci.2017.04.032>.
- [29] Meng X, Fan Y, Zhu J, Jin Y, Li C, Yang N, Sunarso J, Liu S. Improving hydrogen permeation and interface property of ceramic-supported graphene oxide membrane via embedding of silicalite-1 zeolite into Al₂O₃ hollow fiber. *Separ Purif Technol* 2019;227:115712. <https://doi.org/10.1016/j.seppur.2019.115712>.
- [30] Ribeiro SRFL, Bessa LP, Cardoso VL, Reis MHM. Enhanced hydrogen permeance through graphene oxide membrane deposited on asymmetric spinel hollow fiber substrate. *Int J Hydrogen Energy* 2022;47:9616–26. <https://doi.org/10.1016/j.ijhydene.2022.01.049>.
- [31] Cheng L, Guan K, Liu G, Jin W. Cysteamine-crosslinked graphene oxide membrane with enhanced hydrogen separation property. *J Membr Sci* 2020;595:117568. <https://doi.org/10.1016/j.memsci.2019.117568>.
- [32] Zhou Y, Zhang Y, Xue J, Wang R, Yin Z, Ding L, et al. Graphene oxide-modified g-C₃N₄ nanosheet membranes for efficient hydrogen purification. *Chem Eng J* 2021;420:129574. <https://doi.org/10.1016/j.cej.2021.129574>.
- [33] Zhou F, Dong Q, Chen JT, Sengupta B, Jiang J, Xu WL, Li H, Li S, Yu M. Printed graphene oxide-based membranes for gas

- separation and carbon capture. *Chem Eng J* 2022;430:132942. <https://doi.org/10.1016/j.cej.2021.132942>.
- [34] Phrompet C, Sriwong C, Ruttanapun C. Mechanical, dielectric, thermal and antibacterial properties of reduced graphene oxide (rGO)-nanosized C3AH6 cement nanocomposites for smart cement-based materials. *Compos B Eng* 2019;175:107128. <https://doi.org/10.1016/j.compositesb.2019.107128>.
- [35] Manisa VK, Porter M, Whiting MJ, Dorey RA. Effect of processing on the stability and electrical properties of pressureless sintered graphene oxide–alumina composites. *Ceram Int* 2022;48:15839–47. <https://doi.org/10.1016/j.ceramint.2022.02.122>.
- [36] Kitiwan M, Goto T. Fabrication of tungsten carbide–diamond composites using SiC-coated diamond. *Int J Refract Met Hard Mater* 2019;85:105053. <https://doi.org/10.1016/j.ijmhm.2019.105053>.
- [37] Lian B, Deng J, Leslie G, Bustamante H, Sahajwalla V, Nishina Y, Joshi J. Surfactant modified graphene oxide laminates for filtration. *Carbon* 2017;116:240–5. <https://doi.org/10.1016/j.carbon.2017.01.102>.
- [38] Johra FT, Lee JW, Jung WG. Facile and safe graphene preparation on solution based platform. *J Ind Eng Chem* 2014;20:2883–7. <https://doi.org/10.1016/j.jiec.2013.11.022>.
- [39] Chen G, Wang Y, Weng H, Wu Z, He K, Zhang P, et al. Selective separation of Pd(II) on pyridine-functionalized graphene oxide prepared by radiation-induced simultaneous grafting polymerization and reduction. *ACS Appl Mater Interfaces* 2019;11:24560–70. <https://doi.org/10.1021/acsami.9b06162>.
- [40] Zhu C, Guo S, Fang Y, Dong S. Reducing sugar: new functional molecules for the green synthesis of graphene nanosheets. *ACS Nano* 2010;4:2429–37. <https://doi.org/10.1021/nn1002387>.
- [41] Wang J, Chen Z, Chen B. Adsorption of polycyclic aromatic hydrocarbons by graphene and graphene oxide nanosheets. *Environ Sci Technol* 2014;48:4817–25. <https://doi.org/10.1021/es405227a>.
- [42] Claramunt S, Varea A, López-Díaz D, Velázquez MM, Comet A, Cirera A. The importance of interbands on the interpretation of the Raman spectrum of graphene oxide. *J Phys Chem C* 2015;119:10123–9. <https://doi.org/10.1021/acs.jpcc.5b04590>.
- [43] López-Díaz D, López Holgado M, García-Fierro JL, Velázquez MM. Evolution of the Raman spectrum with the chemical composition of graphene oxide. *J Phys Chem C* 2017;121:20489–97. <https://doi.org/10.1021/acs.jpcc.7b06236>.
- [44] Shen J, Hu Y, Shi M, Lu X, Qin C, Li C, Ye M. Fast and facile preparation of graphene oxide and reduced graphene oxide nanoplatelets. *Chem Mater* 2009;21:3514–20. <https://doi.org/10.1021/cm901247t>.
- [45] Phiri J, Gane P, Maloney TC. High-concentration shear-exfoliated colloidal dispersion of surfactant–polymer-stabilized few-layer graphene sheets. *J Mater Sci* 2017;52:8321–37. <https://doi.org/10.1007/s10853-017-1049-y>.
- [46] Bai Y, Liu M, Sun J, Gao L. Fabrication of Ni-Co binary oxide/reduced graphene oxide composite with high capacitance and cyclability as efficient electrode for supercapacitors. *Ionics* 2016;22:535–44. <https://doi.org/10.1007/s11581-015-1576-y>.
- [47] Stankovich S, Dikin DA, Piner RD, Kohlhaas KA, Kleinhammes A, Jia Y, et al. Synthesis of graphene-based nanosheets via chemical reduction of exfoliated graphite oxide. *Carbon* 2007;45:1558–65. <https://doi.org/10.1016/j.carbon.2007.02.034>.
- [48] Cygan T, Wozniak J, Kostecki M, Petrus M, Jastrzębska A, Ziemkowska W, et al. Mechanical properties of graphene oxide reinforced alumina matrix composites. *Ceram Int* 2017;43:6180–6. <https://doi.org/10.1016/j.ceramint.2017.02.015>.
- [49] Corma A. From microporous to mesoporous molecular sieve materials and their use in catalysis. *Chem Rev* 1997;97:2373–419. <https://doi.org/10.1021/cr960406n>.
- [50] Chaudhary V, Sharma S. An overview of ordered mesoporous material SBA-15: synthesis, functionalization and application in oxidation reactions. *J Porous Mater* 2017;24:741–9. <https://doi.org/10.1007/s10934-016-0311-z>.
- [51] Taguchi A, Schüth F. Ordered mesoporous materials in catalysis. *Microporous Mesoporous Mater* 2005;77:1–45. <https://doi.org/10.1016/j.micromeso.2004.06.030>.
- [52] Vernimmen J, Meynen V, Cool P. Synthesis and catalytic applications of combined zeolitic/mesoporous materials. *Beilstein J Nanotechnol* 2011;2:785–801. <https://doi.org/10.3762/bjnano.2.87>.
- [53] Centeno A, Rocha VG, Alonso B, Fernández A, Gutiérrez-González CF, Torrecillas R, Zurutuza A. Graphene for tough and electroconductive alumina ceramics. *J Eur Ceram Soc* 2013;33:3201–10. <https://doi.org/10.1016/j.jeurceramsoc.2013.07.007>.
- [54] Yu CY, Sea BK, Lee DW, Park SJ, Lee KY, Lee KH. Effect of nickel deposition on hydrogen permeation behavior of mesoporous γ -alumina composite membranes. *J Colloid Interface Sci* 2008;319:470–6. <https://doi.org/10.1016/j.jcis.2007.11.056>.
- [55] Lee HJ, Suda H, Haraya K. Gas permeation properties in a composite mesoporous alumina ceramic membrane. *Kor J Chem Eng* 2005;22:721–8. <https://doi.org/10.1007/BF02705789>.
- [56] Lee HJ, Yamauchi H, Suda H, Haraya K. Influence of adsorption on the gas permeation performances in the mesoporous alumina ceramic membrane. *Separ Purif Technol* 2006;49:49–55. <https://doi.org/10.1016/j.seppur.2005.08.007>.
- [57] Liu G, Jin W, Xu N. Graphene-based membranes. *Chem Soc Rev* 2015;44:5016–30. <https://doi.org/10.1039/c4cs00423j>.
- [58] Pandey P, Chauhan RS. Membranes for gas separation. *Prog Polym Sci* 2001;26:853–93. [https://doi.org/10.1016/S0079-6700\(01\)00009-0](https://doi.org/10.1016/S0079-6700(01)00009-0).

Author biography

Name	Montree Hankoy
Date of Birth	30 November 1993
Address	102, M8, Sida District, Nakhon Ratchasima, 30430
Education	2013-2017, Bachelor of Science (B.Sc.) in Applied Physics (Solid State Electronics), School of Science, King Mongkut Institute of Technology Ladkrabang. 2017-2019, Master of Science (M.Sc.) in Applied Physics, School of Science, King Mongkut Institute of Technology Ladkrabang. 2019-2024, Doctor of Philosophy (Ph.D.) in Applied Physics, School of Science, King Mongkut Institute of Technology Ladkrabang.
Scholarship	Ph.D. Research Scholarship: Thailand Graduate Institute of Science and Technology (TGIST) by National Science and Technology Development Agency
Publication(s)	Hankoy M , Kitiwan M, Phrompet C, Ruttanapun C, Kaewpengkrow P R, Vichaphund S, Atong D, and Tunthawiroon P. Hydrogen sulfide adsorption on alumina/graphene oxide composites at ambient temperature. <i>Chiang Mai J. Sci.</i> 2022; 49: 1618-32. Hankoy M , Kitiwan M, Phrompet C, Ruttanapun C, Kaewpengkrow P R, Vichaphund S, Atong D, and Tunthawiroon P. Enhancing the hydrogen permeation of alumina composite porous membranes via graphene oxide addition. <i>Int. J. Hydrogen. Energy.</i> 2023; 48: 1380-90.